

Applied Bionics and Biomechanics

Biomimetic Actuation and Artificial Muscle

Lead Guest Editor: Qingsong He

Guest Editors: David Vokoun and Qi Shen





Biomimetic Actuation and Artificial Muscle

Applied Bionics and Biomechanics

Biomimetic Actuation and Artificial Muscle

Lead Guest Editor: Qingsong He

Guest Editors: David Vokoun and Qi Shen



Copyright © 2018 Hindawi. All rights reserved.

This is a special issue published in “Applied Bionics and Biomechanics.” All articles are open access articles distributed under the Creative Commons Attribution License, which permits unrestricted use, distribution, and reproduction in any medium, provided the original work is properly cited.

Editorial Board

Andrea Cereatti, Italy
Laurence Cheze, France
Christian Cipriani, Italy
Jose L. Contreras-Vidal, USA
Agnès Drochon, France
Fabio Esposito, Italy
Ángel Gil-Agudo, Spain
Eugenio Guglielmelli, Italy
Hiroaki Hobara, Japan
Serkan Inceoglu, USA

Zhongmin Jin, China
Kiros Karamanidis, Germany
Justin Keogh, Australia
Jan Harm Koolstra, Netherlands
Thibault Lemaire, France
Le Ping Li, Canada
Andrea Marinozzi, Italy
Craig P. McGowan, USA
Jose Merodio, Spain
Juan C. Moreno, Spain

Estefanía Peña, Spain
Simo Saarakkala, Finland
Fong-Chin Su, Taiwan
Wei Tan, USA
Amir A. Zadpoor, Netherlands
Stefano Zaffagnini, Italy
Li-Qun Zhang, USA
Nigel Zheng, USA

Contents

Biomimetic Actuation and Artificial Muscle

Qingsong He , David Vokoun , and Qi Shen
Editorial (2 pages), Article ID 4617460, Volume 2018 (2018)

A Computing Method to Determine the Performance of an Ionic Liquid Gel Soft Actuator

Bin He , Chenghong Zhang, Yanmin Zhou, and Zhipeng Wang
Research Article (11 pages), Article ID 8327867, Volume 2018 (2018)

The Gait Design and Trajectory Planning of a Gecko-Inspired Climbing Robot

Xuepeng Li , Wei Wang , Shilin Wu , Peihua Zhu , Fei Zhao , and Linqing Wang 
Research Article (13 pages), Article ID 2648502, Volume 2018 (2018)

A Highly Reliable Embedded Optical Torque Sensor Based on Flexure Spring

Yuwang Liu , Tian Tian, Jibiao Chen , Fuhua Wang, and Defu Zhang 
Research Article (14 pages), Article ID 4362749, Volume 2018 (2018)

CMM-Based Volumetric Assessment Methodology for Polyethylene Tibial Knee Inserts in Total Knee Replacement

Wei Jiang , Cuicui Ji, Zhongmin Jin, and Yuntian Dai
Research Article (6 pages), Article ID 9846293, Volume 2018 (2018)

Active Tube-Shaped Actuator with Embedded Square Rod-Shaped Ionic Polymer-Metal Composites for Robotic-Assisted Manipulation

Yanjie Wang , Jiayu Liu, Denglin Zhu, and Hualing Chen
Research Article (12 pages), Article ID 4031705, Volume 2018 (2018)

Biomimetic Beetle-Inspired Flapping Air Vehicle Actuated by Ionic Polymer-Metal Composite Actuator

Yang Zhao, Di Xu, Jiazheng Sheng, Qinglong Meng, Dezhi Wu, Lingyun Wang, Jingjing Xiao, Wenlong Lv, Qinnan Chen , and Daoheng Sun
Research Article (7 pages), Article ID 3091579, Volume 2018 (2018)

Passive Cushiony Biomechanics of Head Protection in Falling Geckos

Hao Wang , Wenbo Wang, Yi Song, Lei Cai , and Zhendong Dai
Research Article (7 pages), Article ID 9857894, Volume 2018 (2018)

Editorial

Biomimetic Actuation and Artificial Muscle

Qingsong He ¹, David Vokoun ², and Qi Shen³

¹Nanjing University of Aeronautics and Astronautics, Nanjing, China

²Academy of Sciences of the Czech Republic, Prague, Czech Republic

³University of Nevada, Las Vegas, Las Vegas, NV, USA

Correspondence should be addressed to Qingsong He; heqingsong@nuaa.edu.cn

Received 20 March 2018; Accepted 20 March 2018; Published 14 June 2018

Copyright © 2018 Qingsong He et al. This is an open access article distributed under the Creative Commons Attribution License, which permits unrestricted use, distribution, and reproduction in any medium, provided the original work is properly cited.

In general, actuation technology reflects the progress in the development of mechanical systems. Originally, actuators were linked to steam engines, then several decades later to internal combustion engines and to electromotors, making mechanical systems increasingly more flexible, with higher energy utilization and convenience. However, the traditional actuation technologies (e.g., miniature motors and gear transmissions) cannot compete with the high flexibility, high redundancy, and large load-to-weight ratio found in animal muscular systems, which cause the performance of robots to fall behind that of the animals. Distributed actuation found in animal muscular systems is one of the main reasons of flexibility, high efficiency, and large energy density. Thus, the biomimetic actuators or artificial muscles with large displacements have drawn great attention in research and industrial application development.

For these reasons, a large number of scientific works are conducted and this special issue selects the related papers from a great number of high-quality candidates. In this special issue, some important aspects of biomechanics, biomimetic actuation, and artificial muscle and sensor are covered. This special issue starts with an investigation of the internal environment and structure of a *Gekko gekko*'s brain, going to a biomimetic beetle-inspired flapping air vehicle using ionic polymer-metal composite artificial muscle. Then in the third paper, we move to active tube-shaped actuator. With the fourth paper, we start to study computing method to determine the performance of the soft actuator. The fifth paper addresses the gait design and trajectory

planning to further develop dynamic gait and reduce energy consumption of climbing robot. And a new high-reliable and lightweight embedded optical torque sensor is proposed for biomimetic robot arm in the sixth paper. Finally, a volumetric wear assessment methodology for polyethylene tibial knee inserts in total knee replacements is presented in the seventh paper. More in detail, a brief summary of each paper is as follows.

The first paper “Passive Cushiony Biomechanics of Head Protection in Falling Geckos” by H. Wang et al. used the magnetic resonance imaging technique to scan a *Gekko gekko*'s brain to study its internal environment and structure in order to understand the mechanism responsible for the self-protection in case of head impact. The results showed that the brain parenchyma was fully surrounded by the cerebrospinal fluid (CSF) in the skull. A succulent characteristic was presented, which meant the intracalvarium was significantly occupied by the CSF, up to 45% in volume. Then a simplified 3D finite element model was built, and a dynamic simulation was conducted to evaluate the mechanical property of this succulent characteristic during head impacts. These implied the succulent characteristics may play certain roles on the self-protection in case of head impact, which is adaptable to the *Gekko gekko*'s locomotion and behavior.

The paper “Biomimetic Beetle-Inspired Flapping Air Vehicle Actuated by Ionic Polymer-Metal Composite Actuator” by Y. Zhao et al. proposed a biomimetic flapping air vehicle by combining the superiority of ionic polymer-

metal composite (IPMC) with the bionic beetle flapping principle. The blocking force was compared between casted IPMC and IPMC. The flapping state of the wing was investigated, and the maximum displacement and flapping angle were measured. The flapping displacement under different voltages and frequencies was tested. The flapping displacement of the wing and the support reaction force were measured under different frequencies by experiments. The experimental results indicate that the high voltage and low frequency would get large flapping displacement.

The third paper of this special issue "Active Tube-Shaped Actuator with Embedded Square Rod-Shaped Ionic Polymer-Metal Composites for Robotic-Assisted Manipulation" by Y. Wang et al. creates an active tube by integrating bar-shaped IPMC actuators into a soft silicon rubber structure. The authors modified the Nafion solution casting method and developed a complete sequence of fabrication process for bar-shaped IPMCs with square cross sections and four insulated electrodes on the surface. The silicon gel was cured at a suitable temperature to form a flexible tube using molds fabricated by 3D printing technology. By applying different voltages to the four electrodes of each IPMC bar-shaped actuator, complex multidegree of freedom bending motions of the active tube can be generated.

In the fourth paper "A Computing Method to Determine the Performance of an Ionic Liquid Gel Soft Actuator" by B. He et al., the authors model ionic liquid gel using Mooney-Rivlin model, capable of describing the nonlinear character of the mechanical response. Their model is validated by experimental stress-strain data obtained for a manufactured ionic liquid gel sample.

X. Li et al., in their paper "The Gait Design and Trajectory Planning of a Gecko-Inspired Climbing Robot," analyzed the gait design and trajectory planning, in order to further develop dynamic gait and reduce energy consumption of climbing robot based on a model with a pendular waist and four active linear legs.

Y. Liu et al., in their paper "A Highly Reliable Embedded Optical Torque Sensor Based on Flexure Spring," proposed a new high-reliable and lightweight embedded optical torque sensor for biomimetic robot arm enabling the torque measurement in joints, which can measure torque of the joint by detecting torsion of its elastic element.

Finally, in the paper "CMM-Based Volumetric Assessment Methodology for Polyethylene Tibial Knee Inserts in Total Knee Replacement," W. Jiang et al. presented a new coordinate measuring machine- (CMM-) based methodology to determine volumetric material loss based on curve surface fitting without prewear data, CAD model, or original design of drawings. The results indicate that the methodology is adequate for clinically retrieved tibial inserts where no prewear data are provided. This technique can also be used for biotribological study of other polyethylene components, since wear and damage can be assessed visually and volumetrically.

This special issue aims to promote research and provide a platform for communication of novel ideas, theories, and technologies in biomimetic actuation, sensing,

and materials. We hope that this special issue, the regular issue, and other special issues of this journal are beneficial and interesting for you.

*Qingsong He
David Vokoun
Qi Shen*

Research Article

A Computing Method to Determine the Performance of an Ionic Liquid Gel Soft Actuator

Bin He , Chenghong Zhang, Yanmin Zhou, and Zhipeng Wang

College of Electronics and Information Engineering, Tongji University, No. 4800 Caoan Road, Shanghai 201804, China

Correspondence should be addressed to Bin He; hebin@tongji.edu.cn

Received 20 October 2017; Revised 25 January 2018; Accepted 26 February 2018; Published 2 May 2018

Academic Editor: David Vokoun

Copyright © 2018 Bin He et al. This is an open access article distributed under the Creative Commons Attribution License, which permits unrestricted use, distribution, and reproduction in any medium, provided the original work is properly cited.

A new type of soft actuator material—an ionic liquid gel (ILG) that consists of BMIMBF₄, HEMA, DEAP, and ZrO₂—is polymerized into a gel state under ultraviolet (UV) light irradiation. In this paper, we first propose that the ILG conforms to the assumptions of hyperelastic theory and that the Mooney-Rivlin model can be used to study the properties of the ILG. Under the five-parameter and nine-parameter Mooney-Rivlin models, the formulas for the calculation of the uniaxial tensile stress, plane uniform tensile stress, and 3D directional stress are deduced. The five-parameter and nine-parameter Mooney-Rivlin models of the ILG with a ZrO₂ content of 3 wt% were obtained by uniaxial tensile testing, and the parameters are denoted as c_{10} , c_{01} , c_{20} , c_{11} , and c_{02} and c_{10} , c_{01} , c_{20} , c_{11} , c_{02} , c_{30} , c_{21} , c_{12} , and c_{03} , respectively. Through the analysis and comparison of the uniaxial tensile stress between the calculated and experimental data, the error between the stress data calculated from the five-parameter Mooney-Rivlin model and the experimental data is less than 0.51%, and the error between the stress data calculated from the nine-parameter Mooney-Rivlin model and the experimental data is no more than 8.87%. Hence, our work presents a feasible and credible formula for the calculation of the stress of the ILG. This work opens a new path to assess the performance of a soft actuator composed of an ILG and will contribute to the optimized design of soft robots.

1. Introduction

At room temperature, the ionogel is a polymerized gelatinous mixture from the ionic liquid and polymer matrix under UV irradiation [1, 2]. The high conductivity and stability of ionic liquids and the good mechanical properties of polymers make ionic liquid gels an ideal replacement for the traditional electroactive polymers [3]. Due to their high environmental adaptability and low-pressure impedance characteristics, soft robots have shown broad application potential in the fields of biology, medicine, agriculture, and so on. The adoption of electroactive polymer (EAP) materials for soft robots has become a hot research topic in recent years. Progress in electrochemical actuators has been made over the past few decades due to their desirable mechanical properties for intelligent robots, which are an alternative for air- and fluid-derived equipment [4–7]. Ionic liquid gels (ILG) are suitable building blocks for advanced actuators due to their tunable ionic conductivity, chemical stability, thermal stability, and simple ion transport [8–9].

Electrochemical actuators have been further developed over the past few decades for their desirable mechanical properties in intelligent robots, which are alternatives to air- and fluid-derived devices. The flexible ionic conductivity of ILG is better suited to the evolution of building blocks due to the simpler ion transport actuators [10].

Noncovalent interactions provide the gels with the very high mechanical strength and excellent self-healing ability of supramolecular materials [11, 12]. Based on these studies, we used ZrO₂ to fabricate supramolecular nanocomposites with the electrochemical behavior of an ionic liquid and mechanical strength of an ionogel polymer.

Among numerical approaches, finite element analysis is one of the most effective and most common information extraction methods to evaluate and optimize robot designs. By using this method, analytical models can be greatly simplified, which greatly increases the computational efficiency. The largest drawback is that ignorance of the nonlinear and constitutive model and the simplification of the computational model often lead to coarse solutions [13, 14].

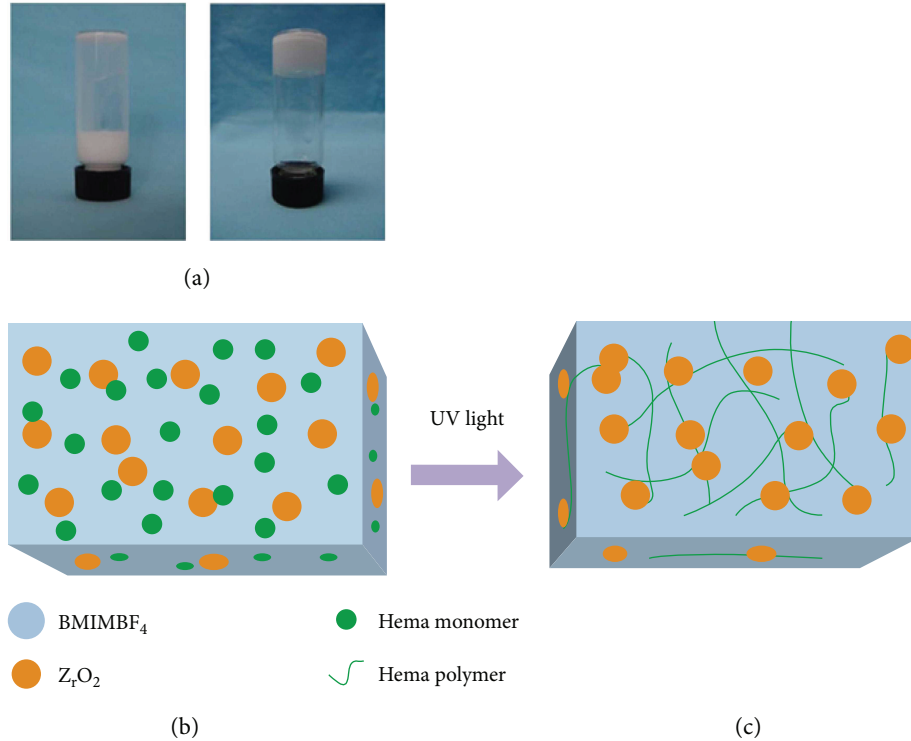


FIGURE 1: The proposed mechanism of the BMIMBF₄-based ionogel under ultraviolet light. (a) ILG solution and ILG solid, respectively. (b) The ILG solution includes BMIMBF₄, HEMA, DEAP, and ZrO₂. (c) HEMA and ZrO₂ are cross-coupled to form a 3D network.

Numerical simulations offer sufficient insight for each case during general soft robot design.

Lee et al. used the finite element method (FEM) to successfully predict the mechanical behavior of an ionic polymer-metal composite (IPMC) actuator [15]. Wang et al. established a model based on the FEM to determine the electromechanical bending behavior of photocurable ionogel actuators (PIA) [16]. He et al. used the common large-scale finite element analysis software ANSYS to simulate an ILG, which is based on the SOLID186 element and the nonlinear hyperelastic Mooney-Rivlin model [17].

Because the use of an ILG actuator requires deep understanding of the mechanical properties of the soft robot, it is necessary to establish a theoretical model to obtain its performance index. To reduce the experimental cost and time, we systematically analyzed the ILG via numerical simulations and verified the accuracy of the calculation, which contributed to the development of the ILG in the soft robot. The numerical simulation results matched the corresponding experiments, proving the validity of the model [18, 19].

2. Fabrication of the Ionic Liquid Gel

In the experiments, the ILG was composed of 1-butyl-3-methylimidazolium tetrafluoroborate (BMIMBF₄), hydroxyethyl methacrylate (HEMA), 2-diethoxyacetophenone (DEAP), and ZrO₂, with masses of 900 mg, 68.6 mg, 1.4 mg, and 30 mg, respectively. The mixed solution was then placed into a magnetic stirrer to form a suspension. Following that, the sample was placed on an ML-3500C Maxima-type cold

light source for ultra-high-intensity UV radiation curing to induce polymerization. The UV intensity is 90000uW / cm² (15'' / 380 mm distance) [20].

Figure 1(a) shows a comparison of the morphology of the ionic liquid before and after gel formation: the left figure shows the liquid state, while the right shows the solid state formed after polymerization. The schematic diagram of the principle behind gel formation is illustrated in Figures 1(b) and 1(c). Under UV light irradiation and the action of the DEAP catalyst, the polymer matrix was cross-linked into a porous network structure.

3. Material Nonlinearity and Parameters

The morphological analysis of the freeze-dried sample by scanning electron microscopy (SEM) showed that a porous microstructure was present throughout the ionogel. Distilled water was used to replace the internal ionic liquid in the ILG after freeze-drying treatment, and then, an S4800 Hitachi high-resolution field-emission scanning electron microscope was used to scan the sample. Figure 2 shows the spatial structure of the ionic liquid carrier HEMA for the typical 3D porous structure with a 5000x magnification, in which its matrix is cross-linked to generate a 3D support skeleton, offering good mechanical strength and self-repairing performance. Due to the porous 3D network in the ionogel, gelled BMIMBF₄ retains a relatively high ionic conductivity.

3.1. Hyperelastic Hypothesis. Assuming that the ILG is an isotropic, incompressible, hyperelastic body, the following

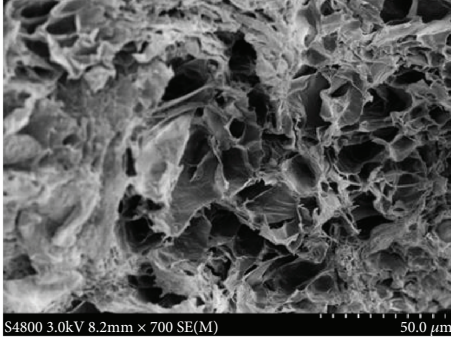


FIGURE 2: SEM image of a freeze-dried BMIMBF₄-based gel after replacing the ionic liquid with water [17].

assumptions can be made based on the theory of continuum mechanics to study its mechanical properties.

- (1) The strain energy function W of a unit mass of material is an analytic function of the strain tensor of the natural state, termed the hyperelastic hypothesis. If the rate of change of W is equal to the power of the stress, then the material is a hyperelastic material. The mechanical properties of a hyperelastic material are described by the strain energy density function W , which has many functions.
- (2) Isotropy can be assumed.
- (3) The volume of the material before and after deformation can be assumed to be the same.

λ_1 , λ_2 , and λ_3 are set as the x , y , and z directions of the main (extension) deformation rate, respectively, given by

$$\begin{aligned}\lambda_1 &= \frac{x}{x_0}, \\ \lambda_2 &= \frac{y}{y_0}, \\ \lambda_3 &= \frac{d}{d_0},\end{aligned}\quad (1)$$

where x , y , and d are the length, width, and thickness, respectively, and x_0 , y_0 , and d_0 are the corresponding initial values before deformation.

Because the material is incompressible, its volume is the same before and after deformation, giving

$$xyd = x_0y_0d_0, \quad (2)$$

namely,

$$\frac{xyd}{x_0y_0d_0} = \lambda_1\lambda_2\lambda_3 = 1. \quad (3)$$

3.2. Hyperelastic Stress. Considering the mechanical performance requirements for potential applications, three kinds of deformation states should be examined: Figure 3(a) shows the uniaxial tensile stress, Figure 3(b) shows uniform pre-stretching in the X and Y directions, and Figure 3(c) shows the Maxwell stress increased along the thickness.

The physical properties are mainly expressed by the strain energy function, and each model is a special form of this function [21–23]. Once the form of the strain energy function W is determined, the Cauchy stress tensor \mathbf{P} can be given by

$$\boldsymbol{\sigma} = -p\mathbf{I} + 2\frac{\partial W}{\partial I_1}B - 2\frac{\partial W}{\partial I_2}B^{-1}, \quad (4)$$

where \mathbf{I} is the unit tensor, which is the left Gauss deformation tensor, and p is the hydrostatic pressure resulting from the assumption of incompressibility.

$$\begin{aligned}I_1 &= B, \\ I_2 &= \frac{1}{2}[I_1^2 - t_r(B^2)], \\ I_3 &= \det B,\end{aligned}\quad (5)$$

where B is the component of the Green strain tensor. The relationship between the invariants and the principal elongation is of a function of B .

$$\begin{aligned}I_1 &= t_r[B] = B_{ii} = \lambda_1^2 + \lambda_2^2 + \lambda_3^2, \\ I_2 &= \frac{1}{2}(t_r[B])^2 - (t_r[B])^2 = \frac{1}{2}(B_{ii}B_{ii} - B_{ij}B_{ji}) \\ &= \lambda_1^2\lambda_2^2 + \lambda_2^2\lambda_3^2 + \lambda_3^2\lambda_1^2 = \frac{1}{\lambda_1^2} + \frac{1}{\lambda_2^2} + \frac{1}{\lambda_3^2}, \\ I_3 &= \det B = \lambda_1^2\lambda_2^2\lambda_3^2.\end{aligned}\quad (6)$$

Hence, the isotropic and incompressible deformation process of an ILG is given as

$$\sqrt{I_3} = \lambda_1\lambda_2\lambda_3 = 1. \quad (7)$$

According to (4) and (6), we can obtain

$$\sigma_i = 2\lambda_i^2 \left[\frac{\partial W}{\partial I_1} - \frac{1}{\lambda_i^2} \frac{\partial W}{\partial I_2} \right] - p, \quad (8)$$

where I_1 , I_2 , and I_3 are the relative changes in the length, surface area, and volume of the elastomer, respectively.

3.3. Mooney-Rivlin Model. The Mooney-Rivlin model was chosen after comparing various hyperelastic constitutive models. The mechanical properties of ionic gel materials can be studied by using the Mooney-Rivlin formula, which is considered to be a nonlinear finite element of ionic gels in this study [24–26].

The strain energy function in the Mooney-Rivlin model equation is as follows:

$$W = \sum_{i \neq j}^n c_{ij}(I_1 - 3)^i(I_2 - 3)^j, \quad (9)$$

where c_{ij} is a constant.

The Mooney-Rivlin model is the most widely used strain energy function in the finite element method. It assumes that the strain energy density is a first-order function of the principal strain constant. Under large deformations, the

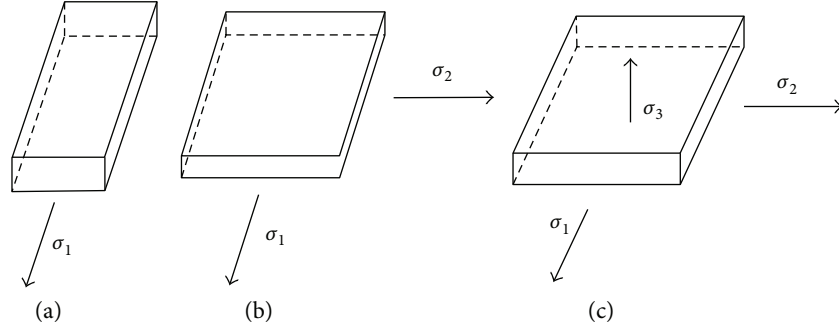


FIGURE 3: Analyses of the stress in different states.

mechanical properties of the ILG, as an incompressible hyperelastic material, are described.

3.4. Selection of the Constitutive Model for the ILG. Yeoh noted that the practical value of the higher-order strain energy function is small because the reproducibility of the ILG material is not sufficient and does not allow accurate estimation of a large number of parameters [27].

Due to its simplicity and practicality, the Mooney-Rivlin model is widely used in finite element analysis. The first-order Mooney-Rivlin model describes the mechanical properties of incompressible hyperelastic materials under large deformation. The higher-order Mooney-Rivlin model can obtain a good approximation for the solution of large strain.

The mechanical response of the hyperelastic material model is determined by the strain energy density function. The Mooney-Rivlin constant of the material must be accurately evaluated to obtain a reliable result from the hyperelastic analysis. In finite element analysis, the hyperelastic material is generally assumed to be a homogeneous isotropic material whose elastic modulus (Young's modulus) E , initial shear modulus G_0 , and Poisson's ratio ν satisfy the following relationship [28, 29].

$$E = 2G_0(1 + \nu). \quad (10)$$

4. Stress Calculation

4.1. Uniaxial Tension (State I)

4.1.1. Five-Parameter Mooney-Rivlin Model. From (9), the strain energy equation in the five-parameter Mooney-Rivlin model can be written as

$$W = c_{10}(I_1 - 3) + c_{01}(I_2 - 3) + c_{20}(I_1 - 3)^2 + c_{11}(I_1 - 3)(I_2 - 3) + c_{02}(I_2 - 3)^2. \quad (11)$$

From (8), we get

$$\sigma_i = 2 \left(\lambda_i^2 \frac{\partial W}{\partial I_1} - \frac{1}{\lambda_i^2} \frac{\partial W}{\partial I_2} \right) - p. \quad (12)$$

The stresses in all directions are

$$\sigma_1 = 2 \left(\lambda_1^2 \frac{\partial W}{\partial I_1} - \frac{1}{\lambda_1^2} \frac{\partial W}{\partial I_2} \right) - p, \quad (13)$$

$$\sigma_2 = 2 \left(\lambda_2^2 \frac{\partial W}{\partial I_1} - \frac{1}{\lambda_2^2} \frac{\partial W}{\partial I_2} \right) - p, \quad (14)$$

$$\sigma_3 = 2 \left(\lambda_3^2 \frac{\partial W}{\partial I_1} - \frac{1}{\lambda_3^2} \frac{\partial W}{\partial I_2} \right) - p, \quad (15)$$

where $\partial W/\partial I_1$ and $\partial W/\partial I_2$ are the partial differentials in the strain energy function W for I_1 and I_2 , respectively, and σ_1 , σ_2 , and σ_3 are the stresses in the x , y , and z directions, respectively.

When uniformly stretched in the X direction, $\lambda_2 = \lambda_3$, and from (3), we get

$$\lambda_2 = \lambda_3 = \frac{1}{\sqrt{\lambda_1}}. \quad (16)$$

From (6) and (16), we obtain

$$I_1 = \lambda_1^2 + \frac{2}{\lambda_1}, \quad (17)$$

$$I_2 = \frac{1}{\lambda_1^2} + 2\lambda_1.$$

Because only axial tensile deformation is considered, the stress in the other two directions is zero.

$$\sigma_2 = \sigma_3 = 0. \quad (18)$$

From (14) or (15) and (16), we obtain

$$p = 2 \left(\frac{1}{\lambda_1} \frac{\partial W}{\partial I_1} - \lambda_1 \frac{\partial W}{\partial I_2} \right). \quad (19)$$

Substituting (19) into (13),

$$\sigma_1 = 2 \left(\lambda_1^2 - \frac{1}{\lambda_1} \right) \left(\frac{\partial W}{\partial I_1} + \frac{1}{\lambda_1} \frac{\partial W}{\partial I_2} \right). \quad (20)$$

For (11), the partial differentials of the strain energy function W for I_1 and I_2 are given by

$$\frac{\partial W}{\partial I_1} = c_{10} + 2c_{02}(I_1 - 3) + c_{11}(I_2 - 3), \quad (21)$$

$$\frac{\partial W}{\partial I_2} = c_{01} + 2c_{02}(I_2 - 3) + c_{11}(I_1 - 3).$$

Therefore,

$$\sigma_1 = 2 \left(\lambda_1^2 - \frac{1}{\lambda_1} \right) \left\{ c_{10} + 2c_{02}(I_1 - 3) + c_{11}(I_2 - 3) + \frac{1}{\lambda_1} [c_{01} + 2c_{02}(I_2 - 3) + c_{11}(I_1 - 3)] \right\}. \quad (22)$$

$$\lambda_1 = \lambda_2 = \frac{1}{\sqrt{\lambda_3}}. \quad (31)$$

From (6) and (31), we get

$$I_1 = 2\lambda_1^2 + \frac{2}{\lambda_1^4}, \quad (32)$$

$$I_2 = \frac{2}{\lambda_1^2} + \lambda_1^4.$$

4.1.2. *Nine-Parameter Mooney-Rivlin Model.* From (9), the strain energy equation in the nine-parameter Mooney-Rivlin model is

$$W = c_{10}(I_1 - 3) + c_{01}(I_2 - 3) + c_{20}(I_1 - 3)^2 + c_{11}(I_1 - 3)(I_2 - 3) + c_{02}(I_2 - 3)^2 + c_{30}(I_1 - 3)^3 + c_{21}(I_1 - 3)^2(I_2 - 3) + c_{12}(I_1 - 3)(I_2 - 3)^2 + c_{03}(I_2 - 3)^3. \quad (23)$$

For (23), the partial differentials of the strain energy function W for I_1 and I_2 are given by

$$\frac{\partial W}{\partial I_1} = c_{10} + 2c_{20}(I_1 - 3) + c_{11}(I_2 - 3) + 3c_{30}(I_1 - 3)^2 + 2c_{21}(I_1 - 3)(I_2 - 3) + c_{12}(I_2 - 3)^2 = M,$$

$$\frac{\partial W}{\partial I_2} = c_{01} + 2c_{02}(I_2 - 3) + c_{11}(I_1 - 3) + 3c_{03}(I_2 - 3)^2 + 2c_{12}(I_1 - 3)(I_2 - 3) + c_{21}(I_1 - 3)^2 = N. \quad (24)$$

Therefore,

$$\sigma_1 = 2 \left(\lambda_1^2 - \frac{1}{\lambda_1} \right) \left(M + \frac{1}{\lambda_1} N \right). \quad (25)$$

4.2. Evenly Stretched in the X and Y Directions (State II)

4.2.1. *Five-Parameter Mooney-Rivlin Model.* From (9), the strain energy equation in the five-parameter Mooney-Rivlin model is

$$W = c_{10}(I_1 - 3) + c_{01}(I_2 - 3) + c_{20}(I_1 - 3)^2 + c_{11}(I_1 - 3)(I_2 - 3) + c_{02}(I_2 - 3)^2. \quad (26)$$

From (8), we get

$$\sigma_i = 2 \left(\lambda_i^2 \frac{\partial W}{\partial I_1} - \frac{1}{\lambda_i^2} \frac{\partial W}{\partial I_2} \right) - p. \quad (27)$$

The stresses in all directions are

$$\sigma_1 = 2 \left(\lambda_1^2 \frac{\partial W}{\partial I_1} - \frac{1}{\lambda_1^2} \frac{\partial W}{\partial I_2} \right) - p, \quad (28)$$

$$\sigma_2 = 2 \left(\lambda_2^2 \frac{\partial W}{\partial I_1} - \frac{1}{\lambda_2^2} \frac{\partial W}{\partial I_2} \right) - p, \quad (29)$$

$$\sigma_3 = 2 \left(\lambda_3^2 \frac{\partial W}{\partial I_1} - \frac{1}{\lambda_3^2} \frac{\partial W}{\partial I_2} \right) - p. \quad (30)$$

When uniformly stretched in the X and Y directions, $\lambda_1 = \lambda_2$, and from (3), we obtain

Because tensile deformations are only considered in the X and Y directions, the stress in the thickness direction is zero.

$$\sigma_1 = \sigma_2, \quad (33)$$

$$\sigma_3 = 0.$$

From (28) or (29) and (31), we obtain

$$p = 2 \left(\frac{1}{\lambda_1^4} \frac{\partial W}{\partial I_1} - \lambda_1^4 \frac{\partial W}{\partial I_2} \right). \quad (34)$$

Substituting (34) into (28) or (29),

$$\sigma_1 = \sigma_2 = 2 \left(\lambda_1^2 - \frac{1}{\lambda_1^4} \right) \left(\frac{\partial W}{\partial I_1} + \lambda_1^2 \frac{\partial W}{\partial I_2} \right). \quad (35)$$

For (26), the partial differentials of the strain energy function W for I_1 and I_2 are given by

$$\frac{\partial W}{\partial I_1} = c_{10} + 2c_{20}(I_1 - 3) + c_{11}(I_2 - 3), \quad (36)$$

$$\frac{\partial W}{\partial I_2} = c_{01} + 2c_{02}(I_2 - 3) + c_{11}(I_1 - 3).$$

Therefore,

$$\sigma_1 = \sigma_2 = 2 \left(\lambda_1^2 - \frac{1}{\lambda_1^4} \right) \cdot \{ c_{10} + 2c_{02}(I_1 - 3) + c_{11}(I_2 - 3) + \lambda_1^2 [c_{01} + 2c_{02}(I_2 - 3) + c_{11}(I_1 - 3)] \}. \quad (37)$$

4.2.2. *Nine-Parameter Mooney-Rivlin Model.* From (9), the strain energy equation of the nine-parameter Mooney-Rivlin model is

$$W = c_{10}(I_1 - 3) + c_{01}(I_2 - 3) + c_{20}(I_1 - 3)^2 + c_{11}(I_1 - 3)(I_2 - 3) + c_{02}(I_2 - 3)^2 + c_{30}(I_1 - 3)^3 + c_{21}(I_1 - 3)^2(I_2 - 3) + c_{12}(I_1 - 3)(I_2 - 3)^2 + c_{03}(I_2 - 3)^3. \quad (38)$$

For (38), the partial differentials of the strain energy function W for I_1 and I_2 are given by

$$\begin{aligned} \frac{\partial W}{\partial I_1} &= c_{10} + 2c_{20}(I_1 - 3) + c_{11}(I_2 - 3) + 3c_{30}(I_1 - 3)^2 \\ &\quad + 2c_{21}(I_1 - 3)(I_2 - 3) + c_{12}(I_2 - 3)^2 = M. \end{aligned} \quad (39)$$

$$\begin{aligned} \frac{\partial W}{\partial I_2} &= c_{01} + 2c_{02}(I_2 - 3) + c_{11}(I_1 - 3) + 3c_{03}(I_2 - 3)^2 \\ &\quad + 2c_{12}(I_1 - 3)(I_2 - 3) + c_{21}(I_1 - 3)^2 = N. \end{aligned}$$

Therefore,

$$\sigma_1 = \sigma_2 = 2 \left(\lambda_1^2 - \frac{1}{\lambda_1^4} \right) (M + \lambda_1^2 N). \quad (40)$$

4.3. *Applied Maxwell Stress Loading (State III)*. The Maxwell stress can be written as

$$p = -\varsigma \varsigma_0 V^2 = -\varsigma \varsigma_0 \frac{u^2}{d^2}, \quad (41)$$

where ς is the insulation constant, ς_0 is the vacuum dielectric constant (8.85×10^{-12} F/m), V is the electric field intensity, and u is the voltage.

4.3.1. *Five-Parameter Mooney-Rivlin Model*. From (9), the strain energy equation in the five-parameter Mooney-Rivlin model is

$$\begin{aligned} W &= c_{10}(I_1 - 3) + c_{01}(I_2 - 3) + c_{20}(I_1 - 3)^2 \\ &\quad + c_{11}(I_1 - 3)(I_2 - 3) + c_{02}(I_2 - 3)^2. \end{aligned} \quad (42)$$

From (8), we get

$$\sigma_i = 2 \left(\lambda_i^2 \frac{\partial W}{\partial I_1} - \frac{1}{\lambda_i^2} \frac{\partial W}{\partial I_2} \right) - p. \quad (43)$$

The stresses in all directions are

$$\sigma_1 = 2 \left(\lambda_1^2 \frac{\partial W}{\partial I_1} - \frac{1}{\lambda_1^2} \frac{\partial W}{\partial I_2} \right) - p, \quad (44)$$

$$\sigma_2 = 2 \left(\lambda_2^2 \frac{\partial W}{\partial I_1} - \frac{1}{\lambda_2^2} \frac{\partial W}{\partial I_2} \right) - p, \quad (45)$$

$$\sigma_3 = 2 \left(\lambda_3^2 \frac{\partial W}{\partial I_1} - \frac{1}{\lambda_3^2} \frac{\partial W}{\partial I_2} \right) - p. \quad (46)$$

When the Maxwell stress is loaded, namely, $\lambda_1 = \lambda_2$, (3) gives

$$\lambda_1 = \lambda_2 = \frac{1}{\sqrt{\lambda_3}}. \quad (47)$$

From (6) and (45), we get

$$I_1 = 2\lambda_1^2 + \frac{2}{\lambda_1^4}, \quad (48)$$

$$I_2 = \frac{2}{\lambda_1^2} + \lambda_1^4.$$

For (42), the partial differentials of the strain energy function W for I_1 and I_2 are given by

$$\frac{\partial W}{\partial I_1} = c_{10} + 2c_{20}(I_1 - 3) + c_{11}(I_2 - 3), \quad (49)$$

$$\frac{\partial W}{\partial I_2} = c_{01} + 2c_{02}(I_2 - 3) + c_{11}(I_1 - 3).$$

Because the materials uniformly stretched in the X and Y directions,

$$\sigma_1 = \sigma_2. \quad (50)$$

From (41), we obtain

$$\sigma_3 = -\varsigma \varsigma_0 V^2 = -\varsigma \varsigma_0 \frac{u^2}{d^2} = -\varsigma \varsigma_0 \frac{u^2}{(\lambda_3 d_0)^2}. \quad (51)$$

Substituting (49), (50), and (51) into (44) and (46),

$$\begin{aligned} \sigma_1 = \sigma_2 &= 2 \left\{ \lambda_1^2 [c_{10} + 2c_{20}(I_1 - 3) + c_{11}(I_2 - 3)] \right. \\ &\quad \left. - \frac{1}{\lambda_1^2} [c_{01} + 2c_{02}(I_2 - 3) + c_{11}(I_1 - 3)] \right\} - p, \end{aligned} \quad (52)$$

$$\begin{aligned} \sigma_3 &= 2 \left\{ \frac{1}{\lambda_1^4} [c_{10} + 2c_{20}(I_1 - 3) + c_{11}(I_2 - 3)] \right. \\ &\quad \left. - \lambda_1^4 [c_{01} + 2c_{02}(I_2 - 3) + c_{11}(I_1 - 3)] \right\} - p, \end{aligned} \quad (53)$$

$$\sigma_3 = -\varsigma \varsigma_0 \frac{u^2}{(\lambda_3 d_0)^2} = -\varsigma \varsigma_0 \frac{\lambda_1^4 u^2}{d_0^2}. \quad (54)$$

From (53) and (54),

$$\begin{aligned} p &= 2 \left\{ \frac{1}{\lambda_1^4} [c_{10} + 2c_{20}(I_1 - 3) + c_{11}(I_2 - 3)] \right. \\ &\quad \left. - \lambda_1^4 [c_{01} + 2c_{02}(I_2 - 3) + c_{11}(I_1 - 3)] \right\} \\ &\quad + \varsigma \varsigma_0 \frac{\lambda_1^4 u^2}{d_0^2}. \end{aligned} \quad (55)$$

Therefore,

$$\begin{aligned} \sigma_1 = \sigma_2 &= 2 \left\{ \lambda_1^2 [c_{10} + 2c_{20}(I_1 - 3) + c_{11}(I_2 - 3)] \right. \\ &\quad \left. - \frac{1}{\lambda_1^2} [c_{01} + 2c_{02}(I_2 - 3) + c_{11}(I_1 - 3)] \right\} \\ &\quad - 2 \left\{ \frac{1}{\lambda_1^4} [c_{10} + 2c_{20}(I_1 - 3) + c_{11}(I_2 - 3)] \right. \\ &\quad \left. - \lambda_1^4 [c_{01} + 2c_{02}(I_2 - 3) + c_{11}(I_1 - 3)] \right\} \\ &\quad - \varsigma \varsigma_0 \frac{\lambda_1^4 u^2}{d_0^2}, \end{aligned} \quad (56)$$

$$\sigma_3 = -\varsigma \varsigma_0 \frac{\lambda_1^4 u^2}{d_0^2}.$$

4.3.2. *Nine-Parameter Mooney-Rivlin Model.* From (9), the strain energy equation in the nine-parameter Mooney-Rivlin model is

$$\begin{aligned} W = & c_{10}(I_1 - 3) + c_{01}(I_2 - 3) + c_{20}(I_1 - 3)^2 \\ & + c_{11}(I_1 - 3)(I_2 - 3) + c_{02}(I_2 - 3)^2 \\ & + c_{30}(I_1 - 3)^3 + c_{21}(I_1 - 3)^2(I_2 - 3) \\ & + c_{12}(I_1 - 3)(I_2 - 3)^2 + c_{03}(I_2 - 3)^3. \end{aligned} \quad (57)$$

For (57), the partial differentials of the strain energy function W for I_1 and I_2 are given by

$$\begin{aligned} \frac{\partial W}{\partial I_1} = & c_{10} + 2c_{20}(I_1 - 3) + c_{11}(I_2 - 3) + 3c_{30}(I_1 - 3)^2 \\ & + 2c_{21}(I_1 - 3)(I_2 - 3) + c_{12}(I_2 - 3)^2 = M, \\ \frac{\partial W}{\partial I_2} = & c_{01} + 2c_{02}(I_2 - 3) + c_{11}(I_1 - 3) + 3c_{03}(I_2 - 3)^2 \\ & + 2c_{12}(I_1 - 3)(I_2 - 3) + c_{21}(I_1 - 3)^2 = N. \end{aligned} \quad (58)$$

Because the materials uniformly stretched in the X and Y directions,

$$\sigma_1 = \sigma_2. \quad (59)$$

From (41),

$$\sigma_3 = -\zeta\zeta_0 V^2 = -\zeta\zeta_0 \frac{u^2}{d^2} = -\zeta\zeta_0 \frac{u^2}{(\lambda_3 d_0)^2}. \quad (60)$$

Substituting (58), (59), and (60) into (44) and (46),

$$\sigma_1 = \sigma_2 = 2 \left(\lambda_1^2 M - \frac{1}{\lambda_1^2} N \right) - p, \quad (61)$$

$$\begin{aligned} \sigma_3 = & 2 \left(\frac{1}{\lambda_1^4} M - \lambda_1^4 N \right) - p = -\zeta\zeta_0 \frac{u^2}{(\lambda_3 d_0)^2} \\ = & -\zeta\zeta_0 \frac{\lambda_1^4 u^2}{d_0^2}. \end{aligned} \quad (62)$$

From (61) and (62),

$$p = 2 \left(\frac{1}{\lambda_1^4} M - \lambda_1^4 N \right) + \zeta\zeta_0 \frac{\lambda_1^4 u^2}{d_0^2}. \quad (63)$$

Therefore,

$$\begin{aligned} \sigma_1 = \sigma_2 = & 2 \left(\lambda_1^2 M - \frac{1}{\lambda_1^2} N \right) \\ & - 2 \left(\frac{1}{\lambda_1^4} M - \lambda_1^4 N \right) - \zeta\zeta_0 \frac{\lambda_1^4 u^2}{d_0^2}, \\ \sigma_3 = & -\zeta\zeta_0 \frac{\lambda_1^4 u^2}{d_0^2}. \end{aligned} \quad (64)$$

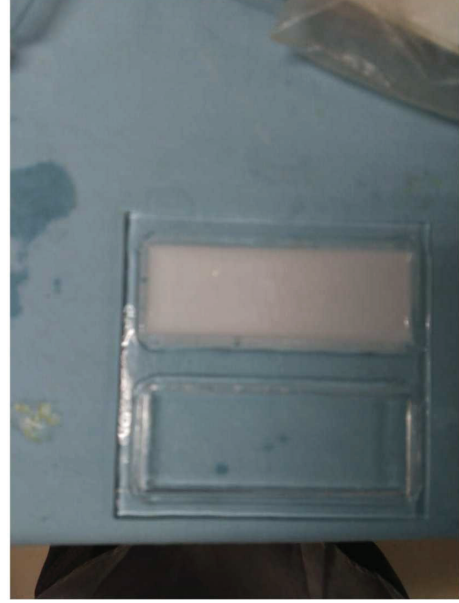


FIGURE 4: The gel after polymerization under a UV lamp.

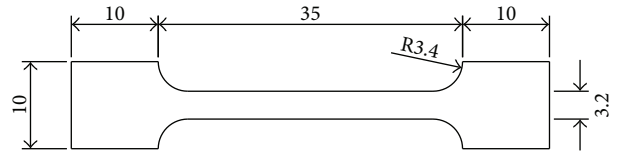


FIGURE 5: Test sample size (in mm).

5. Experimental Analysis

5.1. *Production of Tensile Test Sample.* The prepared solution was poured into a mold and polymerized into a gel under the irradiation of a UV lamp. The gel is white in color and is filled in the transparent glass mold as shown in Figure 4. Then, the sample was cut to the size shown in Figure 5, with a thickness of 3.4 mm. As shown in Figure 6, the experimental instrument was a UTM2502 electronic universal testing machine. The mechanical sensor on the testing machine can achieve a precision of 0.1 mN, the displacement sensor has a precision of 0.001 mm, and the stretching rate is 500 mm/min.

5.2. *Experimental Results.* As seen from Figure 6, the ILG becomes longer and thinner as the load increases, which is consistent with the assumption that the material is incompressible.

The tensile stress-strain curve of the ILG is shown in Figure 7, and the average tensile strength (Young's modulus) of the material obtained from the tensile stress-strain curve is 7.6 kPa.

In the ionogel, BMIMBF₄ exhibits a high level of hyperelastic toughness when the tensile deformation reaches 360%. The tensile test showed that the tensile properties of the gel increased with an increase in ZrO₂ content. The increase in ZrO₂ content should generate more cross-linking sites and higher conversion rates (shown in Figure 2), which contributes to the overall mechanical properties. As the content of

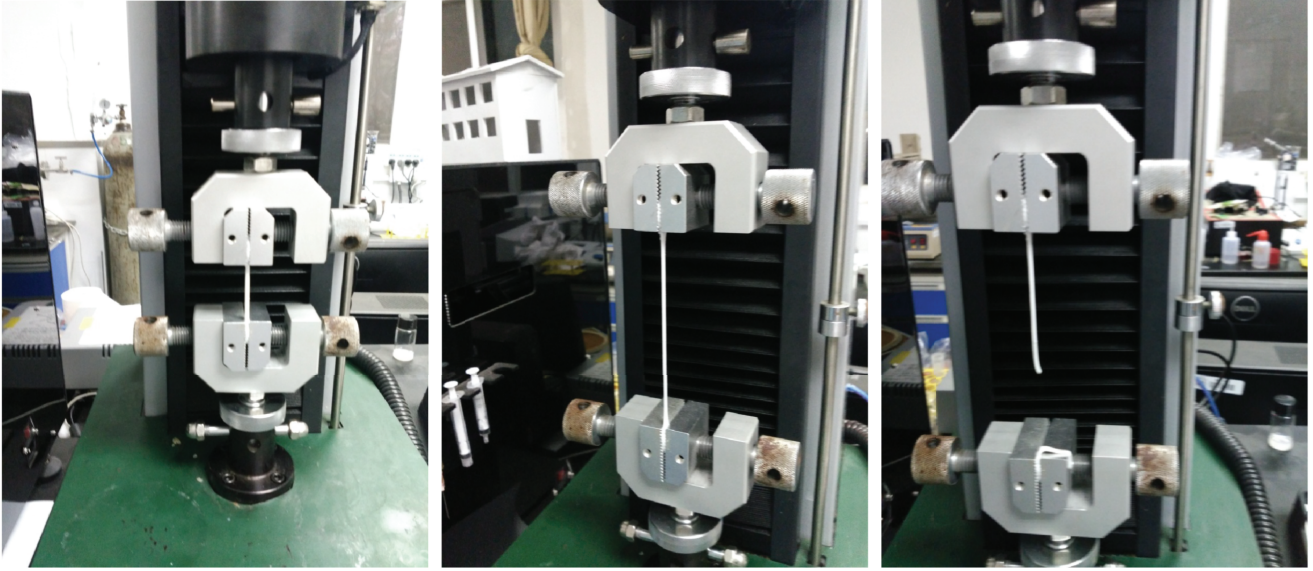


FIGURE 6: Uniaxial tensile test.

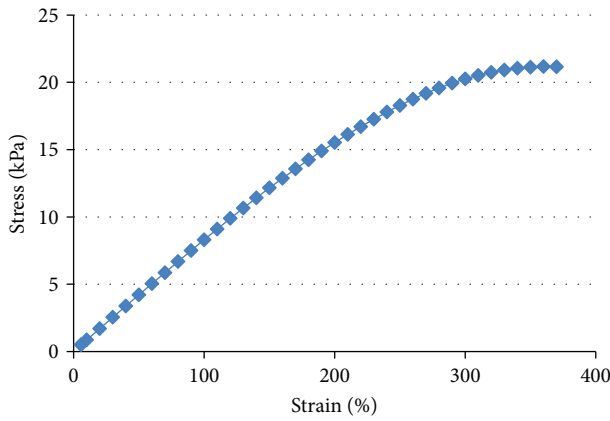


FIGURE 7: Stress-strain curve of the ionic liquid gel polymer.

ZrO_2 increases, the tensile strength of the ILG increases, while the elongation rate decreases. Considering the above data, the optimum amount of ZrO_2 to provide a large tensile strain and tensile strength is 3 wt%.

5.3. Stress Calculation. The relationship between the real stress σ_i and engineering stress σ_E is

$$\sigma_i = \sigma_E \lambda, \quad (65)$$

where σ_i is the true stress and σ_E is the engineering stress. The calculated stress given in Table 1 is the engineering stress.

We next tested whether the above-derived engineering stress expression for the ILG is accurate and whether it can be used for the design of an ILG actuator or sensor. To verify the accuracy and practicability of the induced stress expression of the ILG, the deformation rate at each point in the uniaxial tensile test was substituted into the engineering stress expression to calculate the engineering stress. A comparison

of the calculated uniaxial tensile stress with the experimental data is given in Table 1.

For the five-parameter Mooney-Rivlin model, the parameters c_{10} , c_{01} , c_{20} , c_{11} , and c_{02} are as follows.

$$\begin{aligned} c_{10} &= 2.3582, \\ c_{01} &= -0.87482, \\ c_{20} &= -0.066187, \\ c_{11} &= 0.19663, \\ c_{02} &= 0.21939. \end{aligned} \quad (66)$$

For the nine-parameter Mooney-Rivlin model, the parameters c_{10} , c_{01} , c_{20} , c_{11} , c_{02} , c_{30} , c_{21} , c_{12} , and c_{03} are as follows.

$$\begin{aligned} c_{10} &= 0.55361, \\ c_{01} &= 1.0009, \\ c_{20} &= 130.08, \\ c_{11} &= -270.06, \\ c_{02} &= 142.91, \\ c_{30} &= 0.014438, \\ c_{21} &= -0.17711, \\ c_{12} &= -31.71, \\ c_{03} &= 17.028. \end{aligned} \quad (67)$$

As seen from Table 1 in the comparisons of the calculated tensile stress with the experimental data, the relative error of the five-parameter Mooney-Rivlin model is less than 0.51% and the relative error of the nine-parameter Mooney-Rivlin model is no more than 8.87%.

TABLE 1: Comparison of the calculated tensile stress with the experimental data from the uniaxial tensile test.

Measurement data		Experimental results		Five-parameter Mooney-Rivlin model		Nine-parameter Mooney-Rivlin model	
Force (mN)	Deformation (mm)	Strain (%)	Stress (kPa)	Calculated stress (σ_E) (kPa)	Error (%)	Calculated stress (σ_E) (kPa)	Error (%)
4.97	2.0	5.7	0.50	0.50	0.46	0.50	0.00
8.21	3.5	10	0.86	0.86	0.51	0.86	0.07
14.88	7.0	20	1.70	1.70	0.26	1.70	0.03
20.52	10.5	30	2.54	2.54	0.06	2.55	0.26
25.35	14.0	40	3.38	3.37	0.24	3.39	0.29
29.47	17.5	50	4.21	4.21	0.13	4.23	0.44
33.06	21.0	60	5.04	5.04	0.09	5.07	0.49
36.22	24.5	70	5.86	5.86	0.05	5.90	0.68
38.94	28.0	80	6.68	6.69	0.07	6.73	0.8
41.48	31.5	90	7.50	7.50	0.01	7.57	0.87
43.58	35.0	100	8.30	8.30	0.05	8.39	1.10
45.50	38.5	110	9.10	9.10	0.01	9.21	1.21
47.13	42.0	120	9.88	9.88	0.02	10.02	1.41
48.67	45.5	130	10.65	10.65	0.01	10.82	1.57
49.98	49.0	140	11.41	11.41	0.04	11.60	1.67
51.03	52.5	150	12.15	12.14	0.06	12.37	1.80
51.95	56.0	160	12.86	12.86	0.01	13.12	2.03
52.75	59.5	170	13.56	13.56	0.01	13.86	2.19
53.40	63.0	180	14.24	14.24	0.0	14.58	2.35
53.90	66.5	190	14.89	14.90	0.05	15.27	2.58
54.32	70.0	200	15.52	15.53	0.06	15.95	2.79
54.65	73.5	210	16.12	16.14	0.11	16.61	3.05
54.78	77.0	220	16.70	16.72	0.10	17.25	3.29
54.86	80.5	230	17.25	17.27	0.11	17.86	3.55
54.94	84.0	240	17.78	17.79	0.07	18.45	3.78
54.84	87.5	250	18.28	18.28	0.01	19.02	4.02
54.72	91.0	260	18.74	18.74	0.00	19.55	4.32
54.47	94.5	270	19.18	19.16	0.08	20.05	4.56
54.01	98.0	280	19.57	19.55	0.09	20.53	4.89
53.61	101.5	290	19.93	19.90	0.14	20.97	5.19
53.23	105.0	300	20.24	20.21	0.13	21.37	5.57
52.48	108.5	310	20.50	20.49	0.07	21.73	6.00
51.83	112.0	320	20.73	20.71	0.08	22.05	6.38
51.02	115.5	330	20.91	20.90	0.05	22.34	6.81
50.29	119.0	340	21.04	21.04	0.01	22.57	7.29
49.21	122.5	350	21.12	21.13	0.06	22.77	7.80
48.25	126.0	360	21.16	21.18	0.08	22.92	8.31
47.17	129.5	370	21.15	21.17	0.10	23.03	8.87

Figure 8 shows that the stress-strain curve calculated by the five-parameter model almost coincides with the experimental curve. The first half of the stress-strain curve calculated by the nine-parameter model almost coincides with the experimental curve, while in the second half, the error between the stress-strain curve calculated by the nine-parameter model and the experimental curve becomes increasingly larger, but the error remains small.

The above analyses indicate that the simulated values are consistent with the experimental values, making our derivation a feasible and credible stress formula for the calculation of the ILG properties.

Due to our current laboratory conditions, only the uniaxial tensile test was performed. The next step is to improve the laboratory conditions in order to carry out the plane uniform tensile test and the Maxwell stress experiments. Further

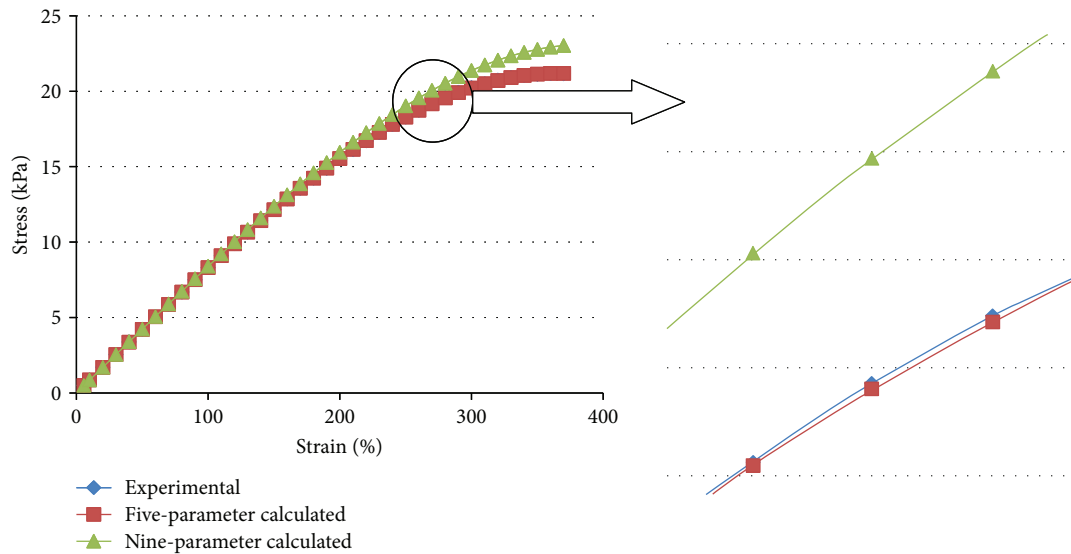


FIGURE 8: Comparison of the calculated tensile stress with the experimental data from the uniaxial tensile test.

studies of the five-parameter and nine-parameter Mooney-Rivlin models will be carried out.

6. Conclusions

In this paper, an ILG is modeled by the hyperelastic nonlinear finite element model. The simulation results show that the Mooney-Rivlin model can well adapt to the constitutive relation of the material [30, 31]. The main advantage of the ILG is that the stress-strain curve can be obtained by the performance parameters of the material in a relatively short time, which provides a theoretical basis for the optimal design of a soft robot.

The simulation results show that the average error between the calculated data and the experimental data is small, and the model has a good correlation with the experimental data. The model requires the input of the ILG material parameters. A standard uniaxial stretching method is used to obtain the desired ILG material parameters.

In the future, we will seek a generalized algorithm for identifying the ILG mechanical properties. Notably, all the results of this study show that there is a good correlation between the 3D theoretical assumptions and the experimental conditions, which proves that our method can be used to optimize the design of a soft robot. This work opens a new path to study the performance of ILG soft actuators, which will be the direction of future work.

Conflicts of Interest

The authors declare that there is no conflict of interests regarding the publication of this paper.

Acknowledgments

The work was supported by the National Natural Science Foundation of China (Grant no. 51605334), the Shanghai Sailing Program of China (Grant no. 17YF1420200), and

the Tongji University Young Excellent Talents Program of China (Grant no. 0800219344). The authors would like to thank the reviewers for their helpful comments on the manuscript.

References

- [1] T. Fukushima, K. Asaka, A. Kosaka, and T. Aida, "Fully plastic actuator through layer-by-layer casting with ionic-liquid-based bucky gel," *Angewandte Chemie International Edition*, vol. 44, no. 16, pp. 2410–2413, 2005.
- [2] K. Kruusamäe, K. Mukai, T. Sugino, and K. Asaka, "Mechanical behaviour of bending bucky-gel actuators and its representation," *Smart Materials & Structures*, vol. 23, no. 2, article 025031, 2014.
- [3] Q. He, M. Yu, X. Yang, K. J. Kim, and Z. Dai, "An ionic electroactive actuator made with graphene film electrode, chitosan and ionic liquid," *Smart Materials and Structures*, vol. 24, no. 6, article 065026, 2015.
- [4] R. Pelrine, R. Kornbluh, Q. Pei, and J. Joseph, "High-speed electrically actuated elastomers with strain greater than 100%," *Science*, vol. 287, no. 5454, pp. 836–839, 2000.
- [5] M. L. Hammock, A. Chortos, B. C.-K. Tee, J. B.-H. Tok, and Z. Bao, "25th anniversary article: the evolution of electronic skin (E-skin): a brief history, design considerations, and recent progress," *Advanced Materials*, vol. 25, no. 42, pp. 5997–6038, 2013.
- [6] A. W. Feinberg, A. Feigel, S. S. Shevkoplyas, S. Sheehy, G. M. Whitesides, and K. K. Parker, "Muscular thin films for building actuators and powering devices," *Science*, vol. 317, no. 5843, pp. 1366–1370, 2007.
- [7] G. Liu, A. Wang, X. Wang, and P. Liu, "A review of artificial lateral line in sensor fabrication and bionic applications for robot fish," *Applied Bionics and Biomechanics*, vol. 2016, Article ID 4732703, 15 pages, 2016.
- [8] N. Buchtová, A. Guyomard-Lack, and J. Le Bideau, "Biopolymer based nanocomposite ionogels: high performance, sustainable and solid electrolytes," *Green Chemistry*, vol. 16, no. 3, pp. 1149–1152, 2014.

- [9] J. Le Bideau, L. Viau, and A. Vioux, "Ionogels, ionic liquid based hybrid materials," *Chemical Society Reviews*, vol. 40, no. 2, pp. 907–925, 2011.
- [10] W. Zhang, L. Chen, J. Zhang, and Z. Huang, "Design and optimization of carbon nanotube/polymer actuator by using finite element analysis," *Chinese Physics B*, vol. 26, no. 4, article 048801, 2017.
- [11] M. Zhang, D. Xu, X. Yan et al., "Self-healing supramolecular gels formed by crown ether based host-guest interactions," *Angewandte Chemie, International Edition*, vol. 51, no. 28, pp. 7011–7015, 2012.
- [12] D. Zhang, J. Yang, S. Bao, Q. Wu, and Q. Wang, "Semiconductor nanoparticle-based hydrogels prepared via self-initiated polymerization under sunlight, even visible light," *Scientific Reports*, vol. 3, no. 1, p. 1399, 2013.
- [13] A. Leski, R. Baraniecki, and J. Malachowski, "Numerical simulation to study the influence of the thickness of canopy at a bird strike," in *DS 30: proceedings of DESIGN 2002, the 7th international design conference*, Dubrovnik, 2002.
- [14] F. He, L. Hua, and L. J. Gao, "A computational model for biomechanical effects of arterial compliance mismatch," *Applied Bionics and Biomechanics*, vol. 2015, Article ID 213236, 6 pages, 2015.
- [15] S. Lee, H. C. Park, and K. J. Kim, "Equivalent modeling for ionic polymer-metal composite actuators based on beam theories," *Smart Materials and Structures*, vol. 14, no. 6, pp. 1363–1368, 2005.
- [16] Z. Wang, B. He, Q. Wang, and Y. Yin, "Electromechanical bending behavior study of soft photocurable ionogel actuator using a new finite element method," *Smart Materials and Structures*, vol. 25, no. 9, article 095018, 2016.
- [17] B. He, C.-H. Zhang, and A. Ding, "Finite element analysis of ionic liquid gel soft actuator," *Chinese Physics B*, vol. 26, no. 12, article 126102, 2017.
- [18] S. Alexandrov and W. Miszuris, "Heat generation in plane strain compression of a thin rigid plastic layer," *Acta Mechanica*, vol. 227, no. 3, pp. 813–821, 2016.
- [19] M. Sonato, A. Piccolroaz, W. Miszuris, and G. Mishuris, "General transmission conditions for thin elasto-plastic pressure-dependent interphase between dissimilar materials," *International Journal of Solids and Structures*, vol. 64-65, pp. 9–21, 2015.
- [20] X. Liu, B. He, Z. Wang, H. Tang, T. Su, and Q. Wang, "Tough nanocomposite ionogel-based actuator exhibits robust performance," *Scientific Reports*, vol. 4, no. 1, 2015.
- [21] M. Li, Y. Yang, L. Guo, D. Chen, H. Sun, and J. Tong, "Design and analysis of bionic cutting blades using finite element method," *Applied Bionics and Biomechanics*, vol. 2015, Article ID 471347, 7 pages, 2015.
- [22] Y. Liu, L. Liu, S. Sun, and J. Leng, "Electromechanical stability of a Mooney–Rivlin-type dielectric elastomer with nonlinear variable permittivity," *Polymer International*, vol. 59, no. 3, pp. 371–377, 2010.
- [23] L. Liu, Y. Liu, K. Yu, and J. Leng, "Thermoelectromechanical stability of dielectric elastomers undergoing temperature variation," *Mechanics of Materials*, vol. 72, pp. 33–45, 2014.
- [24] K. Sangpradit, H. Liu, P. Dasgupta, K. Althoefer, and L. D. Seneviratne, "Finite-element modeling of soft tissue rolling indentation," *IEEE Transaction on Biomedical Engineering*, vol. 58, no. 12, pp. 3319–3327, 2011.
- [25] M. Prados-Privado, J. A. Bea, R. Rojo, S. A. Gehrke, J. L. Calvo-Guirado, and J. C. Prados-Frutos, "A new model to study fatigue in dental implants based on probabilistic finite elements and cumulative damage model," *Applied Bionics and Biomechanics*, vol. 2017, Article ID 3726361, 8 pages, 2017.
- [26] Y. Liu, L. Liu, Z. Zhang, Y. Jiao, S. Sun, and J. Leng, "Analysis and manufacture of an energy harvester based on a Mooney–Rivlin-type dielectric elastomer," *EPL (Europhysics Letters)*, vol. 90, no. 3, article 36004, 2010.
- [27] O. H. Yeoh, "Some forms of the strain energy function for rubber," *Rubber Chemistry and Technology*, vol. 66, no. 5, pp. 754–771, 1993.
- [28] M. Facchinetti and W. Miszuris, "Analysis of the maximum friction condition for green body forming in an ANSYS environment," *Journal of the European Ceramic Society*, vol. 36, no. 9, pp. 2295–2302, 2016.
- [29] D. Hu, B. Song, D. Wang, and Z. Chen, "Experiment and numerical simulation of a full-scale helicopter composite cockpit structure subject to a bird strike," *Composite Structures*, vol. 149, pp. 385–397, 2016.
- [30] W. Sun, E. L. Chaikof, and M. E. Levenston, "Numerical approximation of tangent moduli for finite element implementations of nonlinear hyperelastic material models," *Journal of Biomechanical Engineering*, vol. 130, no. 6, article 061003, 2008.
- [31] C. Ihueze and C. Mgbemena, "Modeling hyperelastic behavior of natural rubber/organomodified kaolin composites oleochemically derived from tea seed oils (*Camellia sinensis*) for automobile tire side walls application," *Journal of Scientific Research and Reports*, vol. 3, no. 19, pp. 2528–2542, 2014.

Research Article

The Gait Design and Trajectory Planning of a Gecko-Inspired Climbing Robot

Xuepeng Li ¹, Wei Wang ¹, Shilin Wu ², Peihua Zhu ³, Fei Zhao ¹,
and Linqing Wang ¹

¹Robotics Institute, Beihang University, Beijing 100191, China

²School of Mechanical Engineering and Automation, Beihang University, Beijing 100191, China

³FAW-Volkswagen Automotive Co., Ltd., Changchun, Jilin 130000, China

Correspondence should be addressed to Xuepeng Li; xpli613@163.com

Received 9 November 2017; Revised 22 January 2018; Accepted 5 March 2018; Published 22 April 2018

Academic Editor: QingSong He

Copyright © 2018 Xuepeng Li et al. This is an open access article distributed under the Creative Commons Attribution License, which permits unrestricted use, distribution, and reproduction in any medium, provided the original work is properly cited.

Inspired by the dynamic gait adopted by gecko, we had put forward GPL (Gecko-inspired mechanism with a Pendular waist and Linear legs) model with one passive waist and four active linear legs. To further develop dynamic gait and reduce energy consumption of climbing robot based on the GPL model, the gait design and trajectory planning are addressed in this paper. According to kinematics and dynamics of GPL, the trot gait and continuity analysis are executed. The effects of structural parameters on the supporting forces are analyzed. Moreover, the trajectory of the waist is optimized based on system energy consumption. Finally, a bioinspired robot is developed and the prototype experiment results show that the larger body length ratio, a certain elasticity of the waist joint, and the optimized trajectory contribute to a decrease in the supporting forces and reduction in system energy consumption, especially negative forces on supporting feet. Further, the results in our experiments partly explain the reasonability of quadruped reptile's kinesiography during dynamic gait.

1. Introduction

Wall-climbing robots can move and work on a vertical wall to complete various tasks, which have attracted much attention of researchers around the world and have wide application fields including antiterrorism, postdisaster rescue, engineering test, and maintenance and inspection for hazardous environment [1–4]. Compared to the wheeled robots and caterpillar robots, the multilegged climbing robots have a distinct advantage of strong adaptability to unknown environment and uneven wall. Certainly, we must own the fact that they are limited by low velocity and large energy consumption. Here, it becomes very important to address gait design and trajectory planning of multilegged climbing robots, especially for bioinspired climbing robots.

Generally, gaits of multilegged climbing robot could be classified into two kinds by leg raise sequence and stability: the quasistatic gait and dynamic gait. As the

name implies, the quasistatic gait shows that the whole robot system maintains static balance during the climbing process, which is easy to ensure the behavior of robot [5]. Many previous works have been carried out to promote development of climbing robots, such as the Climbing Mini-Whegs, the Waalbot II [6], the RiSE [7, 8], the Stintov, and the StickyBot [9, 10], characterized with pivot joints on the legs. These climbing robots can be applied in many challenging environments such as tree, glasses, cabinets, or concrete surfaces. However, their works are limited to relatively low velocities due to the quasistatic gait.

With the development of biomimetics, the dynamic gait which is closer to actual biologic locomotion has been applied to improve vertical climbing efficiency and reduce power consumption. To describe the dynamic gait, some models are abstracted from the biologic locomotion pattern, including the spring-mass (SM) model [11], the ubiquitous

Spring-Loaded Inverted Pendulum (SLIP) model, the Lateral-Leg Spring (LLS) model [12], and the F-G model [13]. As expected, the climbing robots adopting dynamic gait performed an excellent performance from the perspective of high speed and low energy cost [14, 15]. However, there are still inevitable questions about the stability of climbing motion. With the DynoClimber and ROCR as an example, the lack of supporting feet makes both of them easily rotate around the vertical axis parallel with the climbing surface and leads to the weak stability during pendulum.

Trajectory planning for multilegged climbing robots refers to two major steps. Firstly, the trajectory solution for a required motion task could be obtained based on the forward and inverse kinematics. Furthermore, it is to ensure that the final path satisfies the needs of the desired conditions, such as minimum path, time, and energy consumption. Wang et al. investigated optimal attaching and detaching trajectory for wall climbing which guarantee reliability of the climbing robot [16]. Chen et al. operated the leg trajectories of the leg-wheel hybrid robot in a periodic manner on each step during stair climbing in view of a series of similar geometry constraints and limitation of the joint power density [17]. Akinfiyev and Armada analyzed the influence of gravity on trajectory planning for climbing robots [18]. These works have improved the climbing performance of robots to a certain extent.

In our previous work, we have proposed the GPL (Gecko inspired mechanism with a Pendular waist and Linear legs) model and verified its feasibility [19]. The GPL model inspired by the F-G model consists of two rigid bodies (upper part and lower part with tail), four linear legs with spring buffers, and a passive waist joint. And it aims at explaining the relationships of the locomotion dynamics, the variables of the movement, and the parameters of the mechanism for sprawl quadruped climbing animals. To further develop dynamic gait and reduce energy consumption of climbing robots based on the GPL model, the gait design and trajectory planning will be addressed in this paper.

The organization of this paper is as follows: firstly, kinematics and dynamics of GPL are derived systematically and the conditions of gait reuse are obtained in the second section. And the singularity and feasible region of the waist are analyzed in detail. Then, the effects of structural parameters on the supporting forces are explored, including body length ratio, driving angle, and elasticity of the waist joint. Moreover, the trajectory of the waist is optimized based on system energy consumption. To testify our analysis, a bioinspired robot is developed and the prototype experiments are performed. Finally, conclusions are drawn and the future work is described.

2. Gait Design and Continuity Analysis

2.1. Kinematics and Dynamics of GPL. As illustrated in Figure 1, the GPL model abstracted from the gecko's morphology and kinesiology is composed of four linear legs L_i ($i = 1 - 4$), an upper part rigid body P_1 , a lower part rigid body P_2 , and a passive revolute joint called waist P . Here,

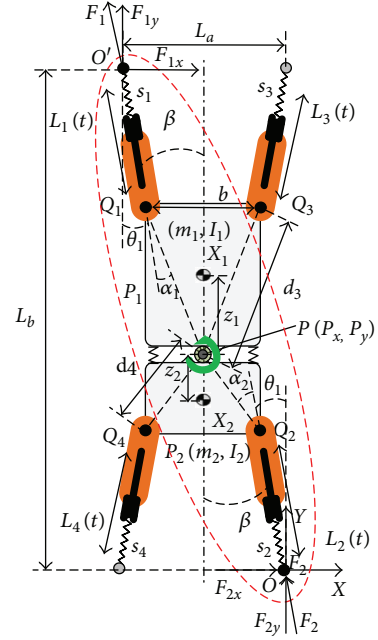


FIGURE 1: The GPL and its dynamic model derived from gecko. The red dotted line indicates the current adherent mechanism. The black dots on the foot mean the corresponding diagonal legs are attached with the climbing surface, while the gray dots mean the corresponding diagonal legs are swinging. Here, L_a and L_b are the horizontal and vertical distances between the diagonal stance feet, respectively. $L_i(t)$ and x_p denote the length of linear legs L_i and the position of P , which can be controlled. Let m_j, X_j , and I_j ($j = 1, 2$) be mass, the position of the center, and the inertia moment tensor matrix of P_j in coordinate $\{O\}$, respectively. Q_j, d_j, θ_j , and α_j denote the leg's fixed point on P_j , the distance from x_p to Q_j , the angle between leg and the vertical line, and the angle between corresponding leg and line PQ_j , respectively. B and α_j are constant values. z_j denotes the distance from x_p to the center of P_j .

the tail of the bionic prototype is very light and ignored to simplify the dynamic analysis. According to bionic research [25], the driving angle β between the driving force along the legs and the long axis of the body is almost constant during a moving cycle. Here, β keeps a constant value (10°). The front legs L_1, L_3 and rear legs L_2, L_4 are fixed on the upper and lower rigid body, respectively. Namely, the leg and the corresponding rigid body have the same angular velocity. In order to facilitate the analysis and design, waist P fixed on the upper part P_1 is treated as a reference point of locomotion for the model. The lower body can revolve about the waist freely. To imitate gecko's wrist, one passive rotary joint is designed at the end of each leg, which allows the leg to rotate on the climbing surface. The GPL's locomotion can be realized by the legs' extending or contracting motion, cooperating with alternation of feet's attachment and wring. It notes that the waist has a certain elasticity by linking two rigid bodies with two linear springs.

The trot gait inspired by gecko's climbing is adopted for the GPL model, as shown in Figure 2. One stride of the trot gait during a stable climbing movement can be divided into

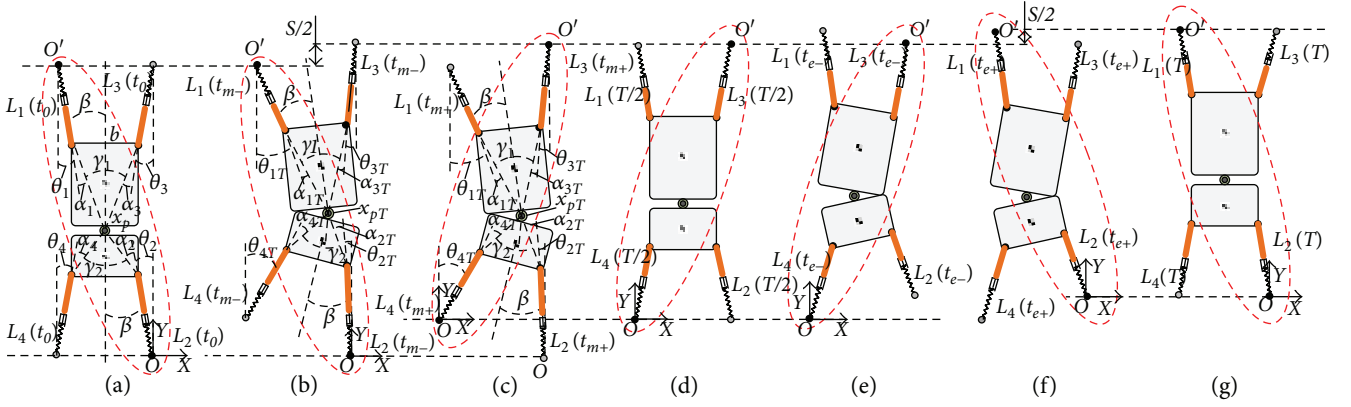


FIGURE 2: The trot gait inspired by gecko's climbing for the GPL model. Here, red dotted lines denote that the corresponding mechanisms are executing the active movement. (a)–(c) show the gait movement principle during half one gait. (a) The initial state of trot gait. L_1 and L_2 are adherent; L_3 and L_4 are swing. (b) L_1 contracts and L_2 extends; L_3 and L_4 are swing; and the waist swings as a pendulum and moves forward half stride $S/2$. (c) The role transformation of corresponding adherent and swinging diagonal feet. (d)–(e) The two processes are similar with (a) and (b). And the waist moves forward the other half stride $S/2$. (f) The role transformation status. (g) The initial state for the next gait.

two symmetrical phases. In one phase, the left front leg and the right rear leg begin to establish attachment with the climbing surface. Then, the left front leg contracts and the right rear leg extends, pulling the body upward, with other legs executing opposite motion. Meanwhile, the waist swings as a pendulum about the stance foot. Next, the other one executes the symmetrical motion.

In view of the symmetry of gait, we choose the procedure of one phase for analysis and apply the result to the next symmetrical phase, as shown by red dotted lines in Figure 1. Thus, the GPL model can be treated as a planar five-bar mechanism RPRPR with two degrees of freedom during one phase.

Let $\{O\}$ and $\{O'\}$ be a coordinate frame $O-XY$ fixed on the right rear at O and left front foot at O' , respectively. The waist P rotates with the upper part around the stance foot O' . The pose of GPL can be expressed by either $\mathbf{q}_L = [L_1 L_2]^T$, $\mathbf{x}_p = [P_x P_y]^T$, or $\mathbf{X}_j = [P_x P_y j]^T$ as below (details can be found in [20]).

$$\mathbf{x}_p = \begin{bmatrix} P_x \\ \frac{(\Phi(L_2) - \Phi(L_1) - 2L_a P_x + C)}{2} L_b \end{bmatrix}, \quad (1)$$

$$\dot{\mathbf{x}}_p = \mathbf{J} \dot{\mathbf{q}}_L,$$

$$\mathbf{X}_j = \begin{bmatrix} P_x \\ P_y \end{bmatrix} + \begin{bmatrix} \sin(\theta_j - \beta) z_j \\ (-1)^{j+1} \cos(\theta_j - \beta) z_j \end{bmatrix},$$

where \mathbf{J} is a 2×2 Jacobian matrix.

$$\mathbf{J} = \frac{1}{L_b \times P_x + L_a \times P_y} \begin{bmatrix} m P_y n & (L_b - P_y) \\ -m P_x & n(L_a + P_x) \end{bmatrix}. \quad (2)$$

Based on (1) and (2), when given the length q_L of linear legs, the position x_p of the waist can be solved and vice versa, which lays the foundation for trajectory planning.

For further dynamic analysis of GPL, driving forces on the linear legs are analyzed, which significantly determine the control and performance of the robot. According to Autumn et al.'s research [21], energy loss during a rapid locomotion was generally attributed to the deceleration forces produced by the supporting feet. In that case, gravity and the gecko's legs decelerate the climbing within each step, resulting in velocity fluctuation. Therefore, it is worth analyzing the supporting forces on foot.

Let F_j be the active force applied on the linear legs. Let E_K and E_p be the kinetic energy and potential energy of the template; it can be calculated as follows:

$$E_k(q_L, \dot{q}_L) = \frac{1}{2} \sum_1^j [I_j^2 \dot{\theta}_j + m_j (\dot{P}_{xj} + \dot{P}_{yj})], \quad (3)$$

$$E_p(q_L) = E_{ps} + E_{pg},$$

where

$$E_{ps} = \frac{1}{2} \left(k_w \sigma_w^2 + \sum_1^j k_j (L_j - L_{sj})^2 \right), \quad (4)$$

$$E_{pg} = \sum_1^j m_j g P_y.$$

Here, the E_{ps} and E_{pg} denote the elastic potential energy and the gravitational potential energy of the template, respectively. k_j is the stiffness coefficient of the axil legs L_j . k_w and σ_w are the stiffness coefficient and torsional angle of the pendular waist, respectively.

According to Lagrange dynamical equation, driving force $\boldsymbol{\tau} = [F_1 F_2]^T$, generated by the stretchout and drawback of the legs, can be calculated as follows:

$$\tau = \frac{d}{dt} \left(\frac{\partial T}{\partial \dot{q}_L} \right) - \frac{\partial T}{\partial q_L}, \quad (5)$$

$$T = E_k(q_L, \dot{q}_L) + E_p(q_L).$$

Therefore, the joint power of the robot and system energy consumption in actual application of the climbing robot can be obtained as follows:

$$P_j(t) = \frac{R_a}{k_M^2 \eta^2 N_G^2} F_j^2(t) + \frac{\dot{L}_j(t) F_j(t)}{\eta}, \quad (6)$$

$$E(t) = \sum_{j=1}^n \int_{t_0}^{t_m} P_j(t) dt \quad (j = 1, 2).$$

2.2. Condition of Gait Reuse. Generally, the gait designed for the robot has obvious periodicity in view of motion stability and control complexity. When a symmetrical gait is adopted, the trajectory planning for a step could be reused in the entire regular motion trajectory, especially linear trajectory or circle trajectory. Unlike the other quadruped robots, there is only a controllable local degree of freedom on the foot for the GPL model. This means that when two diagonal legs are attached with the climbing surface, the remaining legs are in an approximately free state, leading to the uncontrollable poses of the corresponding feet. In other words, the floating feet poses cannot reach the necessary conditions needed for the trot gait reuse when the GPL model is in the transitional state from one phase to the other one in one stride (S). In this paper, the conditions of GPL gait reuse are analyzed and the gait continuity is ensured by taking linear trajectory as an example.

Figures 2(a)–(c) describe the gait movement principle during half one gait. When $t = t_0$, the climbing robot is in the initial state, in which the diagonal legs with the black dot on the foot are attached with the climbing surface and the diagonal legs with the blank dot on the foot are swinging; see Figure 2(a). Namely, the left front leg and the right rear leg begin to establish attachment with the climbing surface. Then, the left leg contracts and the right leg extends, pulling the body upward. When $t = t_{m-}$, the climbing robot is in the transitional state; see Figure 2(b). It is obvious that the position of waist P moves from x_p to x_{pT} , and the distance in vertical direction is just half a stride. When $t = t_{m+}$, the other diagonal mechanism indicated by red dotted lines starts to execute the active movement, as shown in Figure 2(c). Now, the current state becomes the initial state of the next half one gait. In the same way, the right front leg and the left rear leg begin to establish attachment with the climbing surface and execute a similar movement. So, the state transition is realized from the former half one gait to the next one. Of course, the following conditions need to be satisfied.

Set the initial time $t = t_0$ and the terminal time $t = t_m$ during half a gait. Let x_p and x_{pT} , $L_i(t_0)$ and $L_i(tm)$, and θ_i and θ_{iT} ($i = 1 - 4$) be the position of the waist, length of linear legs, and angle between leg and the corresponding vertical line in the initial and transitional states of gait, respectively. Let γ_j ($j = 1, 2$) be the angle between line

PQ_j and PQ_{j+2} , keeping a constant value. Let S be the vertical stride of one gait.

To realize the gait continuity, the following constraints need to be satisfied when the following phase repeats the trajectory of the previous phase in one stride.

(a) Structure parameter constraints

It is mainly considered that the prototype design should keep bilateral symmetry. Thus,

$$\alpha_j = \alpha_{j+2},$$

$$d_j = d_{j+2} \quad (j = 1, 2). \quad (7)$$

(b) Leg pose constraints

These constraints include two aspects: feet angle and leg length. Here, the leg lengths can be actively controlled by motors.

$$\theta_j = \theta_{(j+2)T},$$

$$L_j(t_0) = L_{(j+2)}(t_m) \quad (j = 1, 2). \quad (8)$$

(c) Waist position constraints about central symmetry

This is determined by the trot gait adopted by the GPL model. Thus,

$$x_p + x_{pT} = -\frac{L_a}{2}. \quad (9)$$

Based on the geometric constraints, there exists a fixed relationship as follows:

$$\theta_j + \alpha_j + \theta_{j+2} + \alpha_{j+2} = \gamma_j,$$

$$\theta_{jT} + \alpha_j + \theta_{(j+2)T} + \alpha_{(j+2)T} = \gamma_j \quad (j = 1, 2). \quad (10)$$

According to (1), (7), (8), (9), and (10), the conditions of gait reuse and continuity for the GPL model can be obtained as follows.

$$x_p = f_1(\theta_1, \theta_2),$$

$$x_{pT} = f_1(\theta_{1T}, \theta_{2T}), \quad (11)$$

$$f_1(\theta_{1T}, \theta_{2T}) + f_1(\theta_1, \theta_2) = -\frac{L_a}{2},$$

where

$$\theta_{jT} = 2\beta_j - \theta_j. \quad (12)$$

From the above, it can be seen that the position of the waist has specific limitations to realize the gait continuity during the climbing process, rather than any position.

3. Trajectory Planning of GPL

3.1. Singularity and Feasible Region of the Waist. For the trajectory planning, singularity and workspace are both inevitable problems. Let $|J|$ denote the determinant of the Jacobian matrix J of the GPL model. When $|J| \rightarrow \infty$ is satisfied, the singularity of the GPL model occurs.

$$|J| \rightarrow \infty \Leftrightarrow L_b \times P_x + L_a \times P_y = 0. \quad (13)$$

Obviously, the singularity of the robot will occur when the position of the waist is located on the diagonal anomaly line from (13). In this case, the driving forces on each supporting foot will be infinite theoretically. In order to address this issue, the waist trajectory should avoid intersection with the diagonal anomaly line. According to (5) and (6), it suggests that the farther the waist trail keeps away from the diagonal line linking the supporting feet, the smaller the maximum force on the axial legs. This rule should be considered during trajectory planning of the waist for the robot.

As we know, trajectory planning must be restricted to the corresponding workspace. Here, the waist x_p is selected as the reference point for trajectory planning. The feasible region of the waist can be obtained according to previous analysis. Let $W \in \mathbb{R}^2$ denote the feasible region of the waist. Let $P_{x \min}$ and $P_{x \max}$ be the minimum and maximal values of P_x for a certain P_y within the feasible region of the waist, respectively.

From (1), the relation between P_x and P_y can be derived as follows:

$$P_x = -d_2 \sin \alpha_2 \sec \theta_2 - P_y \tan \theta_2. \quad (14)$$

Given a large range $[P_{y \min}, P_{y \max}]$ of P_y beyond the feasible region, $P_{x \min}$ and $P_{x \max}$ can be confirmed by the below constraints.

$$\begin{aligned} \text{Minimize} \rightarrow & \begin{cases} P_{x \min} = \min\{P_x\}, \\ P_{x \max} = \min\{-P_x\}, \end{cases} \\ \text{subject to} & \begin{cases} L_{j \min} \leq L_j \leq L_{j \max} \quad (j = 1, 2), \\ P_y = L_2 \cos \theta_2 + d_2 \cos(\theta_2 + \alpha_2), \\ P_{y \min} \leq P_y \leq P_{y \max}. \end{cases} \end{aligned} \quad (15)$$

Based on (1) and (15), a series of points including $(P_{x \min}, P_y)$ and $(P_{x \max}, P_y)$ constitute the boundary of W during half a gait. In the same way, the feasible region of the waist during the following half a gait can be determined, which is symmetric with the previous feasible region about the central axis and has a translational distance in the climbing direction.

3.2. Effect of Structural Parameters. As mentioned above, the feasible region of the waist directly affects trajectory planning of the climbing robot. Both driving forces of active legs and the feasible region of the waist are related to the structural parameters of the robot, including body length ratio, driving angle, and waist spring coefficient. Therefore, the structural parameters should be reasonably selected, which contributes

to a decrease in energy consumption and improvement in the stability of the climbing robot.

3.2.1. The Effect of Body Length Ratio on Supporting Forces of Climbing Robot. To avoid the disturbance of unreasonable motion path to structural parameters, it is necessary to plan a smooth motion trail of the waist to highlight the effect of structural parameters on the climbing performance of the robot. In terms of control weaknesses of the single curve function, an acceleration function composed by piecewise continuous function is adopted, which combines advantages of trapezoidal function and sine function. In this case, the acceleration curve function transits smoothly. Thus, the inertia force of the system could be reduced, which effectively improves the climbing speed and stability.

Let T be the working time during half a gait. Here, let L_{Ij} and L_{Tj} ($j = 1, 2$) be the initial and terminal lengths of legs L_j , respectively. According to kinematic analysis of the robot, L_{Ij} and L_{Tj} can be solved based on the start and terminal points (x_p and x_{pT}) of waist trajectory at initial and terminal times.

To ensure the smooth path and no impact velocity of the GPL model, the following boundary conditions are listed. Namely, the corresponding velocity and acceleration of legs L_j are both equal to zero at initial and terminal times.

$$\begin{aligned} L_j(t_0) &= L_{Ij}, \\ \dot{L}_j(t_0) &= 0, \\ \ddot{L}_j(t_0) &= 0, \\ L_j(t_m) &= L_{Tj}, \\ \dot{L}_j(t_m) &= 0, \\ \ddot{L}_j(t_m) &= 0. \end{aligned} \quad (16)$$

Define the trajectory interpolation functions $s(\tau)$, and let $s(\tau)$ be the independent variable. Thus,

$$\begin{aligned} L_j(t) &= L_{Ij} + (L_{Tj} - L_{Ij})s(\tau), \\ \dot{L}_j(t) &= (L_{Tj} - L_{Ij})\dot{s}\frac{\tau}{T}, \\ \ddot{L}_j(t) &= (L_{Tj} - L_{Ij})\ddot{s}\frac{\tau}{T^2}, \end{aligned} \quad (17)$$

where $s(\tau)$ meets the following constraints:

$$\begin{aligned} 0 &\leq s(\tau) \leq 1, \\ 0 &\leq \tau \leq 1, \\ \tau &= \frac{t - t_0}{T}, \\ T &= t_m - t_0. \end{aligned} \quad (18)$$

Give priority to acceleration, and set $\ddot{s}(\tau)$ as follows:

$$\ddot{s}(\tau) = \begin{cases} k \sin(4\pi\tau), & 0 \leq \tau \leq \frac{1}{8} \\ k, & \frac{1}{8} \leq \tau \leq \frac{3}{8} \\ k \sin(4\pi\tau - \pi), & \frac{3}{8} \leq \tau \leq \frac{5}{8} \\ -k, & \frac{5}{8} \leq \tau \leq \frac{7}{8} \\ k \sin(4\pi\tau - 3\pi), & \frac{7}{8} \leq \tau \leq 1. \end{cases} \quad (19)$$

Integrating (19) with respect to time and combining the initial and terminal conditions, the value of k can be determined as follows:

$$\begin{aligned} s(\tau) &= \int_{t_0}^{t_m} \int_0^1 \ddot{s}(\tau) d\tau, \\ s(0) &= 0, \\ s(1) &= 1. \end{aligned} \quad (20)$$

According to (16), (17), (19), and (20) and structural parameters of the climbing robot (Table 1), the planned trajectory of the waist can be obtained. Combining the kinematic analysis of robot, the whole controlling function of legs can be confirmed.

To study the effect of the length ratio of front and rear body on driving forces of the robot, the different body length ratios $\lambda = 8/2$, $\lambda = 6/4$, $\lambda = 5/5$, and $\lambda = 4/6$ are set to calculate the driving forces according to the planned trajectory of waist and kinematic analysis. According to Figure 3, the supporting forces on front and rear feet present a significant decreasing trend as the increasing body length ratio. It is worth mentioning that the supporting forces on rear foot display a smaller negative value with the larger body length ratio, which contributes to a reduction in negative work of the robot. It suggests that the waist close to the bottom of the lower body can effectively optimize driving forces and system energy consumption.

3.2.2. The Effect of Driving Angle on Start and Terminal Points of Waist Trajectory. According to bionic research [22, 23], the driving angle β of reptile gecko usually keeps a certain value. From (11), it can be shown that β has an obvious influence on the start and termination point space of the waist. To explore the effect of the driving angle on the start and terminal points of the waist, the driving angle range [8, 11] is selected to compute the start and termination point space and the feasible region of the waist based on the following dimension constraints and structural parameters (Table 1).

$$\begin{bmatrix} L_{1\min} \\ L_{2\min} \end{bmatrix} \leq \begin{bmatrix} L_1(t) \\ L_2(t) \end{bmatrix} \leq \begin{bmatrix} L_{1\max} \\ L_{2\max} \end{bmatrix}. \quad (21)$$

From Figure 4, the range of the waist feasible region shows a slightly increasing trend with driving angle β . As mentioned above, trajectory planning should avoid the singular line due to waist joint on singular position, causing

TABLE 1: Structural parameters of the climbing robot.

Parameters	L_a (mm)	d_1 (mm)	$L_{1\min}$ (mm)	$L_{1\max}$ (mm)
Value	230	168	103	168
m_1 (g)	L_b (mm)	d_2 (mm)	$L_{2\min}$ (mm)	$L_{2\max}$ (mm)
243	420	113	85	150
m_2 (g)	N_G	η (%)	R_a (Ω)	K_M (Nm/A)
223	2	77	4	10.2

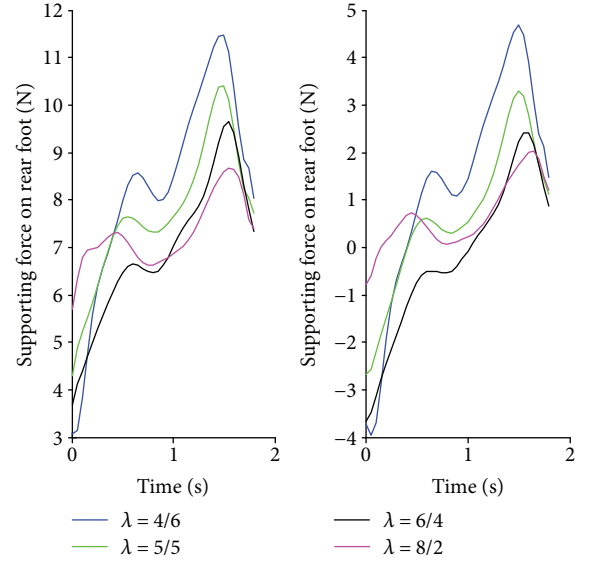


FIGURE 3: Supporting forces of the GPL model with different body length ratios.

infinite force. Therefore, the start and termination points of the waist joint should be at the same side of the singular line. In addition, the motion trajectory must be within the waist feasible region in terms of structural constraint. Namely, the start and termination points of the waist also need to be located in the feasible region. Here, the optimal driving angle is 9° .

3.2.3. The Effect of Waist Spring Coefficient on Supporting Forces of Climbing Robot. As we know, the reverse driving forces produce negative work, increasing system energy consumption. The driving forces are associated with the waist spring coefficient according to (3) and (5). Hence, the waist spring coefficient of the robot is analyzed to obtain a reasonable value, which contributes to a decrease in negative driving forces.

To optimize the energy consumption, we need to reduce thermal energy during robot climbing. It means that the negative work done by the supporting legs should be avoided. For a given waist trajectory or a climbing dynamic gait, the negative work will be as small as possible when the following (22) is satisfied. According to the equation, we can obtain the range of k_w (0.503–0.616) to ensure the positive driving forces.

$$\begin{aligned} F_1 &> 0, \\ F_2 &> 0. \end{aligned} \quad (22)$$

Given the range of k_w ($0 - 1 \text{ N} \cdot \text{mm}$), the system energy consumption is calculated based on the above planning trajectory of the waist as well as (5) and (6). Figure 5(a) shows that the supporting forces on front and rear feet decrease and increase with k_w , respectively. There exist the largest negative and positive driving forces in the case of $k_w = 1 \text{ N} \cdot \text{mm}$ than the ones in other cases. From Figure 5(b), it can be seen that the lesser negative forces active legs produce, the lesser the system energy consumption and the better the movement performance of the robot. Here, the reasonable spring coefficient can improve athletic performance while an oversize value of the spring coefficient may generate a negative effect on climbing motion of the robot. We can also find that the system energy consumption can obtain the smallest value when $k_w = 0.5 \text{ N} \cdot \text{mm}$. This is in accord with the above analysis based on (22). Hence, the value of $k_w = 0.5 \text{ N} \cdot \text{mm}$ is selected in this paper.

3.3. Trajectory Optimization Based on Energy Consumption. During practical applications, there are high requirements of energy supply to be put forward for the robot system. Generally, the load-bearing capability of multilegged climbing robots is limited, which cannot carry greater weight energy storage units. Thus, it is significant to reasonably control mechanical energy consumption and improve climbing efficiency of the robot during the design process of the climbing robot. In this section, we focus on trajectory optimization based on system energy consumption.

Here, the waist joint coordinates can be expressed by the m -rank polynomial through the Hermite interpolation method, as follows:

$$\begin{aligned} x_p(t) &= a_{j0} + a_{j1}(t - t_0) + \cdots + a_{jm}(t - t_0)^m, \quad j = 1, \\ y_p(t) &= a_{j0} + a_{j1}(t - t_0) + \cdots + a_{jm}(t - t_0)^m, \quad j = 2. \end{aligned} \quad (23)$$

The above equation can be written in matrix form, as follows:

$$q(A, t) = \begin{bmatrix} x_p(t) \\ y_p(t) \end{bmatrix} = Ah(t), \quad (24)$$

where A is the multinomial coefficient matrix, which needs to be calculated.

$$\begin{aligned} A &= \begin{bmatrix} a_{10} & \cdots & a_{1m} \\ a_{20} & \cdots & a_{2m} \end{bmatrix} \in \mathbb{R}^{2 \times (m+1)}, \\ h(t) &= [1 \quad (t - t_0) \quad \cdots \quad (t - t_0)^m]^T. \end{aligned} \quad (25)$$

As in Section 3.2, the driving angle and body length ratio have been discussed and the optimal values have been obtained. The driving force curves of supporting feet at every start and termination points of the waist joint can be accomplished according to (1), (2), and (13). Considering the minimum driving force as the optimization goal, the best start point $q(A, t_0)$ and termination point $q(A, tm)$ of the waist

joint are selected. To ensure the smooth motion track of the robot, it is necessary to guarantee the angular velocity and angular acceleration to be continuous. Therefore, the following constraint equations need to be satisfied:

$$\begin{aligned} q(A, t_k) &= \begin{bmatrix} x_p(t_k) \\ y_p(t_k) \end{bmatrix} = \begin{bmatrix} x_{1k} \\ x_{2k} \end{bmatrix} = Ah(t_k), \\ \dot{q}(A, t_k) &= \begin{bmatrix} \dot{x}_p(t_k) \\ \dot{y}_p(t_k) \end{bmatrix} = \begin{bmatrix} x_{1(k+1)} \\ x_{2(k+1)} \end{bmatrix} = A\dot{h}(t_k), \\ \ddot{q}(A, t_k) &= \begin{bmatrix} \ddot{x}_p(t_k) \\ \ddot{y}_p(t_k) \end{bmatrix} = \begin{bmatrix} x_{1(k+2)} \\ x_{2(k+2)} \end{bmatrix} = A\ddot{h}(t_k) \quad (k = 0, m), \end{aligned} \quad (26)$$

where x_{ij} is the boundary condition, which denotes the position, velocity, and acceleration of the waist at the start and terminal points.

Combining the above equation constraints, the boundary conditions can be obtained as follows:

$$\text{Ce}q_j(A) = 0, \quad j = 1 - 6. \quad (27)$$

In addition, the waist joint coordinates are limited to the dimension constraint relation as in (15). Thus, there are four inequality constraints as follows:

$$C_i(A) \leq 0, \quad i = 1 - 4. \quad (28)$$

In terms of constraint condition for waist joint coordinate x or y , there are six equation constraints. And there are twelve equations and four inequalities for the waist joint coordinate in x and y directions. Therefore, at least seven undetermined coefficients are needed to solve the solution. Here, $m = 6$.

According to the above theoretical analysis, the system energy consumption is mainly caused by active joints. So, the power consumption of the robot at any time can be represented by multinomial coefficient matrices A and $h(t)$.

$$P(A, t) = \sum_{j=1}^2 P_j(t) = \widehat{D}\ddot{q}(A, t) + \widehat{H}\dot{q}(A, t) + \widehat{S}q(A, t) + \widehat{C}. \quad (29)$$

The optimization problem of system energy consumption can be described as

$$\begin{aligned} \text{Minimize} & \rightarrow \int_{t_0}^{t_m} P(A, t) dt, \\ \text{subject to} & \begin{cases} \text{Ce}q_j(A) = 0, \\ C_i(A) \leq 0. \end{cases} \end{aligned} \quad (30)$$

So the trajectory optimization of the waist can be transformed into a nonlinear programming problem in the nonlinear equality and inequality constraints. According to the structural parameters and gait conditions, the multinomial

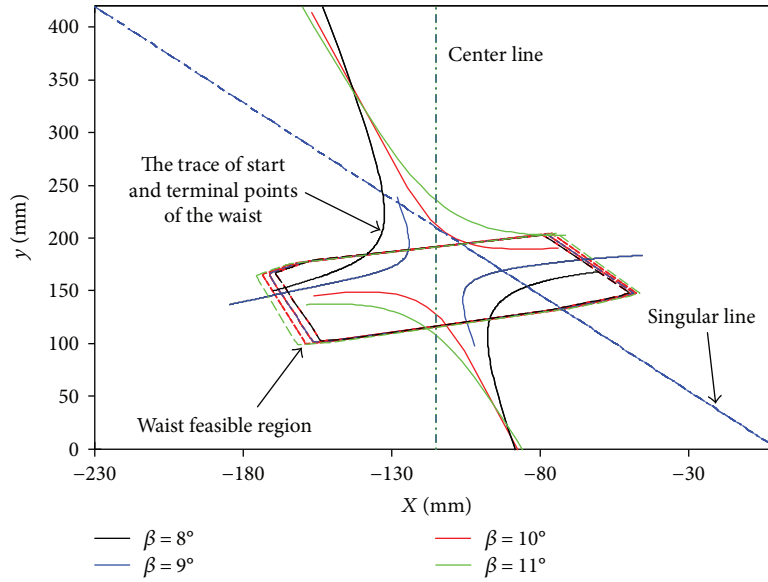


FIGURE 4: The start and termination point space and the feasible region of the waist.

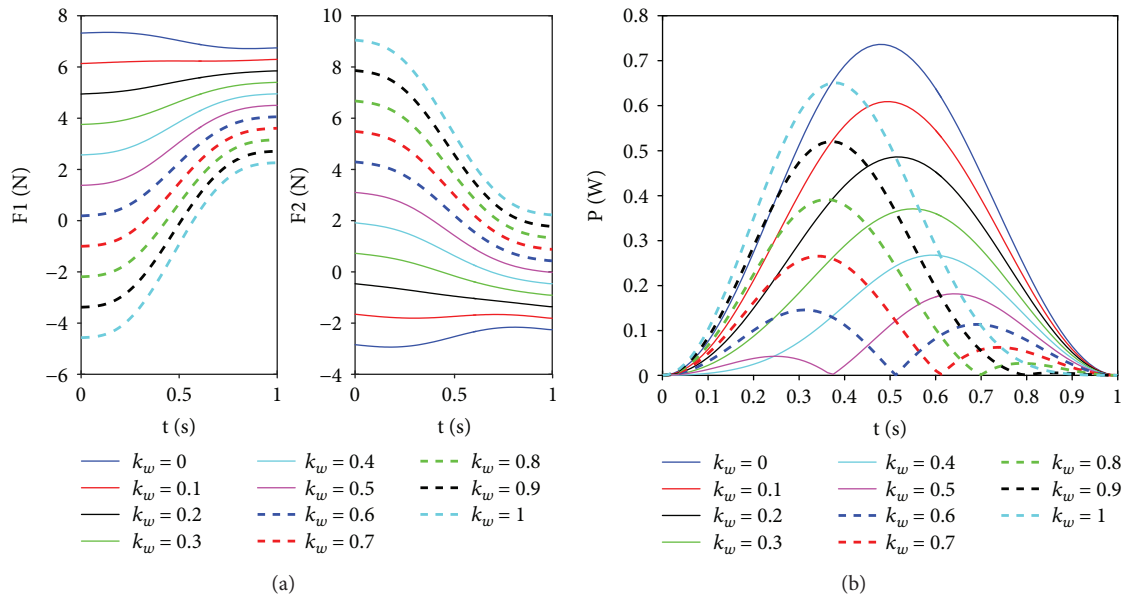


FIGURE 5: The effect of the waist spring coefficient. (a) The supporting forces on front and rear feet with different waist spring coefficients. (b) The system energy consumption with different waist spring coefficients.

coefficient matrices A can be solved and the optimal trajectory of the waist can be obtained, as shown in Figure 6.

4. Experiments and Results

4.1. Prototype Design Based on the GPL Model. The robot based on the GPL model is composed of two rigid parts and four identical leg modules. According to Figure 7(a), there is no difference between mechanical configurations of the upper and lower parts in addition to the size parameter. And both parts connect to each other by the passive waist, which is a rotational joint in practice. Here, the position of the waist joint can be adjusted along the central axis of the

upper part. The linear leg modules fixed on the rigid parts are adopted to realize the desired motion of the climbing robot, and they keep a certain angle with the body axis. In order to facilitate parameter adjustment, the angle and position of the rotating joint can be regulated manually. From Figure 7(b), the linear leg module consists of spines, buffer units, a linear guide with a rack, and a linear slider fixed on the rigid part. Here, the spine is fixed on the cylindrical slider that can slide in a linear track. The track named as spring shells is divided into two segmentations by a cylindrical slider, which plays a buffer role in two directions. To acquire the accurate motion of the robot, the linear leg modules are directly driven by a rotary motor with a rack and pinion

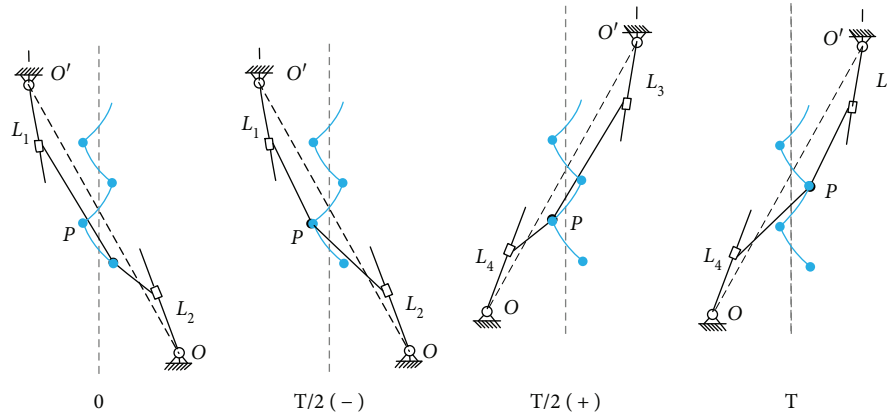


FIGURE 6: The optimal trajectory of waist during the whole gait. Here, the blue line and blue circle dot denote the optimal trajectory and the start and terminal points during the half gait, respectively.

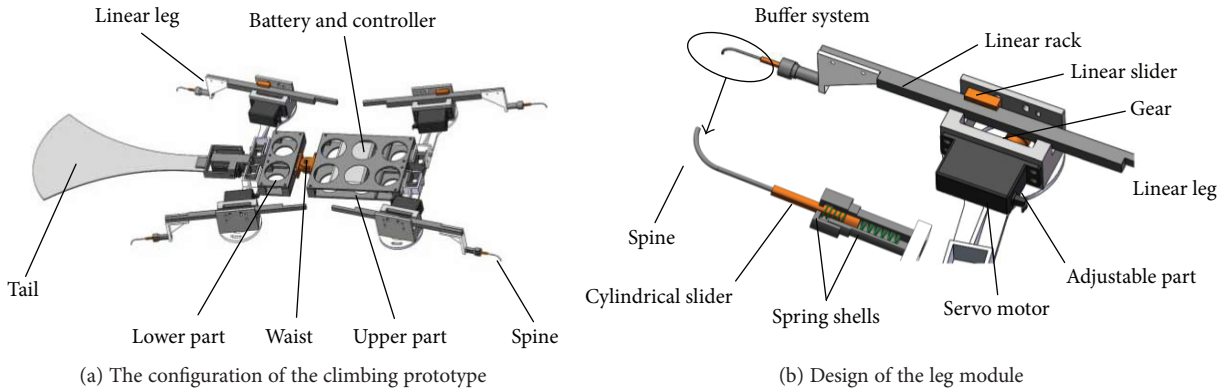


FIGURE 7: Prototype design based on the GPL model.

mechanism. The corresponding linear speed of linear legs can be regulated and controlled by servo motors.

In view of the overturning torque in the whole climbing process, it is necessary to reduce the torque to avoid drop damage. As we know, the overturning torque becomes larger as the thickness of the robot increases. So, the thickness of the robot is limited to 14.8 mm and the motor is placed on the rigid parts. Moreover, a thin flat tail acting as a support is designed to obtain a more stable climbing movement. In fact, the tail is ignored in dynamics of the GPL model due to its micro weight. In addition, the controller and battery are located in the upper part, which have the effect of counter weight by adjusting their corresponding position.

4.2. Actual Climbing Experiments and Force Measurement on Supporting Feet. In order to verify the designed gait and condition of gait reuse, the test platform with linen is established and the actual climbing experiment is conducted. According to Figure 8(a), the robot adopts a symmetrical gait and moves smoothly during a whole gait circle, which shows an intuitive understanding about gait reuse and continuity. It suggests that the theoretical analysis is validated and it provides the basis for the trajectory planning of the robot. It should be noted that the climbing speed is 66 mm/s in the dynamic analysis for robot climbing. Actually, the

speed of the prototype is limited by failure of the spine's attachment/detachment to the cloth-covered climbing surface in the climbing experiment, which will be improved. Therefore, the speed of the prototype is reduced to 50 mm/s to maintain a more stable climbing in the test. Meanwhile, the force-measuring platform is built to explore the effect of structural parameters on supporting forces of the robot, as shown in Figure 8(b).

In the supporting force measurement experiment, the planning trajectory of the waist in Section 3.2.1 is applied. And the ranges of the waist spring coefficient and body length ratio are in accord with the above analysis. From Figure 9, we can obviously find that the supporting forces on front and rear feet have the same decreasing trend with the increase in λ . Meanwhile, the ranges of supporting forces vary greatly with λ under a given waist spring coefficient k_w . This indicates that the larger body length ratio contributes to a decrease in the driving forces, which is consistent with theoretical analysis. Based on (6), the system energy consumption is directly related to the supporting forces, which is expected to be as small as possible. Moreover, the waist spring coefficient has a significant effect on supporting forces, especially forces on rear feet. From Figures 9(a) and 9(b), there exist negative values on the rear-supporting foot when k_w is 0 N·mm and 0.2 N·mm.

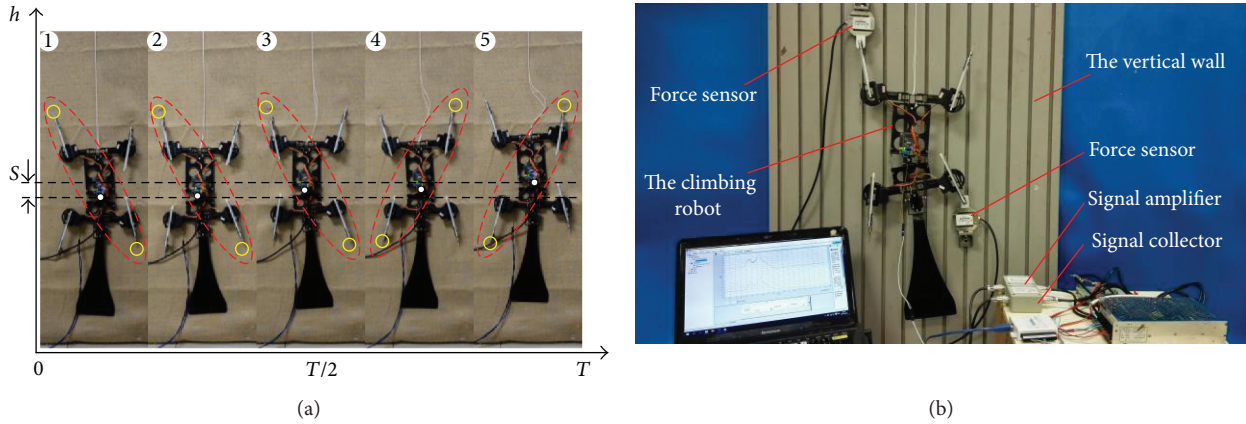


FIGURE 8: Actual climbing experiments on cloth-covered climbing surface and force measurement on supporting feet. (a) The sequence of climbing gait. Here, the red dotted line indicates the current adherent mechanism and the yellow circles indicate the adherent feet. (b) The test facilities of climbing robot and supporting force experiment.

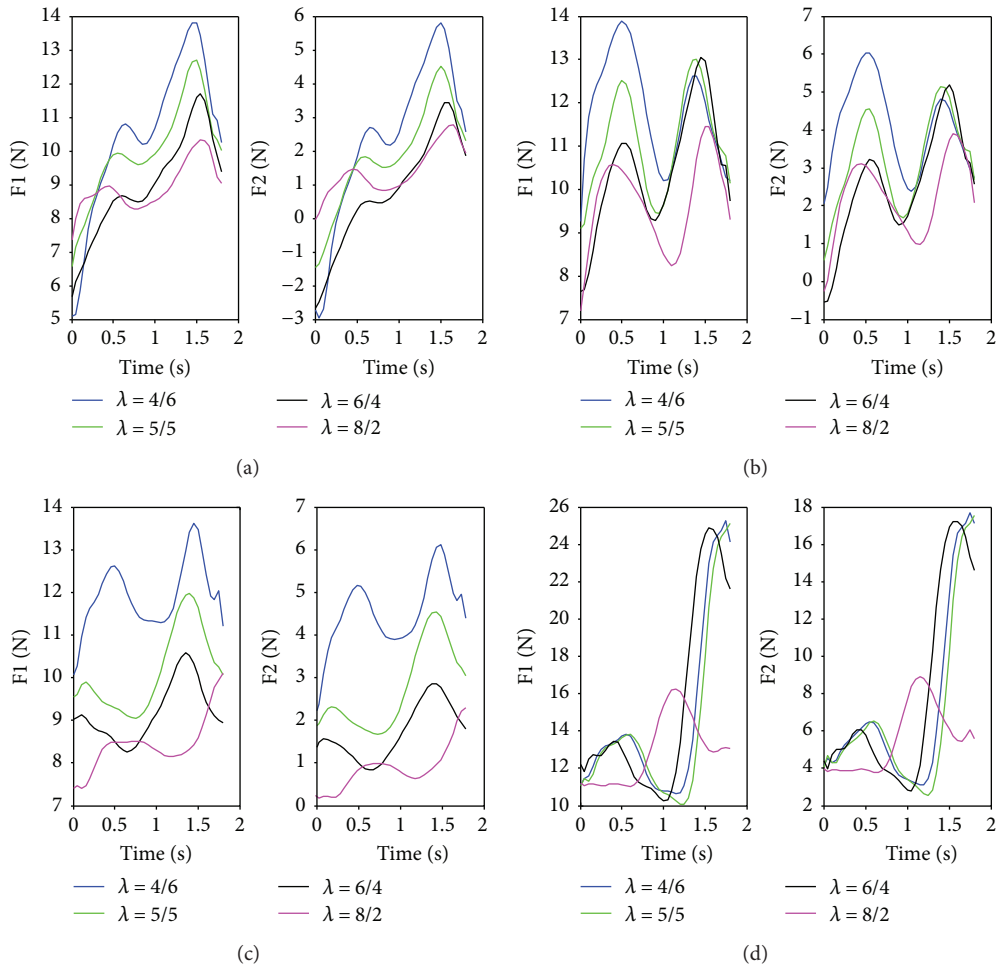


FIGURE 9: The supporting forces on front and rear feet with different waist spring coefficients and body length ratios: (a) $k_w = 0 \text{ N} \cdot \text{mm}$; (b) $k_w = 0.2 \text{ N} \cdot \text{mm}$; (c) $k_w = 0.5 \text{ N} \cdot \text{mm}$; (d) $k_w = 1 \text{ N} \cdot \text{mm}$.

According to Figures 9(c) and 9(d), the negative forces decrease gradually with the increase in k_w while the overall values of supporting forces become larger. Based on previous

analysis, the negative forces on the rear-supporting foot should be avoided to reduce energy consumption in the process of climbing. In addition, there exist obvious fluctuations

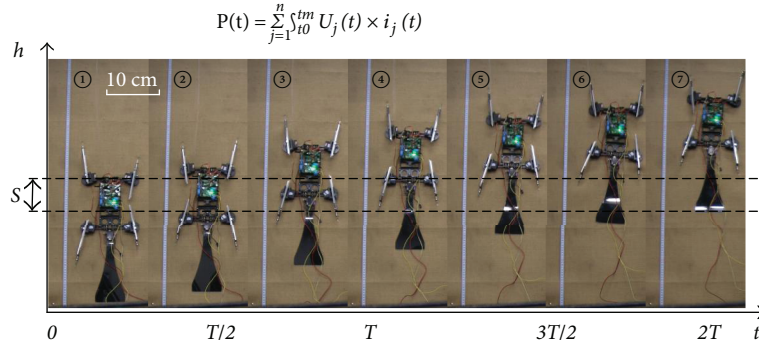


FIGURE 10: Energy consumption experiments of the climbing robot.

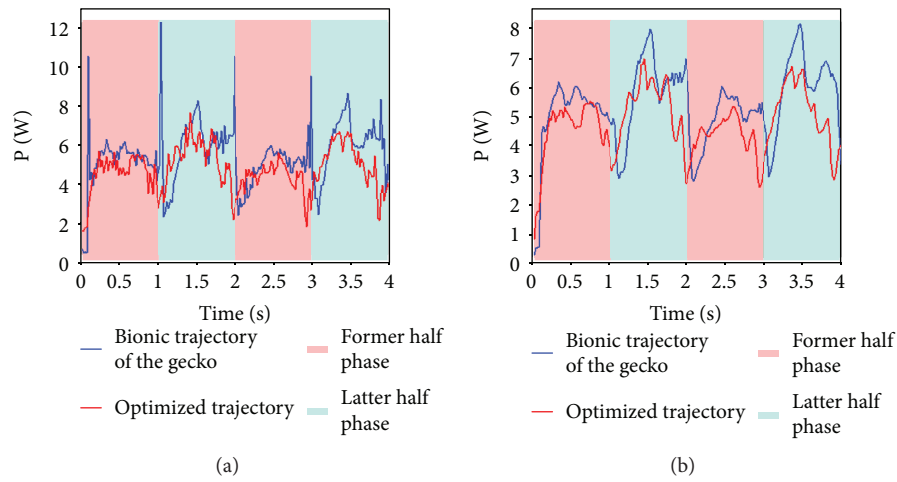


FIGURE 11: Energy consumption of the climbing robot with different trajectories. (a) The total input power of the robot with unfiltering data; (b) the total input power of robot with filtering data.

of supporting forces in Figures 9(a), 9(b), and 9(d). This means that the stability and structural strength of the climbing robot are easily damaged from the changing stresses to the actuators and manipulator structure. Therefore, 0.5 N·mm may be a more reasonable value of k_w in view of the whole positive amounts and smaller range of supporting forces on both feet.

4.3. Energy Consumption Experiments. To verify the effectiveness of the optimized trajectory in Section 3.3, the energy consumption experiments are carried out, as shown in Figure 10. According to bionic research on gecko, the sinusoidal curve fitting the trajectory of the gecko's waist is applied to contrast with optimized trajectory [24, 26]. And the current sensors are adopted to obtain the instantaneous current values of motors. The instantaneous input power of the motor is the product of the instantaneous armature current and the instantaneous armature voltage. Thus, the total input power of the robot can be obtained as follows. Here, $U_j(t)$ is a constant 5 V.

$$P(t) = \sum_{j=1}^n \int_{t_0}^{t_m} U_j(t) \times i_j(t). \quad (31)$$

According to Figure 11, the power based on optimized trajectory is less than that based on bionic trajectory of the gecko. The former is 7.39 W and the latter is 9.79 W, in which the energy consumption based on optimized trajectory saves 24.5% than the latter one does. Obviously, it suggests that the optimized trajectory is effective, enhancing the theoretical analysis in this paper. Moreover, the results in our experiments may partly explain the reasonability of the quadruped reptile's kinesiology during dynamic gait.

5. Conclusion and Future Work

Benefitting from dynamic gait, the GPL model inspired by gecko has been proposed in our previous work. In order to further develop dynamic gait and reduce energy consumption of the climbing robot based on the GPL model, the gait design and trajectory planning are analyzed in this paper. In view of the special construction of the GPL model, the trot gait is adopted and the conditions of gait reuse are presented. According to the kinematics and dynamics of the GPL model, the structural parameters have a significant effect on the trajectory planning of the robot. The prototype experiment results show that the larger body length ratio and a certain elasticity of the waist joint contribute to a decrease in the

supporting forces and reduction in system energy consumption, especially negative forces on supporting feet. Moreover, it suggests that the driving angle plays an important role on obtaining a reasonable performance of gait continuity. From the perspective of gecko, the pendular waist with certain elasticity is beneficial to storing kinetic energy in fluctuation and reducing energy consumption in the process of climbing. Therefore, the optimal trajectory of the waist is planned based on system energy consumption. The energy consumption experiments about optimal trajectory and gecko's sinusoidal curve are conducted, where a similar trend and less value of power suggest that the optimized trajectory is effective. Further, the results in our experiments partly explain the reasonability of the quadruped reptile's kinesiology during dynamic gait.

In the future work, the deformation of the structure will be considered in dynamics of the GPL model. And the flexible material and foot structure with multiple degrees of freedom will be included in the future design of climbing robots.

Conflicts of Interest

The authors declare that there is no conflict of interest regarding the publication of this manuscript.

Acknowledgments

This study is supported by the National Natural Science Foundation of China (no. 51475018), Beijing Natural Science Foundation (no. 3162018), and Innovation Practice Foundation of BUAA for Graduates (no. YCSJ-01-201709).

References

- [1] A. O. Pullin, N. J. Kohut, D. Zarrouk, and R. S. Fearing, "Dynamic turning of 13 cm robot comparing tail and differential drive," in *2012 IEEE International Conference on Robotics and Automation*, vol. 20no. 10, pp. 5086–5093, St. Paul, MN, USA, 2012.
- [2] W. Wang, K. Wang, and H. Zhang, "Crawling gait realization of the mini-modular climbing caterpillar robot," *Progress in Natural Science*, vol. 19, no. 12, pp. 1821–1829, 2009.
- [3] A. M. Hoover, S. Burden, X. Y. Fu, and S. S. Sastry, "Bio-inspired design and dynamic maneuverability of a minimally actuated six-legged robot," in *2010 3rd IEEE RAS & EMBS International Conference on Biomedical Robotics and Biomechatronics*, vol. 28no. 1, pp. 869–876, Tokyo, Japan, 2010.
- [4] G. A. Lynch, L. Rome, and D. E. Koditschek, "Sprawl angle in simplified models of vertical climbing: implications for robots and roaches," *Applied Bionics and Biomechanics*, vol. 8, no. 3-4, 452 pages, 2011.
- [5] P. Birkmeyer, A. G. Gillies, and R. S. Fearing, "Dynamic climbing of near-vertical smooth surfaces," in *2012 IEEE/RSJ International Conference on Intelligent Robots and Systems*, vol. 57no. 1, pp. 286–292, Vilamoura, Algarve, Portugal, 2012.
- [6] M. P. Murphy, C. Kute, Y. Mengüç, and M. Sitti, "Waalbot II: adhesion recovery and improved performance of a climbing robot using fibrillar adhesives," *The International Journal of Robotics Research*, vol. 30, no. 1, pp. 118–133, 2011.
- [7] G. C. Haynes and A. A. Rizzi, "Gait regulation and feedback on a robotic climbing hexapod," in *Proceedings of Robotics: Science & Systems II*, pp. 97–104, Philadelphia, PA, USA, 2006.
- [8] M. J. Spenko, G. C. Haynes, J. A. Saunders et al., "Biologically inspired climbing with a hexapedal robot," *Journal of Field Robotics*, vol. 25, no. 4-5, pp. 223–242, 2008.
- [9] S. Kim, M. Spenko, S. Trujillo, B. Heyneman, D. Santos, and M. R. Cutkosky, "Smooth vertical surface climbing with directional adhesion," *IEEE Transactions on Robotics*, vol. 24, no. 1, pp. 65–74, 2008.
- [10] A. Sintov, T. Avramovich, and A. Shapiro, "Design and motion planning of an autonomous climbing robot with claws," *Robotics and Autonomous Systems*, vol. 59, no. 11, pp. 1008–1019, 2011.
- [11] R. Blickhan, "The spring-mass model for running and hopping," *Journal of Biomechanics*, vol. 22, no. 11-12, pp. 1217–1227, 1989.
- [12] J. Schmitt, M. Garcia, R. C. Razo, P. Holmes, and R. J. Full, "Dynamics and stability of legged locomotion in the horizontal plane: a test case using insects," *Biological Cybernetics*, vol. 86, no. 5, pp. 343–353, 2002.
- [13] J. D. Dickson and J. E. Clark, "Design of a multimodal climbing and gliding robotic platform," *IEEE/ASME Transactions on Mechatronics*, vol. 18, no. 2, pp. 494–505, 2013.
- [14] G. A. Lynch, J. E. Clark, P. C. Lin, and D. E. Koditschek, "A bioinspired dynamical vertical climbing robot," *International Journal of Robotics Research*, vol. 31, no. 8, pp. 974–996, 2012.
- [15] W. R. Provancher, S. I. Jensen-Segal, and M. A. Fehlgberg, "ROCR: an energy-efficient dynamic wall-climbing robot," *IEEE/ASME Transactions on Mechatronics*, vol. 16, no. 5, pp. 897–906, 2011.
- [16] Z. Y. Wang, Z. D. Dai, Z. W. Yu, and D. N. Shen, "Optimal attaching and detaching trajectory for bio-inspired climbing robot using dry adhesive," in *Proceedings of the IEEE/ASME International Conference on Advanced Intelligent Mechatronics*, pp. 990–993, Besanson, France, 2014.
- [17] S. C. Chen, K. J. Huang, W. H. Chen, S. Y. Shen, C. H. Li, and P. C. Lin, "Quattroped: a leg-wheel transformable robot," *IEEE/ASME Transactions on Mechatronics*, vol. 19, no. 2, pp. 730–742, 2014.
- [18] T. Akinfiyev and M. Armada, "The influence of gravity on trajectory planning for climbing robots with non-rigid legs," *Journal of Intelligent and Robotic Systems*, vol. 35, no. 3, pp. 309–326, 2002.
- [19] S. L. Wu, W. Wang, D. Wu, C. Chen, P. H. Zhu, and R. Liu, "Analysis on GPL's dynamic gait for a gecko inspired climbing robot with a passive waist joint," in *Proceedings of the IEEE International Conference on Robotics and Biomimetics*, pp. 943–948, Bali, Indonesia, 2015.
- [20] W. Wang, S. L. Wu, P. H. Zhu, and R. Liu, "Analysis on the dynamic climbing forces of a gecko inspired climbing robot based on GPL model," in *Proceedings of the IEEE/RSJ International Conference on Intelligent Robots and Systems*, pp. 3314–3319, Hamburg, Germany, 2015.
- [21] K. Autumn, S. T. Hsieh, D. M. Dudek, J. Chen, C. Chitaphan, and R. J. Full, "Dynamics of geckos running vertically," *Journal of Experimental Biology*, vol. 209, no. 2, pp. 260–272, 2006.
- [22] Z. Wang, G. Sun, and Z. Dai, "Trajectory optimization for robot crawling on ceiling using dry elastomer adhesive," in *Advances in Reconfigurable Mechanisms and Robots II*, pp. 593–601, Springer International Publishing, Cham, 2016.

- [23] Z. Y. Wang, X. B. Lu, Q. Liu, Y. Song, and Z. D. DAI, "Adhesion performance test and trajectory optimization for gecko-inspired footpad under simulated micro-gravity environment," *Chinese Science Bulletin*, vol. 62, no. 19, pp. 2149–2156, 2017.
- [24] Z. Wang, L. Cai, W. Li, A. Ji, W. Wang, and Z. Dai, "Effect of slope degree on the lateral bending in gekko geckos," *Journal of Bionic Engineering*, vol. 12, no. 2, pp. 238–249, 2015.
- [25] Z. D. Dai and A. H. Ji, *Biomechanical Base for Bioinspiration of Gecko Locomotion*, Harbin Institute of Technology Press, Harbin, China, 1st edition, 2011.
- [26] J. W. Cheng, *Research on characteristics of gecko's gait and posture*, [M.S. thesis], Nanjing University of Aeronautics and Astronautics, Nanjing, China, 2007.

Research Article

A Highly Reliable Embedded Optical Torque Sensor Based on Flexure Spring

Yuwang Liu ¹, Tian Tian,² Jibiao Chen ³, Fuhua Wang,¹ and Defu Zhang ³

¹State Key Laboratory of Robotics, Shenyang Institute of Automation, Chinese Academy of Sciences, Shenyang, China

²Department of Mechanical Engineering, Shenyang Ligong University, Shenyang, China

³Department of Mechanical Engineering, Northeastern University, Shenyang, China

Correspondence should be addressed to Yuwang Liu; liuyuwang@sia.cn

Received 23 October 2017; Revised 2 January 2018; Accepted 28 January 2018; Published 15 April 2018

Academic Editor: QingSong He

Copyright © 2018 Yuwang Liu et al. This is an open access article distributed under the Creative Commons Attribution License, which permits unrestricted use, distribution, and reproduction in any medium, provided the original work is properly cited.

We propose a new highly reliable and lightweight embedded optical torque sensor for biomimetic robot arm enabling the torque measurement in joints, which can measure torque of the joint by detecting torsion of its elastic element (mechanical structure or flexure element). Flexure spring is introduced as the elastic element of the torque sensor in this paper. Because of its curve modeling, flexure spring is not inclined to be broken contrast to crossbeam structure, which is commonly used in torque sensor. Thanks to this structure, we can build a torque sensor as an extremely compact and highly reliable size. Six types of flexure spring are proposed to be used as the elastic element of the torque sensor in this paper, which have the potential for the requirements of measurement range and multidimensional detection. The optical electronic, less influenced by electromagnetic interferences, is selected to measure the torsion displacement of the flexure spring. The proposed design is analyzed, which can obtain the successful measurement of the torque with a load capacity of 1 Nm. One of the designed optical torque sensors is optimized by FEM. The calibration and experiment are conducted to ensure its feasibility and performance.

1. Introduction

This paper focuses on the design of a new highly reliable and lightweight embedded optical torque sensor for biomimetic robots in order to ensure accuracy and stability while performing practical tasks of physical interaction with unstructured environment. Biomimetic robot arm is used to realize dexterous tasks such as interaction with human or manipulation with objects in hazardous conditions. To achieve the stability in contact with environment and realize safety while performing tasks of physical interaction with human and unstructured environment, it is essential to calculate the torque of each joint of the robot arm. The torque information of the torque sensor greatly enhances the force perception ability of biomimetic robot joint. The development of embedded torque sensor, especially, a lightweight and highly reliable one, has been of great interest for decades [1–3]. Based on its measurement methods, the torque sensor can be classified as strain gauges [4–6], capacitive [7–9], piezoelectric [10, 11], photoelectric [1, 12–17], and so on [18, 19].

Kang et al. [4] designed a mechanically decoupled six-axis force/torque sensor. It is a crossbeam sensor, which use strain gauge technique to detect force/moment. The size of this sensor is small with thickness of 37 mm, and the maximum torque detected by this sensor is 40 Nm. Also, Ma et al. [5] presented three kinds of compact torque sensors using strain gauge technique. The structure of these sensors is cartwheel flexure, which is also crossbeam. The measurement ranges of these sensors are 7 Nm, 22 Nm, and 50 Nm, respectively. The thickness is about 6 mm which is much suitable for using an embedded application. However, it is difficult to attach the strain gauge to the structure reliably while developing the type of torque sensor which is commonly sensitive to electrical noise and temperature. Kim et al. [7] designed a six-axis force/moment capacitive sensor using dielectric elastomer. Its deformation results in variation of capacitance, which is used for sensing force/moment. The size of this sensor is 67 mm × 30 mm, and the measurement range is 0.16 Nm. However, it is generally nonlinearity. Liu et al. [10] designed a no-elastic six-axis force/moment

sensor using piezoelectric. The maximum torque detected by this sensor is as high as 250 Nm when the size is small as 50 mm × 30 mm. However, piezoelectric sensor is generally too stiff for this condition.

Recently, lots of researchers have been interested in this type of optical for its compact size, noncontact approach, and less electromagnetic interference. Kim et al. [12] designed a three-axis force/moment optical sensor using crossbeam which has a thickness of 7 mm and a diameter of 28 mm making it the most compact. Also, Shams et al. [13] presented an optical crossbeam torque sensor. This sensor is compact with a thickness of 11 mm and a diameter of 80 mm. Tsetserukou et al. [14] proposed three types of optical torque sensors. The first one is the cross-shaped spring with a diameter and thickness of 30 mm which can be used to detect 1.75 Nm load. The second one is the hub spoke-shaped spring with a diameter of 42 mm and thickness of 6.5 mm, and the sensor can be used to measure torque up to 0.8 Nm. The third one is the ring-shaped spring with a diameter of 42 mm and thickness of 10 mm, which can be used to handle torque up to 0.8 Nm.

Relatively speaking, the optical torque sensors tend to acquire much more deformation which is very suitable to build a biomimetic robot. However, the proposed sensors are commonly close to the yield stress at the maximum of torque size in which the overload protection needs to be added to keep it operating. However, it is inconvenient to build a sensor with this mechanism as it will increase the joint size. Factor of safety is a property to evaluate the ability of resistance to overload. It suggests the property of reliability, which is equal to the yield stress divided by the allowed one. However, an ideal compact size of the structure with a high factor of safety especially for the embedded sensor is very hard to acquire. The fact is that the factor of safety of optical torque sensors is generally limited to 1.0~2.0 [1, 14, 15, 34].

Flexure spring, also called planer spring or torsion spring, has been used in many fields for its advantages of compact structure and highly reliable performance [20–25]. It has been used to design a strain gauge sensor [22, 23]. However, the application of flexure spring to torque sensor has not been developed yet. In addition, limited to the mount space, there is also a challenge to build an optical torque sensor based on the spring.

In this paper, we develop a highly reliable embedded optical torque sensor using flexure spring. The size of the torque sensor is designed to be extremely small, according to that of joint with the output of 1 Nm. The flexure spring, with the ability of storing energy and reducing the potential of stress concentration, is applied to realize the high reliability of torque sensor. In [33], we imitate an elephant's trunk with the special function of holding objects and propose a new type of shape-adaptive elephant's trunk robot to which the embedded optical torque sensor could be well applied. As shown in Figure 1, the elephant's trunk robot could be seen as a biomimetic elephant's trunk, whose effect could be equivalent to a kind of large artificial muscle. The robot consists of a base and some under-actuated joint units; the size of which is very similar to the real trunk. In an unstructured environment, the robot can adaptively grab various

irregular-shaped objects and has flexible obstacle avoidance performance. a_i ($i = 1\sim 7$) are under-actuated joint units in the robSSot. Each under-actuated joint unit is made up of a scissor mechanism, an elastic device, bottom links, and support links. The robot is directly driven by a single motor. Therefore, the output torque of the driving motor has a great influence on the holding stability of the robot. In Figure 1, (a) is the torque sensor and (b) is the driving motor. The inner ring of the sensor is fixed with the driving motor, and the outer ring is fixedly connected with the robot. The torque sensor we designed can accurately measure the output torque of the motor. Therefore, the torque sensor can be well applied to a biomimetic actuation similar to the elephant's trunk robot and is of great significance for studying the stability and performance characteristics of a bionic robot system.

Six types of flexure spring are proposed to be used as the mechanical structure. And the proper optical electronic is selected to measure the torsion of the flexure spring. As a result, six typical torque sensors are designed in Section 2. Simulations of all the six types of torque sensor were done by FEM (finite element method) software ANSYS, which are described in Section 3. Simulation results show that 2-rib torque sensor under 1 Nm load covers the measurement range of the selected optical electronic perfectly. The 2-rib torque sensor is selected to be further studied. And topology optimization of this sensor is represented in Section 3. The 2-rib optical torque sensor is calibrated, and several experiments (linearity, hysteresis, and repeatability) are conducted in Section 4.

2. Sensor Design

Torque sensor can be divided into two main parts, elastic element and sensing element. Elastic element produces torsion under the load of torque. The deformation accuracy is detected and measured by the sensing element (Figure 2). Thus, the applied torque could be acquired by establishing the relationship between the torque and the torsion.

2.1. Sensing Element Design. As the input of torque sensor is usually connected to motor [26, 27], the optical technique less influenced by electrical noise is preferred. In many types of optical detection, we decided to use ultrasmall size of photointerrupter as sensitive element to measure the relative motion of sensor's component. In those products, RPI-131 and RPI-121 are considered as their wide measurement range and small size. Although its size is slightly large, we finally selected RPI-131 to obtain a wide measurement range. The dimension of selected photointerrupter is 4.2 mm × 4.2 mm × 5.2 mm, the measurement range is about 0.6 mm, and its weight is only 0.05 g.

2.2. Elastic Element Design. The performance of elastic element widely varies according to its material and configuration.

2.2.1. Material. Steel, aluminum, and titanium are general materials used in the design of torque sensor. Although the yield stress of aluminum is the smallest, we select it because its density is half of steel and 2/3 of titanium. Also, aluminum

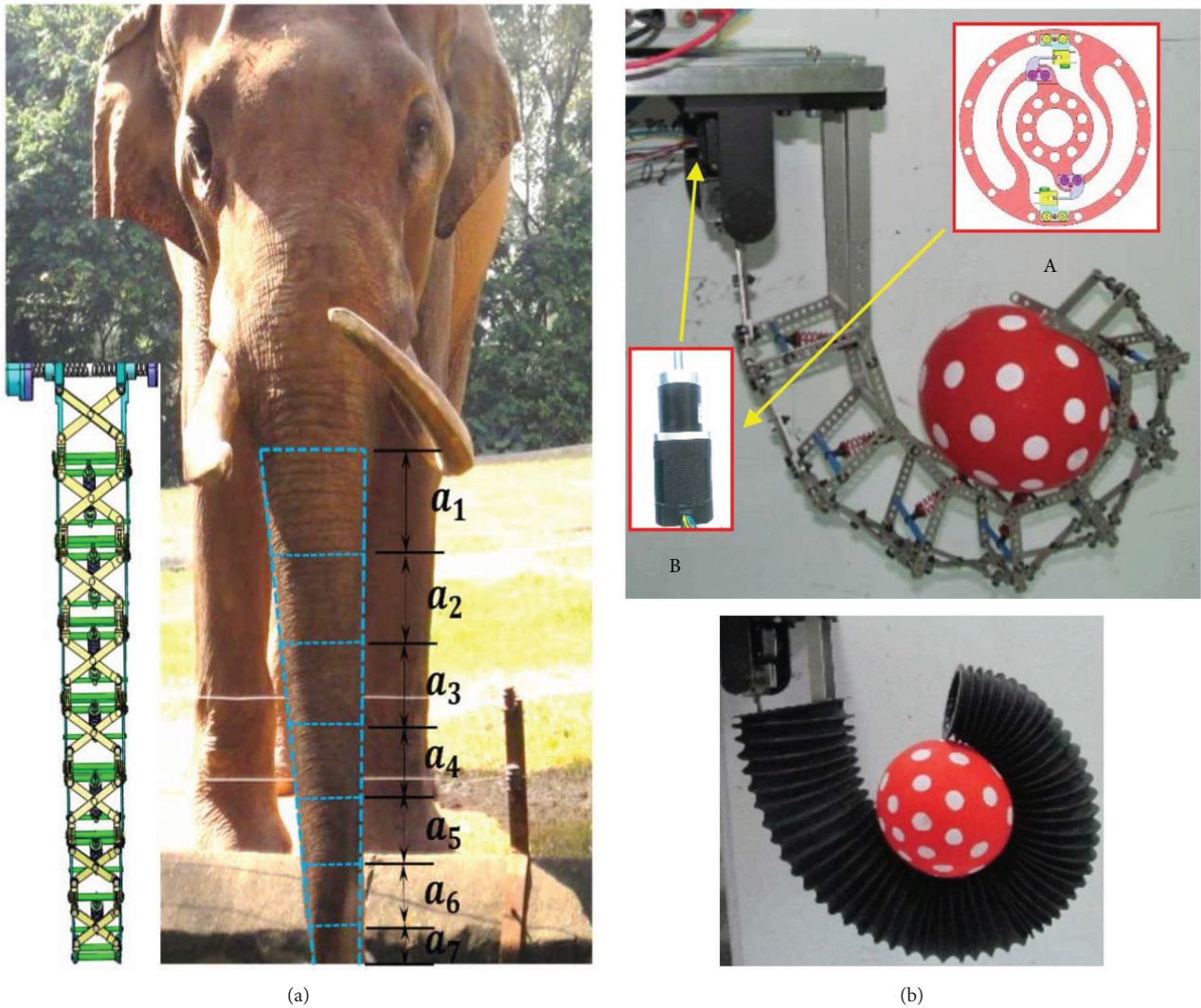


FIGURE 1: Elephant's trunk robot and torque sensor. (a) Elephant's trunk robot; (b) application of torque sensor in biomimetic actuation.

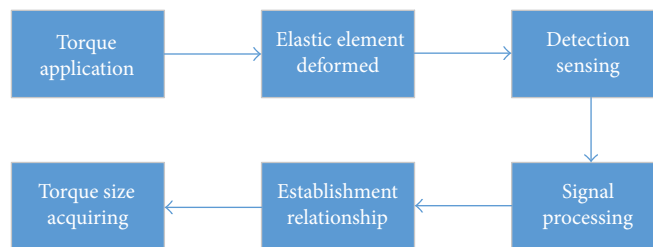


FIGURE 2: Working principle of torque sensor.

is the most economical among these materials. As a result, the aluminum 7075 with yield of 500 MPa is selected to manufacture the elastic element of torque sensor.

2.2.2. Configuration. Two types of shapes, namely, axis structure and crossbeam, are generally used in elastic element design. The axis structure is usually used to load big torque because of its highly reliable performance and its capability to reduce coupling [3, 14, 28, 29]. However, it is difficult to

TABLE 1: Parameters of the torque sensor.

Item	Parameter	Item	Parameter
Diameter	60 mm	Mount	11 mm
Thickness	4 mm	Inner/outer flange	ϕ 3 mm/ ϕ 2.5 mm
Hole	12 mm		

be assembled into small space of a joint. On the other hand, the crossbeam is widely used because of its compact structure and good linearity [1, 4, 5, 7, 12–16]. However, it tends to produce stress concentration and even fail.

Flexure spring has been gradually applied in many fields such as cryocoolers [20, 21], sensors [22–24], and geophones [25] because of its compact structure and highly reliable performance. Contrast to the crossbeam, this structure could be more flexible which is beneficial to the requirement of the relatively wide deformation. In this section, the elastic element design is configured based on the flexure spring.

Because of the variety of the number and angle of ribs, the configuration would have potential for different measurement ranges. Theoretically, the number of ribs could be any. However, one to six ribs are considered feasible. The designed parameters of the torque sensor are mainly determined by the robot joint, whose maximum output torque is 1 Nm. These parameters are shown in Table 1. And the six typical configurations are shown in Table 2.

2.3. Integration. The interrupter shield and bracket were designed to vary the intensity of light and support the photo-interrupter, respectively. The interrupter shield is attached to rib while bracket is attached to outer ring (shown in Table 2). Obviously, we can find that the multirib configurations have a wide measurement range and multidetection, while the sensitivity is much lower.

3. Analysis

In this section, the stiffness equations of the proposed configurations are deduced. With FEM simulation using the software of ANSYS, the theory is examined by building the relationship between design angle and stiffness. The optimal structures in these six typical configurations are selected according to their analysis results. Through the optimization of topology also using ANSYS, we finally acquired the ideal configuration.

3.1. Physical Modeling. The stiffness k means the required torque to produce a unit angle and can be calculated from

$$k = T/\Delta\theta = TR_{\text{out}}/\Delta s, \quad (1)$$

where T is the applied torque, $\Delta\theta$ is the deformed revolving angle, R_{out} is the radius of out flange, and Δs is the produced tangential displacement. While T and R_{out} are given, the core issue is to acquire the formula of torsion in these sensors. To complete it, several assumptions and simplified physical model are needed. Assumptions

- (1) during the deformation, the cross section remains initial conditions;
- (2) for the selected Al-7075, the material of the beam is homogeneous;
- (3) when the deformation is small, the calculation can be seen as linearly elastic.

The built physical model can be seen in Figure 3.

The work done in deflecting the sensor $\Delta\theta$ by torque T is $1/2T\Delta\theta$, and for these parts, the stored energies due to torsion are U_1 , U_2 , and U_3 . Therefore,

$$U = U_1 + U_2 + U_3 = \frac{1}{2}T\Delta\theta. \quad (2)$$

In this model, we accept the equivalent force F and moment M_0 stand for the applied torque T . They are

$$F = \frac{T}{NR_{\text{out}}}, \quad (3)$$

$$M_0 = F(R_{\text{out}} - R_1),$$

where N denotes the number of ribs. For part I, we can calculate the normal force F_{11} and tangential force F_{12} as

$$F_{11} = F \cos \alpha_1, \quad (4)$$

$$F_{12} = F \sin \alpha_1,$$

where α_1 is the angle between F and horizontal. Therefore, the stresses are

$$\sigma_{1x} = \frac{F_{11}}{A} + \frac{F_{12}xy}{I} + \frac{M_0y}{I},$$

$$\sigma_{1y} = 0, \quad (5)$$

$$\tau_{1xy} = \frac{3F_{12}}{2A} \left\{ 1 - \left(\frac{2y}{b} \right)^2 \right\},$$

where A is the sectional area, which can be calculated as $A = b \cdot h$ (h is the thickness and b is the wide). I is the moment of inertia, which is equal to $b^3h/12$. Due to

$$U = \int \frac{1}{2} \sigma \varepsilon dV, \quad (6)$$

where ε is the strain displacement. We can acquire the energy of part I as

$$U_1 = \int \frac{1}{2} \sigma_1 \varepsilon_1 dV = \int \frac{\sigma_{1x}^2}{2E} dV + \int \frac{\tau_{1xy}^2}{2G} dV$$

$$= \int \left(\frac{F_{11}}{A} + \frac{F_{12}xy}{I} + \frac{M_0y}{I} \right)^2 \frac{1}{2E} dV \quad (7)$$

$$+ \int \frac{9F_{12}^2}{8GA^2} \left\{ 1 - \left(\frac{2y}{b} \right)^2 \right\}^2 dV$$

$$= \frac{F_{11}^2 L_1}{2EA} + \frac{F_{12}^2 L_1^3}{6EI} + \frac{M_0^2 L_1}{2EI} + \frac{F_{12} M_0 L_1^2}{2EI} + \frac{3F_{12}^2 L_1}{5GA},$$

where E is the modulus of elasticity, G is the modulus of rigidity, L_1 is the distance between point A and B(x_1, y_1). For part II, in any point $P(x_2, y_2)$ of the ribs, it has

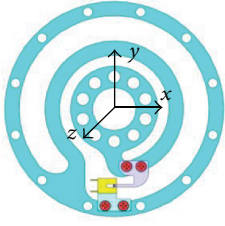
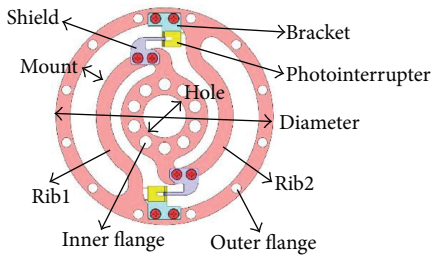
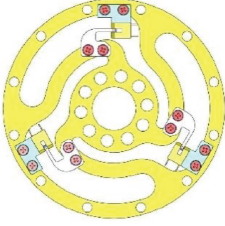
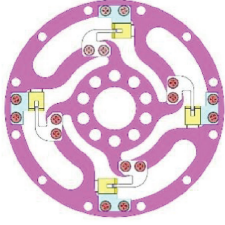
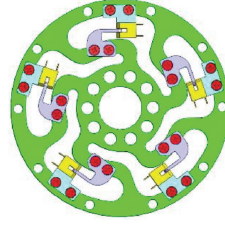
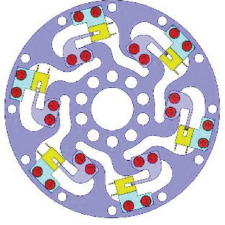
$$V = F \cos \alpha_2,$$

$$N = F \sin \alpha_2, \quad (8)$$

$$M_p = -F_{11}(y_2 - y_1) + F_{12}(x_2 - x_1) + M_1,$$

where V , N , and M_p are the tangential force, normal force, and moment size in point P , respectively. α_2 is the angle

TABLE 2: Six typical configurations.

Number of ribs	1	2	3
Configuration			
Multidetetection	M_z/F_x	M_z, F_x	$M_z, F_x, \text{ and } F_y$
Number of ribs	4	5	6
Configuration			
Multidetetection	$M_z, F_x, \text{ and } F_y$	$M_z, F_x, \text{ and } F_y$	$M_z, F_x, \text{ and } F_y$

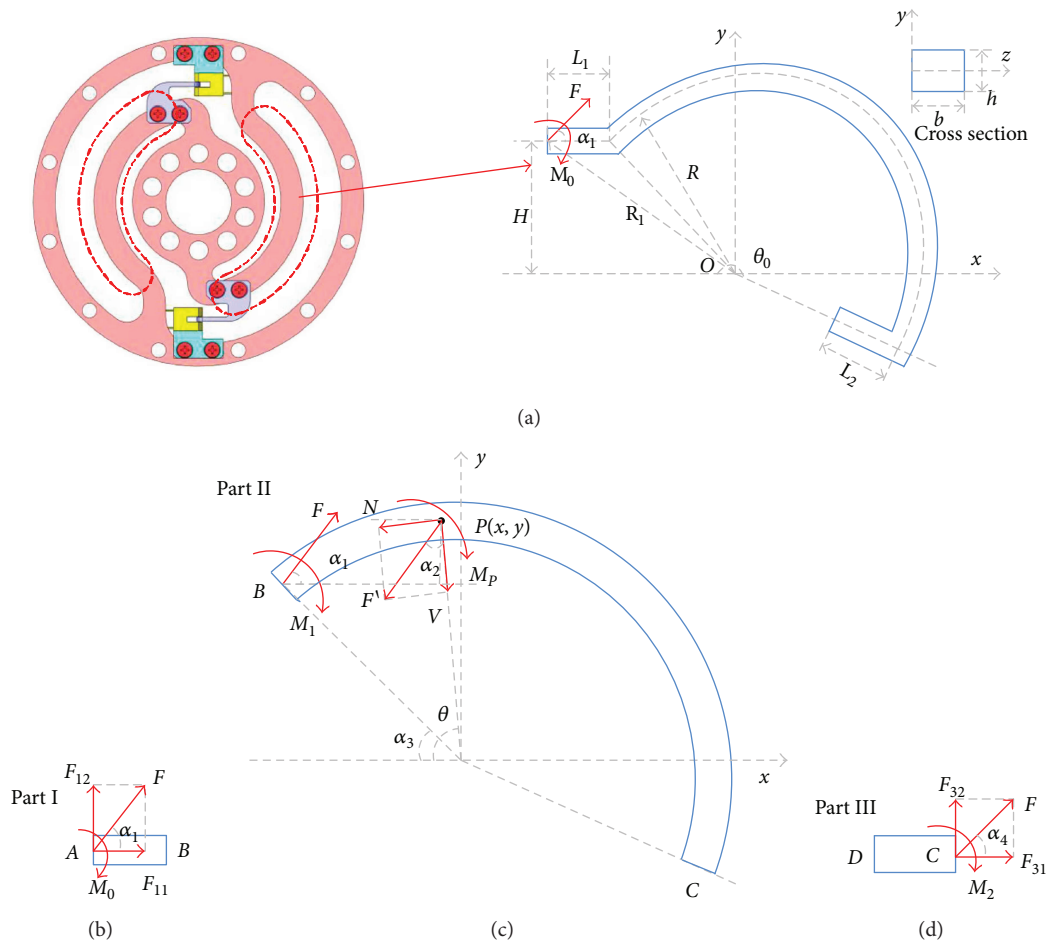
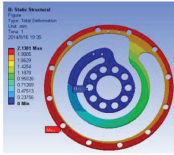
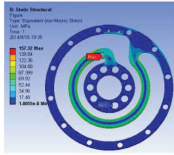
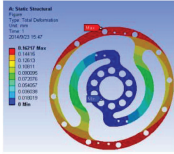
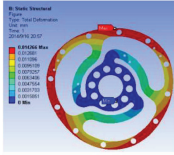
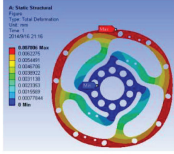
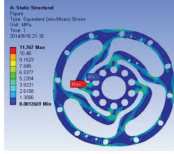
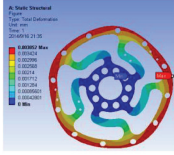
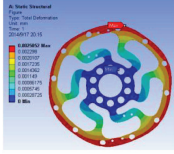
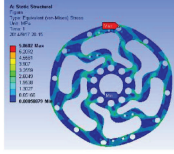
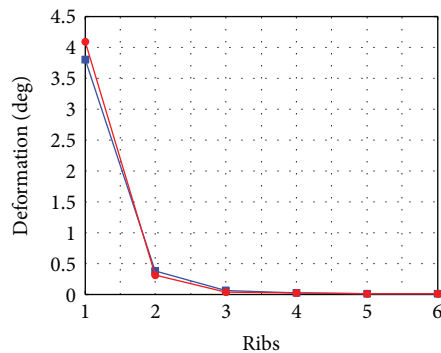


FIGURE 3: Physical model of the torque sensor: (a) overall appearance; (b) part I; (c) part II; (d) part III.

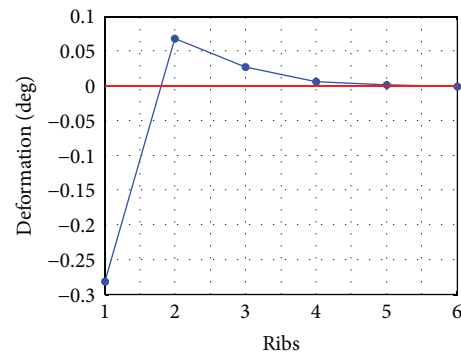
TABLE 3: Results of finite element analysis.

Ribs	Structure	Displacement	Stress	Results
1				Max displacement 4.0835 deg Max stress 157.32 Mpa
2				Max displacement 0.3097 deg Max stress 65.627 Mpa
3				Max displacement 0.0272 deg Max stress 17.55 Mpa
4				Max displacement 0.0134 deg Max stress 11.767 Mpa
5				Max displacement 0.0074 deg Max stress 6.9949 Mpa
6				Max displacement 0.0049 deg Max-stress 5.8602 Mpa



—■— Angle from equation
—●— Angle from FEM

(a)



—■— Error
—●— FEM

(b)

FIGURE 4: Relationship between deformation and the number of ribs: (a) deformation; (b) error.

between F and V , which can be calculated as $\alpha_2 = pi - \theta - \alpha_1$. M_1 is the moment in point B , which is equal to $M_0 + F_{12}L_1$. As the rib is the curve beam, the expression according to the method of energy is given in [30]

$$U_2 = \int \frac{M_p^2}{2AEe} d\theta + \int \frac{kV^2R}{2AG} d\theta + \int \frac{N^2R}{2AE} d\theta - \int \frac{M_pN}{AE} d\theta \quad (9)$$

or

$$U_2 = U_{21} + U_{22} + U_{23} + U_{24}, \quad (10)$$

where k^* is a factor depending on the form of the cross section (for regular section which is equal to 1.2), e is the distance from the centroidal axis to the neutral axis, $e = R - b/[\ln(R + b/2) - \ln(R - b/2)]$, and θ is the angle from axis of x to point P . Therefore, we can separately calculate the energy of $U_{2i}(i = 1, 2, 3, 4)$ as

$$\begin{aligned} U_{21} &= \int \frac{M_p^2}{2AEe} d\theta = \frac{1}{2AEe} \int [-F_{11}(y_2 - y_1) + F_{12}(x_2 - x_1) + M_1]^2 d\theta, \\ U_{22} &= \int \frac{kV^2R}{2AG} d\theta = \frac{kF^2R}{2AG} \int \cos^2(\theta + \alpha_1) d\theta, \\ U_{23} &= \int \frac{N^2R}{2AE} d\theta = \frac{F^2R}{2AE} \int \sin^2(\theta + \alpha_1) d\theta, \\ U_{24} &= - \int \frac{M_pN}{AE} d\theta = \frac{F}{AE} \int [-F_{11}(y_2 - y_1) + F_{12}(x_2 - x_1) + M_1] \sin(\theta + \alpha_1) d\theta, \end{aligned} \quad (11)$$

where the coordinates of point $B(x_1, y_1)$ and point $P(x_2, y_2)$ are

$$\begin{aligned} x_1 &= -R \cos \alpha_3, \\ y_1 &= R \sin \alpha_3, \\ x_2 &= -R \cos \theta, \\ y_2 &= R \sin \theta. \end{aligned} \quad (12)$$

For part III, we can calculate the normal force F_{31} and tangential force F_{32} as

$$\begin{aligned} F_{31} &= F \sin \alpha_4, \\ F_{32} &= F \cos \alpha_4, \end{aligned} \quad (13)$$

where α_4 is the angle between F and horizontal in this part, which can be calculated as $\alpha_4 = \alpha_1 + \theta_0 - pi$. Therefore, the stresses in this part are

$$\begin{aligned} \sigma_{3x} &= \frac{F_{31}}{A} - \frac{F_{32}xy}{I} + \frac{M_2y}{I}, \\ \sigma_{3y} &= 0, \\ \tau_{3xy} &= \frac{3}{2} \frac{F_{32}}{A} \left[1 - \left(\frac{2y}{b} \right)^2 \right], \end{aligned} \quad (14)$$

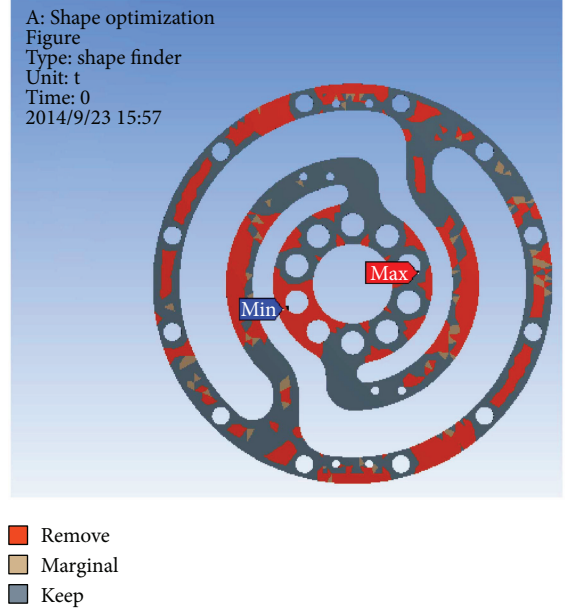


FIGURE 5: Result of optimization.

where M_2 is the moment in point C , which is equal to $F_{12}R(\cos \alpha_3 - \cos \theta_0) - F_{11}R(\sin \theta_0 - \sin \alpha_3) + M_1$. θ_0 is the angle of the rib. The energy of part III can be calculated as

$$\begin{aligned} U_3 &= \int \frac{1}{2} \sigma_3 \epsilon_3 dV + \int \frac{\tau_{3xy}^2}{2G} dV \\ &= \int \left(\frac{F_{31}}{A} - \frac{F_{32}xy}{I} + \frac{M_2y}{I} \right)^2 \frac{1}{2E} dV + \int \frac{9}{4} \frac{F_{32}^2}{GA^2} \\ &\quad \cdot \left[1 - \left(\frac{2y}{b} \right)^2 \right]^2 dV \\ &= \frac{F_{31}^2 L_2}{2EA} - \frac{F_{32}^2 L_2^3}{6EI} - \frac{F_{32} M_2 L_2^2}{2EI} + \frac{M_2^2 L_2}{2EI} + \frac{3 F_{32}^2 L_2}{5GA}. \end{aligned} \quad (15)$$

Therefore, we can find the $\Delta\theta$ as

$$\Delta\theta = \frac{2(U_1 + U_2 + U_3)}{T}. \quad (16)$$

And the stiffness can be obtained as

$$k = \frac{T}{\Delta\theta}. \quad (17)$$

According to these formulations, we could make the conclusion that the stiffness of k is in proportion to the ribs number of N , modulus elasticity of E , and thickness of h .

3.2. FEM Static. The six typical configurations are analyzed by using ANSYS. In the analysis, the mesh type is hexahedron element, and each model comprises approximately 35,000 elements and 140,000 nodes. A fixed constraint is applied to the inner flange, and a torque load of 1 Nm is applied to the outer flange. The analysis results are listed in

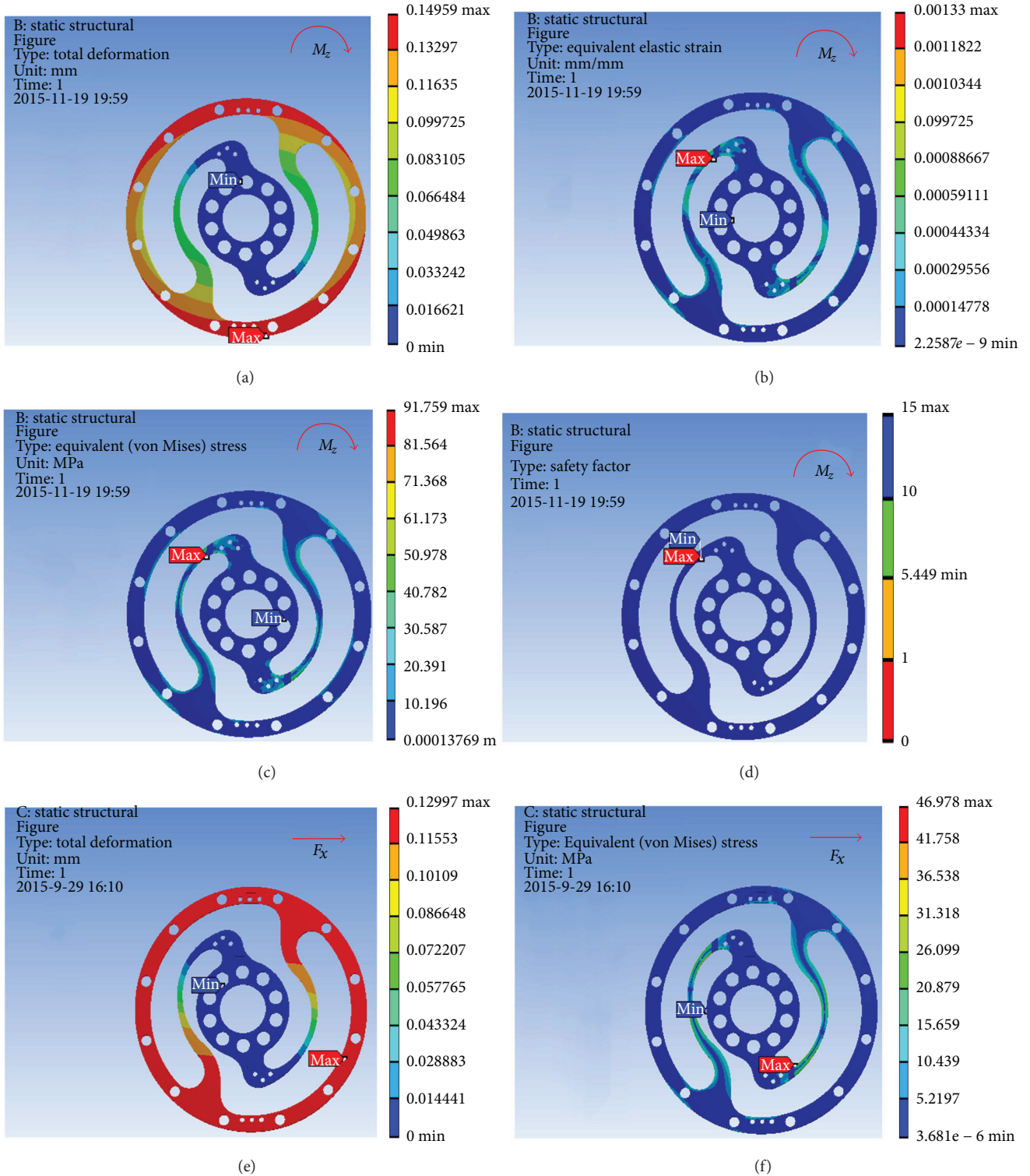


FIGURE 6: FEA results of optimized structure: (a) deformation from M_z ; (b) strain from M_z ; (c) stress from M_z ; (d) factor of safety from M_z ; (e) deformation from F_x ; (f) stress from F_x .

Table 3. The relationship of displacement with those 6 configurations as FEM and formulae is shown in Figure 4.

The displacement of the applied torque of the elastic element was reduced from 2.1381 mm to 0.0025852 mm

when the number of ribs increased. The maximum stress of 157.23 MPa was less than the material yield stress of 500 MPa. Therefore, in this condition, the stress was not the core issue to consider. Finally, the 2-rib structure

was found to be optimal because the deformation of one rib was beyond the measurement range of RPI-131, while the deformation of others was significantly small. Furthermore, the displacement of 0.1627 mm was detectable using the RPI-131.

3.3. FEM Optimization. Optimization was measured to determine the optimal structure. The topology optimization to achieve the lightest weight was conducted using ANSYS with the reliability constraints and stress limitations. An efficient method for topology optimization is reducing the quality and volume to make the model approach the optimized target. In this case, the mechanical performance should be partly retained.

In the analysis, the solid element was accepted. Approximately 90,000 elements and 160,000 nodes were produced in the meshing. Similarly, a fixed constraint was applied to the inner flange, and the torque was loaded at the outer flange. The quality of the target optimization was set to half. Figure 5 shows that the red area could be removed without significantly affecting the performance in mechanics.

Based on the result of optimization, we finally acquired the ideal configuration by modelling with the method of eccentric circle to approach the optimization results. To evaluate the performance of the optimized 2-rib configuration, the static analysis was reconducted. In the analysis, the solid element was also accepted, and approximately 54,000 elements and 98,000 nodes were produced. The same torque load and fixed constraint were applied on the outer and inner flanges, respectively. As this sensor is immune to the loads of M_x , M_y , F_y , and F_z (the deformation from these loads could not be detected by the photointerrupters), the influence by F_x needs to be considered. In the analysis, the force load (15 N) and fixed constraint were also applied on the outer and inner flanges, respectively. Figure 6 shows the analysis results of the optimized 2-rib structure. The comparison of performances between the original and optimized structures is listed in Table 4.

According to (a) to (f) in Figure 6, we can obviously find that under the load of M_z , the deformations detected by the two photointerrupters are identical. While, under the load of F_x , the deformations detected by the two photointerrupters are opposite. Therefore, the error caused by F_x , in a certain range, could be eliminated through the simple signal process such as be average. Eventually, the designed sensor could detect the torque of M_z without influence from other loads.

And through the topology optimization, the results show that the displacement was reduced by 7.01%, and the mass was reduced by 11.15%; meanwhile, the factor of safety was also reduced by 29.63%. Theoretically, the linearity of this sensor can be seen in Figure 7.

4. Experiments and Results

The performances of linearity, hysteresis, and repeatability are important in evaluating the feasibility of the design of torque sensor.

TABLE 4: Comparison of performances of original and optimized structure.

Item	Original	Optimized
Mesh	34,000 elements, 136,000 nodes	60,000 elements, 11,000 nodes
Displacement	0.16086 mm	0.14959 mm
Max stress	64.567 MPa	91.759 MPa
Max strain	0.00089679 mm	0.00133 mm
Factor of safety	7.7439	5.449
Mass	15.442 g	13.72 g

4.1. Experiment Preparation. The sensor, discussed in this paper, is manufactured with a computer numerical control milling machine (Figure 8), and the test system (Figure 9) is built to study its performances. Figure 10 shows the established experiment circuit. The photointerrupter is composed of an infrared light emitting diode (LED) at one side and a transistor (detector) at the other side (shown in Figure 10(a)). The graph in Figure 10(b) shows there is a linear relationship between the distance and the current of the collector. According to this linear relationship, acquiring the applied torque size by detecting shield displacement would be successful. Considering the sensitivity, $U = 10 \text{ V}$ and $R_L = 10 \text{ k}\Omega$ were selected [13]. $R_0 = 833 \Omega$ was chosen for $I \approx (U - U_d)/R_0 = (10\text{V} - 1.16 \text{ V})/833\Omega = 10.4 \text{ mA}$ (where $U_d \approx 1.16 \text{ V}$ that is the voltage drop caused by LED). Channels A and B were linked to the oscilloscope channels 1 and 2, respectively. In this kind of circuit, the maximum output voltage was 9.8 V, and the output voltage in the initial position was approximately 4.5 V.

4.2. Linearity. Linearity describes the degree offset between the actual line and ideal straight line [31, 32]. The torque is achieved (from 0 Nm to 0.98 Nm) by placing load at the lever of the test system, and the increased torque is 0.098 Nm. The experiment is conducted more than 50 times to ensure the acquired data truly reflect the performance of the sensor. The experiment data are recorded in Table 5, and the graphs of linearity and error are drawn in Figure 11. With using polyfit function of MATLAB, the relationship between displacement and applied torque can be built as

$$\Delta = -3.0198T + 4.3250, \quad (18)$$

where Δ is the output voltage and T is the applied torque size. The nonlinearity and torque sensitivity are expressed as

$$\gamma_L = \frac{\Delta L_{\max}}{FS} \times 100\% = \frac{0.0986}{4.325 - 1.3052} \times 100\% = 3.27\%,$$

$$S = \frac{\Delta Y}{\Delta X} = \frac{4.4118 - 1.4038}{0.98} = 3.07 \text{ V/Nm}, \quad (19)$$

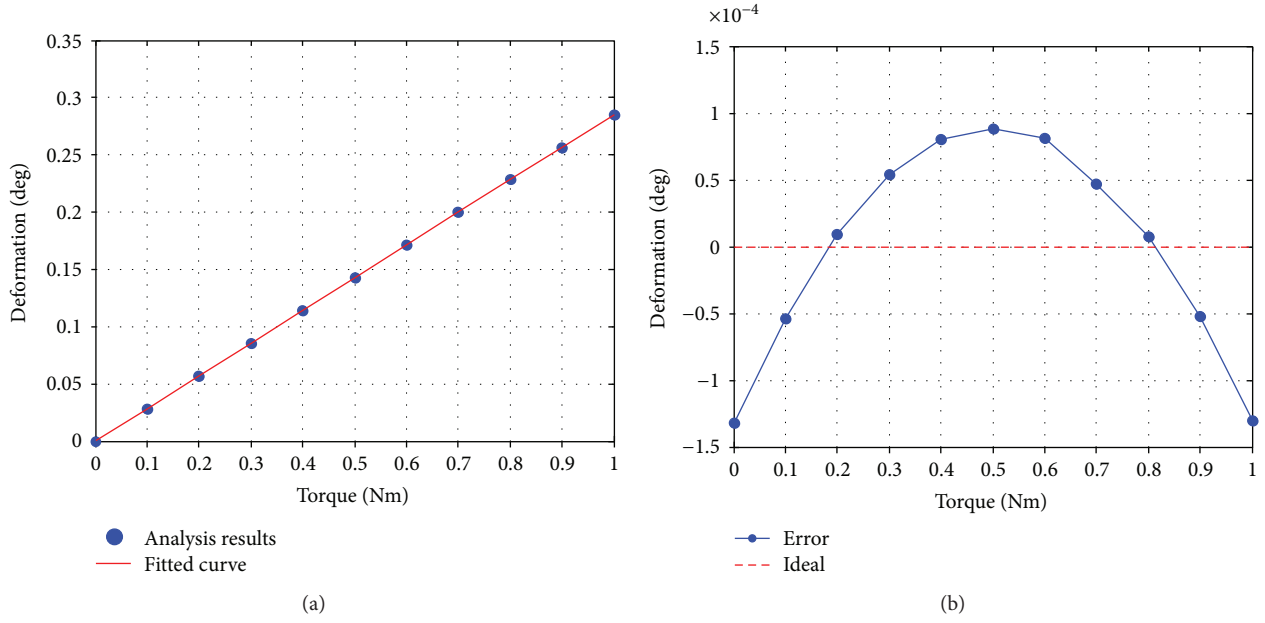


FIGURE 7: Simulation in the range of 0~1 Nm: (a) relationship of torque and displacement; (b) error.

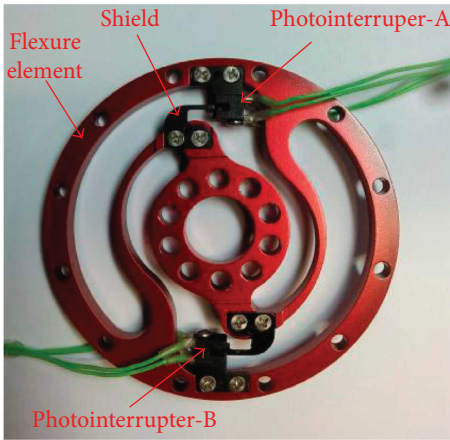


FIGURE 8: Manufactured torque sensor.

where ΔL_{\max} is the maximum error, FS is the full scale, ΔX is the full range of torque input change, and ΔY is the corresponding change in the output voltage.

4.3. Hysteresis. Hysteresis describes the degree of misalignment between the input and output with the forward and backward loads. The hysteresis experiment was tested by applying torque in ascending and descending manners at 0.098 Nm. The results of the hysteresis experiment are shown in Table 6 and Figure 12. The graph of the hysteresis curve was drawn using MATLAB. With a maximum offset ΔH_{\max} of 0.006 V, the hysteresis is calculated as

$$\gamma_H = \frac{\Delta H_{\max}}{FS} \times 100\% = 0.2\%. \quad (20)$$

4.4. Repeatability. Repeatability is usually necessary when an unsteady system is used to measure errors. Each graph in Figure 13 shows the results of the applied torque repeatedly applied for 50 times. The graph means that with the application of the same torque, the frequency of equal output voltage can be detected. For the maximum span ΔR_{\max} of 0.07 V, the repeatability can be calculated as (21). The graph presents the detected frequency of equal output voltage applying the same torque.

$$\gamma_R = \frac{\Delta R_{\max}}{FS} \times 100\% = 2.32\%. \quad (21)$$

4.5. Factor of Safety. Generally, that the most effective method to evaluate the property of factor of safety is to conduct the experiment of overload. The experiment is conducted with 0.5 Nm increment of load from 1 Nm to 5 Nm. In each load, the experiment is conducted about 3 times with maintaining load at least 5 minutes. After removing the load, the output voltage of photointerrupter is recorded in Table 7. From the results, we can clearly find that in the range of 1 Nm to 4.5 Nm, this sensor could operate normally, while at the torque size of 5 Nm, it has been failed. Therefore, the factor of safety of this sensor should be about 4.5.

4.6. Evaluation. The performance of the designed torque sensor is shown in Table 8. Recently, the research of flexible spring applied to the torque sensor is less. Obviously, the linearity is a little insufficient which may be caused by its principle of sensing element or the especially flexure spring. However, compared with other optical torque sensors [12–14], the torque sensor designed in this paper has a wide measure range and a small diameter, while

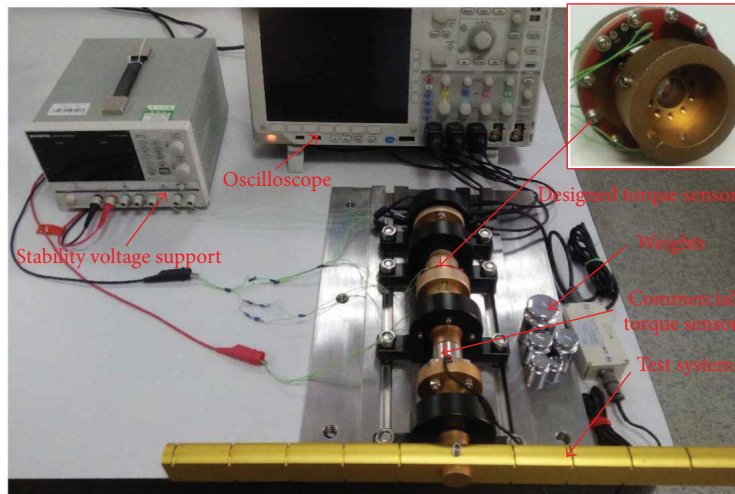


FIGURE 9: Calibrate test system.

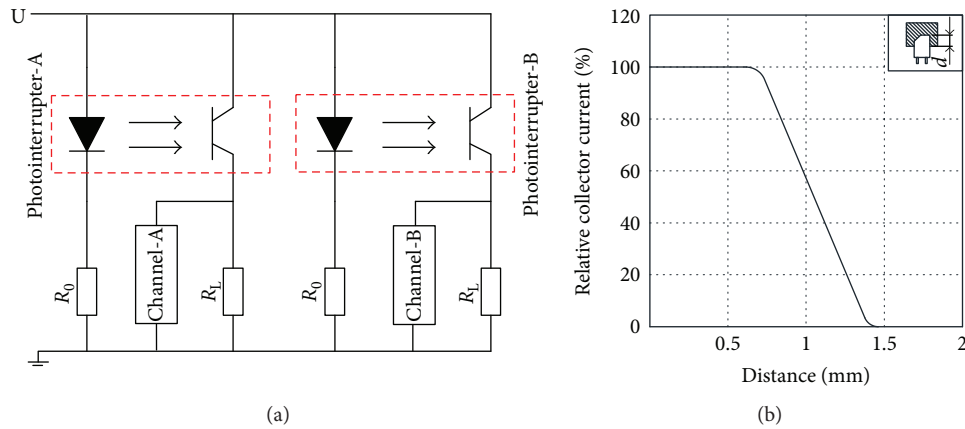
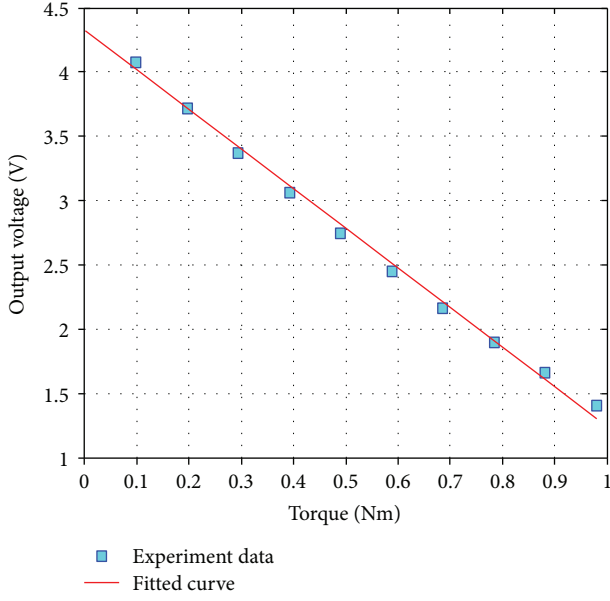


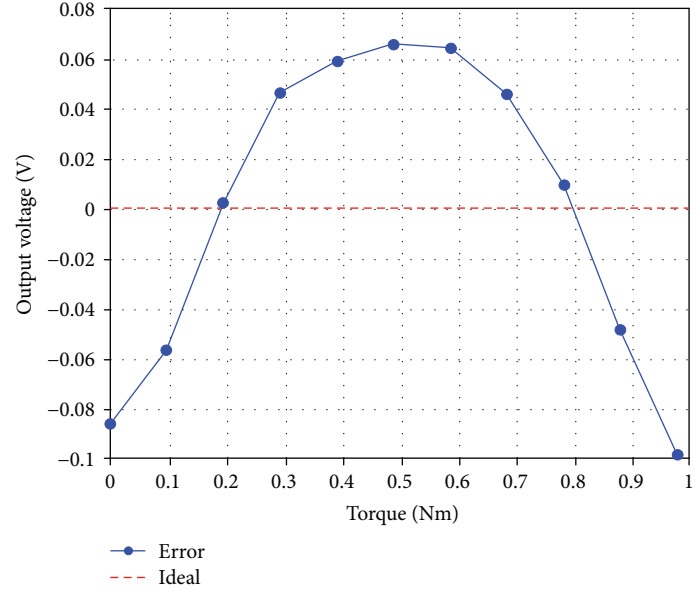
FIGURE 10: Experiment circuit: (a) working principle of photointerrupter; (b) measure range.

TABLE 5: Experiment data.

Torque (Nm)	Minimum (V)	Maximum (V)	Average (V)	Calculate (V)	Error	% error
0	4.40	4.43	4.4118	4.3250	-0.0868	2.87
0.098	4.05	4.12	4.0800	4.0231	-0.0569	1.88
0.196	3.70	3.75	3.7190	3.7211	0.0021	0.70
0.294	3.35	3.40	3.3730	3.4191	0.0461	1.53
0.392	3.04	3.08	3.0586	3.1171	0.0585	1.94
0.49	2.73	2.77	2.7496	2.8151	0.0655	2.17
0.588	2.43	2.47	2.4494	2.5131	0.0637	2.11
0.686	2.15	2.19	2.1654	2.2112	0.0458	1.52
0.784	1.89	1.92	1.8998	1.9092	0.0094	0.31
0.882	1.64	1.67	1.6560	1.6072	-0.0488	1.62
0.98	1.39	1.42	1.4038	1.3052	-0.0986	3.27



(a)



(b)

FIGURE 11: Experiment results of applied torque and resulting output: (a) linearity; (b) error.

TABLE 6: Results of hysteresis.

Torque (Nm)	Forward (V)	Backward (V)	Error (V)
0	4.410	4.407	0.003
0.098	4.079	4.079	0.000
0.196	3.717	3.717	0.000
0.294	3.372	3.370	0.002
0.392	3.060	3.054	0.006
0.49	2.746	2.746	0.000
0.588	2.446	2.441	0.005
0.686	2.160	2.160	0.000
0.784	1.894	1.892	0.002
0.882	1.650	1.649	0.001
0.98	1.398	1.398	0.000

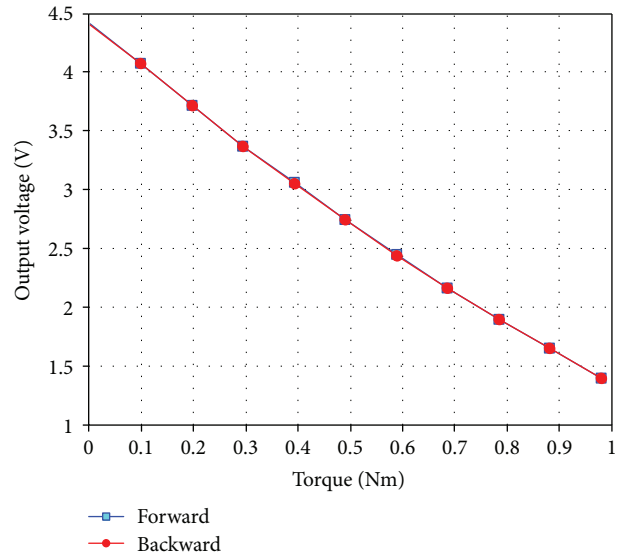


FIGURE 12: Hysteresis curve.

the thickness of only 4mm is the best of them. At the same time, it is equally satisfied with a light mass and a high safety factor; hence, it has a compact and smart structure that can be perfectly applied to biomimetic robot joints.

5. Conclusion

In this paper, a highly reliable optical torque sensor is developed for biomimetic robot joints in extreme embedded applications. To ensure the high reliability, the structure is designed based on a flexure spring, which is most commonly used in many fields. The thickness is reduced to 4mm, the weight is 16g, and the factor of safety is 4.5. The torque

sensor is very small for being used in a biomimetic joint with a maximum output torque size of 1Nm obviously. The linearity, sensitivity, repeatability, and hysteresis are 4.31%, 2.06 V/Nm, 2.67%, and 0.2%, respectively. In the future, using signal process to promote its performance and studying multforce/moment condition with similar size are worth considering. Improving the measurement dimension of the torque sensor and its application capacity in the new generation of biomimetic robot joints are our next vision and priorities.

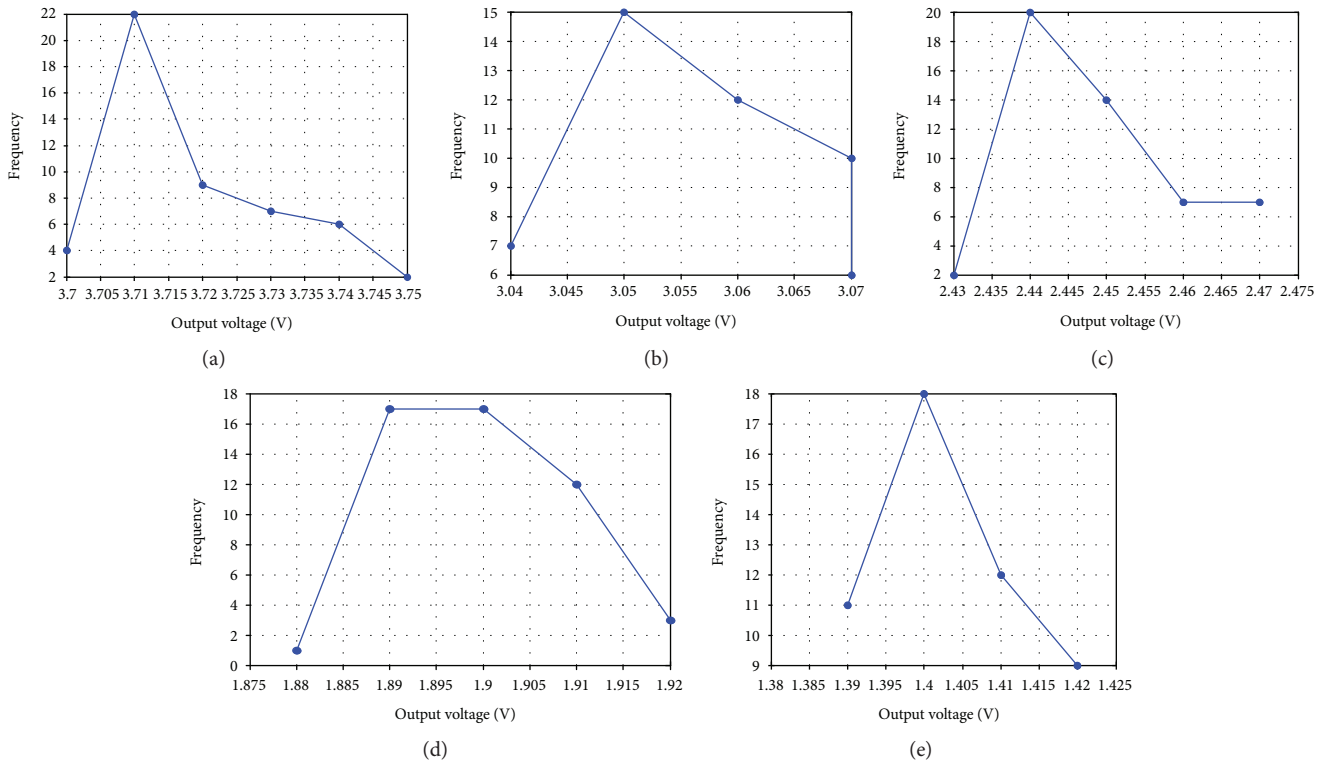


FIGURE 13: Repeatability curve: (a) torque 0.196 Nm; (b) torque 0.392 Nm; (c) torque 0.588 Nm; (d) torque 0.784 Nm; (e) torque 0.98 Nm.

TABLE 7: Data of overload experiment.

Torque (Nm)	1	1.5	2	2.5	3.0	3.5	4	4.5	5
1 (V)	4.41	4.40	4.40	4.41	4.42	4.41	4.40	4.42	4.41
2 (V)	4.41	4.42	4.39	4.40	4.42	4.40	4.41	4.42	4.35
3 (V)	4.40	4.40	4.39	4.41	4.42	4.40	4.41	4.41	4.21

TABLE 8: Performances of designed torque sensor.

Item	Optical torque sensor
Mass	16 g
Diameter	60 mm
Thickness	4 mm
Factor of safety	4.5
Linearity	3.27%
Sensitivity	3.06 V/Nm
Repeatability	2.32%
Hysteresis	0.2%

Conflicts of Interest

The authors declare no conflict of interest.

Acknowledgments

This research is supported by the National Natural Science Foundation of China (no. 51605474), Foundation of State Key Laboratory of Robotics (no. 2016-Z09), and Innovation

Foundation for National Defense Science and Technology of Chinese Academy of Sciences (CXJJ-17-M109).

References

- [1] D. Tsetserukou, N. Kawakami, and S. Tachi, "Design, control and evaluation of a whole-sensitive robot arm for physical human-robot interaction," *International Journal of Humanoid Robotics*, vol. 6, no. 4, pp. 699–725, 2009.
- [2] V. A. Ho, D. V. Dao, S. Sugiyama, and S. Hirai, "Development and analysis of a sliding tactile soft fingertip embedded with a microforce/moment sensor," *IEEE Transactions on Robotics*, vol. 27, no. 3, pp. 411–424, 2011.
- [3] Q. Liang, D. Zhang, Y. Ge, and Q. Song, "A novel miniature four-dimensional force/torque sensor with overload protection mechanism," *IEEE Sensors Journal*, vol. 9, no. 12, pp. 1741–1747, 2009.
- [4] M. K. Kang, S. Lee, and J. H. Kim, "Shape optimization of a mechanically decoupled six-axis force/torque sensor," *Sensors and Actuators A: Physical*, vol. 209, pp. 41–51, 2014.
- [5] R. Ma, A. H. Slocum, E. Sung, J. F. Bean, and M. L. Culpepper, "Torque measurement with compliant mechanisms," *Journal of Mechanical Design*, vol. 135, no. 3, article 034502, 2013.
- [6] I. M. Kim, H. S. Kim, and J. B. Song, "Embedded joint torque sensor with reduced torque ripple of harmonic drive," in *Intelligent Autonomous Systems 12*, pp. 633–640, Springer-Verlag, Berlin, Germany, 2013.
- [7] D. Kim, C. H. Lee, B. C. Kim et al., "Six-axis capacitive force/torque sensor based on dielectric elastomer," in *Electroactive Polymer Actuators and Devices (EAPAD) 2013*, San Diego, California, USA, April 2013.

- [8] F. Beyeler, S. Muntwyler, and B. J. Nelson, "A six-axis MEMS force-torque sensor with micro-Newton and nano-Newtonmeter resolution," *Journal of Microelectromechanical Systems*, vol. 18, no. 2, pp. 433–441, 2009.
- [9] A. M. Madni, J. B. Vuong, D. C. H. Yang, and B. Huang, "A differential capacitive torque sensor with optimal kinematic linearity," *IEEE Sensors Journal*, vol. 7, no. 5, pp. 800–807, 2007.
- [10] J. Liu, M. Li, L. Qin, and J. Liu, "Active design method for the static characteristics of a piezoelectric six-axis force/torque sensor," *Sensors*, vol. 14, no. 12, pp. 659–671, 2014.
- [11] Y.-J. Li, G.-C. Wang, D. Zhao, X. Sun, and Q.-H. Fang, "Research on a novel parallel spoke piezoelectric 6-DOF heavy force/torque sensor," *Mechanical Systems and Signal Processing*, vol. 36, no. 1, pp. 152–167, 2013.
- [12] J. C. Kim, K. S. Kim, and S. Kim, "Note: a compact three-axis optical force/torque sensor using photo-interrupters," *Review of Scientific Instruments*, vol. 84, no. 12, article 126109, 2013.
- [13] S. Shams, J. Y. Lee, and C. Han, "Compact and lightweight optical torque sensor for robots with increased range," *Sensors and Actuators A: Physical*, vol. 173, no. 1, pp. 81–89, 2012.
- [14] D. Tsetserukou, R. Tadakuma, H. Kajimoto, and S. Tachi, "Optical torque sensors for implementation of local impedance control of the arm of humanoid robot," in *Proceedings 2006 IEEE International Conference on Robotics and Automation, 2006. ICRA 2006*, pp. 1674–1679, Orlando, Florida, USA, May 2006.
- [15] G. Palli and S. Pirozzi, "An optical torque sensor for robotic applications," *International Journal of Optomechatronics*, vol. 7, no. 4, pp. 263–282, 2013.
- [16] G. Palli, L. Moriello, U. Scarcia, and C. Melchiorri, "Development of an optoelectronic 6-axis force/torque sensor for robotic applications," *Sensors and Actuators A: Physical*, vol. 220, pp. 333–346, 2014.
- [17] P. Horváth and A. Nagy, "Optical torque sensor development," in *Recent Advances in Mechatronics*, pp. 91–96, Springer-Verlag, Berlin, Germany, 2010.
- [18] D. E. Choi, G.-H. Yang, J. Choi, W. Lee, C. Cho, and S. Kang, "A safe joint with a joint torque sensor," in *2011 8th International Conference on Ubiquitous Robots and Ambient Intelligence (URAI)*, pp. 331–336, Incheon, Korea, November 2011, Songdo Conventi A.
- [19] R. Haslinger, P. Leyendecker, and U. Seibold, "A fiberoptic force-torque-sensor for minimally invasive robotic surgery," in *2013 IEEE International Conference on Robotics and Automation*, pp. 4390–4395, Karlsruhe, Germany, May, 2013.
- [20] N. Chen, X. Chen, Y.-N. Wu, C.-G. Yang, and L. Xu, "Spiral profile design and parameter analysis of flexure spring," *Cryogenics*, vol. 46, no. 6, pp. 409–419, 2006.
- [21] R. Pan, A. L. Johnson, and T. E. Wong, "Tangential linear flexure bearing," *US Patent*, vol. 7407493, p. B2, 1996.
- [22] M. A. Diftler, J. S. Mehling, M. E. Abdallah et al., "Robonaut 2 - the first humanoid robot in space," in *2011 IEEE International Conference on Robotics and Automation*, pp. 2178–2183, Shanghai, China, May 2011.
- [23] C. A. Ihrke, A. H. Parsons, J. S. Mehling, and B. K. Griffith, "Planar torsion spring," *US Patent*, vol. 8176809, p. B2, 2010.
- [24] L.-S. Fan, Y.-C. Tai, and R. S. Muller, "Integrated movable micromechanical structures for sensors and actuators," *IEEE Transactions on Electron Devices*, vol. 35, no. 6, pp. 724–730, 1988.
- [25] D. M. Woo, "Geophone spring," *US Patent*, vol. 5134594, 1992.
- [26] A. Albu-Schäffer, S. Haddadin, C. Ott, A. Stemmer, T. Wimböck, and G. Hirzinger, "The DLR lightweight robot: design and control concepts for robots in human environments," *Industrial Robot: An International Journal*, vol. 34, no. 5, pp. 376–385, 2007.
- [27] X. H. Gao, M. H. Jin, Z. W. Xie et al., "Development of the Chinese intelligent space robotic system," in *2006 IEEE/RSJ International Conference on Intelligent Robots and Systems*, pp. 994–1001, Beijing, China, October 2006.
- [28] D. Wang, J. Guo, C. Sun, M. Xu, and Y. Zhang, "A flexible concept for designing multi-axis force/torque sensors using force closure theorem," *IEEE Transactions on Instrumentation and Measurement*, vol. 62, no. 7, pp. 1951–1959, 2013.
- [29] W.-C. Yang, B. Song, Y. Yu, and Y.-J. Ge, "Design of a micro six-axis force sensor based on double layer E-type membrane," in *2008 International Conference on Information and Automation*, pp. 1632–1636, Zhangjiajie, China, June 2008.
- [30] W. C. Young and R. C. Budynas, *Roark's Formulas for Stress and Strain*, McGraw-Hill, New York, USA, 2002.
- [31] M. J. McGrath and C. N. Scanail, "Sensing and sensor fundamentals," in *Sensor Technologies*, pp. 15–45, Apress, Berkeley, USA, 2013.
- [32] J. Fraden, "Sensor characteristics," in *Handbook of Modern Sensors*, Springer, New York, USA, 2010.
- [33] D.-D. Wang, Y.-W. Liu, and L.-J. Fang, "Kinematics and mechanics simulation analysis of space multi-unit underactuated mechanism," in *Mechatronics and Manufacturing Technologies*, pp. 211–216, Wuhan, China, August 2016.
- [34] Y. Noh, J. Bimbo, S. Sareh et al., "Multi-axis force/torque sensor based on simply-supported beam and optoelectronics," *Sensors*, vol. 16, no. 11, 2016.

Research Article

CMM-Based Volumetric Assessment Methodology for Polyethylene Tibial Knee Inserts in Total Knee Replacement

Wei Jiang ¹, Cuicui Ji,² Zhongmin Jin,³ and Yuntian Dai¹

¹School of Mechanical and Automobile Engineering, Changzhou Institute of Technology, Changzhou, Jiangsu 213032, China

²School of Mechanical and Electrical Engineering, Hohai University, Changzhou, Jiangsu 213022, China

³Leeds Joint School, Southwest Jiaotong University, Chengdu, Sichuan 611756, China

Correspondence should be addressed to Wei Jiang; jwei@czust.edu.cn

Received 3 November 2017; Revised 16 January 2018; Accepted 19 February 2018; Published 10 April 2018

Academic Editor: David Vokoun

Copyright © 2018 Wei Jiang et al. This is an open access article distributed under the Creative Commons Attribution License, which permits unrestricted use, distribution, and reproduction in any medium, provided the original work is properly cited.

Total knee replacement is a common surgical procedure in orthopaedics. Accurate volumetric wear assessment of the polyethylene knee inserts has been an essential subject for improving the longevity. A new CMM-based methodology was presented to determine volumetric material loss based on curve surface fitting without prewear data, CAD model, or original design of drawings. Both computational and experimental simulated volume removal tests were run to validate the methodology by comparing with the gravimetric measurements. The volume and linear wear of the tibial inserts were calculated using the presented method based on the coordinates acquired by the CMM. The results indicate that the methodology is adequate for clinically retrieved tibial inserts where no prewear data are provided. This technique can also be used for biotribological study of other polyethylene components, since wear and damage can be assessed visually and volumetrically.

1. Introduction

Total knee replacement (TKR) is being widely used as a successful and effective treatment of degenerative knee joint diseases, about 80 percent of which were carried out because of osteoarthritis of the knee, and the number of knee replacement operations is increasing every year worldwide [1]. CoCrMo alloy, ultra-high molecular weight polyethylene (UHMWPE), and more recently, ceramics are used in the prosthesis manufacturing process for reducing the wear and improving the longevity of implants thanks to their significant advantages in terms of low friction coefficient and good antiwear property. However, wear of polyethylene bearing component is a major problem in total knee replacement, and studies have shown that about 16 percent of knees fail due to polyethylene wear [2]. Therefore, accurate wear assessment of the polyethylene knee inserts has been an essential subject for improving the longevity [3]. Wear measurement methodologies become critically important if differentiations with respect to materials and design are sought when geometry change is small, which can consist of both wear and creep. There are many methods of

determining the volume loss of polyethylene in the hip, knee, and spine either using contact or noncontact procedures. Volumetric measurements are commonly performed using tactile coordinate measuring machines (CMM) [4–6] or non-contact techniques such as micro X-ray computed tomography (CT) [7] and gravimetric method [8, 9]. CMM has been proved to be an accurate technique for volumetric assessment [10, 11]; however, CMM measurement can induce deformations on polymeric-bearing components due to clamping and probing forces [12]. The aim of this study was to develop a novel methodology based on three-dimensional (3-D) geometry acquired by means of a tactile CMM to determine volumetric material loss of polyethylene tibial knee inserts and validate its effectiveness on the basis of computational and experimental studies of simulated volume removal tests.

2. Materials and Methods

An unworn PFC Sigma tibial knee component (manufactured by DePuy Synthes, UK) was used for the experimental investigations presented in this work. The original surface

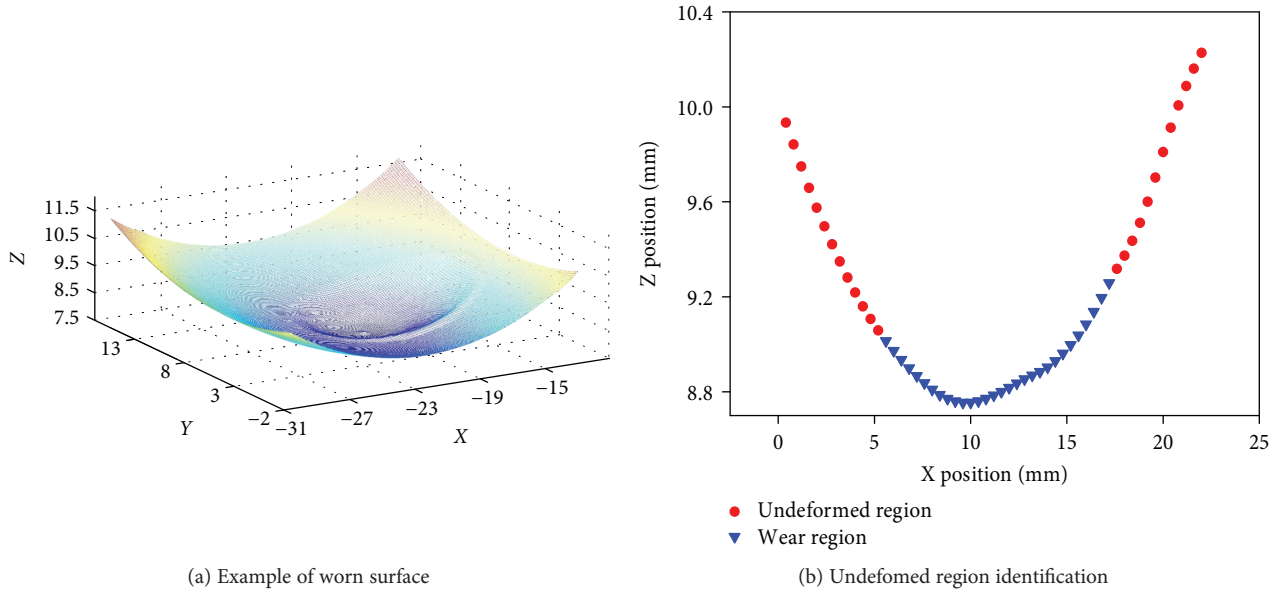


FIGURE 1: Example of polyethylene worn surface and undeformed region identification.

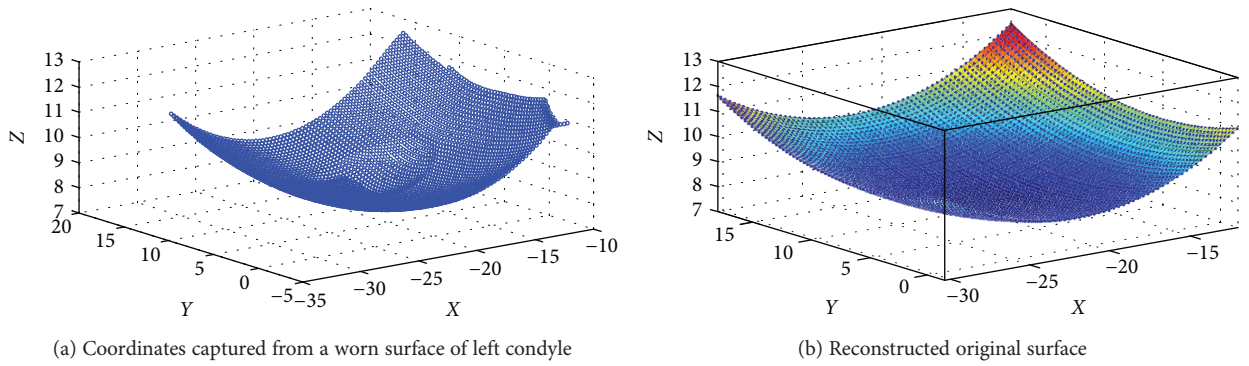


FIGURE 2: Surface coordinates obtained using CMM and reconstructed original surface for volumetric assessment.

coordinates of the left condyle were obtained using a coordinate measuring machine (Mitutoyo Legex 322). The coordinates obtained from the unworn tibial knee inserts were considered as the prewear data and used as reference for both computational and experimental simulated volume removal tests, which were used to validate the volumetric assessment methodology by comparing with the prewear data. From the captured 3-D coordinates, a three-dimensional surface was then established. The wear region was determined according to the difference of Z value between two adjacent coordinates, and it can be judged to be worn out when the difference is greater than 0.1 mm. It is important to note that some clearly wrong coordinates need to be removed for accurate wear region identification. Thus, the undeformed region was identified automatically using a MATLAB (Version 8.3, Mathworks Inc., USA) program (Figure 1), which was used as a reference for volume loss assessment in the conditions where no prewear data was provided [13, 14]. A 5th-order polynomial curve surface fitting algorithm (1) was used to generate the original 3-D surface based on this undeformed region (Figure 2).

$$\begin{aligned}
 f(x, y) = & P00 + P10x + P01y + P20x^2 + P11xy + P02y^2 \\
 & + P30x^3 + P21x^2y + P12xy^2 + P03y^3 + P40x^4 \\
 & + P31x^3y + P22x^2y^2 + P13xy^3 + P04y^4 + P50x^5 \\
 & + P41x^4y + P32x^3y^2 + P23x^2y^3 + P14xy^4 + P05y^5,
 \end{aligned} \tag{1}$$

where P_{ij} are the parameters in polynomial surface fitting algorithm, i is the degree in x , and j is the degree in y .

Prior to the CMM measurement, the polyethylene inserts were cleaned using detergent water then soaked in 1% Trigen solution (MediChem International Ltd., Seven Oaks, UK) to clean the specimen for 30 minutes to remove contaminants from the surface. Afterwards, the inserts were soaked in isopropanol solution (Fisher Scientific, Loughborough, UK) mixed with water (70% isopropanol: 30% water) and placed in an ultrasonic bath (VWR Labshop, IL, USA) for 10 minutes (IMBE simulator test protocol, Leeds University, UK). Then, the components were stored in the weighing room, which is temperature and humidity controlled (21°C

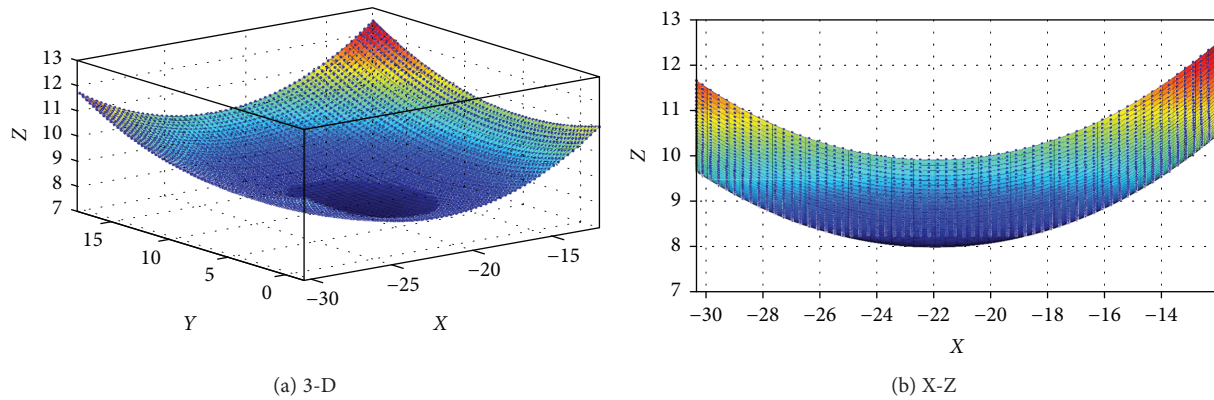


FIGURE 3: Computational simulated volume removal test (the dark blue area is the worn region).

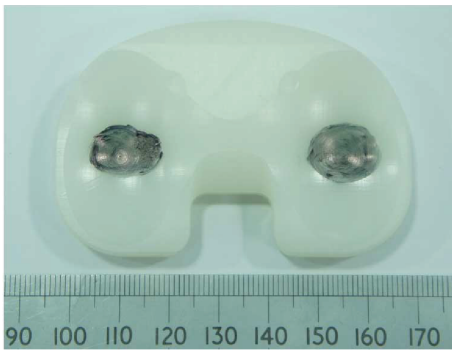


FIGURE 4: Experimental simulated volume removal test (the black area with the ink painting is the worn region).

and 40%, resp.) and allowed to stabilize for a period of 48 hours. The change in mass was assessed using the AT 201 balance (Mettler Toledo Inc., Columbus, Ohio, USA), and the volumetric loss was calculated using 2, taking the density of polyethylene as 0.931 g/mm^3 [5]. For computational simulated volume removal test, the coordinates from the left condyle were used for the development of a computational program to artificially generate different wear areas and depths via a MATLAB program (Figure 3). The wear region of the left condyle ranges from 0.29% to 38.55%, and the maximum wear depth was 0.2 mm. For experimental simulated volume removal test, a 24 mm diameter ball-ended cutter was used to remove physical materials on the left condyle of the tibial knee inserts with maximum wear depths from 0.1 mm to 1 mm (Figure 4). The volume loss of the polyethylene tibial knee inserts was calculated using the presented methodology based on the coordinates captured by the CMM, respectively.

$$\text{Volume loss} = \frac{\text{weight change}}{\text{density}}. \quad (2)$$

3. Results and Discussion

An unworn tibial knee component was used to investigate the influence of the CMM scan interval (0.1 mm, 0.2 mm, 0.5 mm, 1.0 mm, 1.5 mm, and 2.0 mm), and the results were

demonstrated in Figure 5, with the increasing interval of the CMM scan, the points measured decreased from 31,133 to 90 and the volume difference increased from 0.1 mm^3 to 8.1 mm^3 , meanwhile the time taken decreased from 519 minutes to 1.5 minutes. As a result, the scan interval with 0.2 mm was adopted in this study to balance accuracy and time costs (7872 points measured and time taken was 132 minutes). As shown in Figure 6(a), a total of 17 computational wear tests were performed on the left condyle of the tibial knee component to generate different volumes of wear with an increasing wear area. A comparison of theoretical wear volume calculated using coordinates before and after wear test and determined wear volume calculated using surface curve fitting was performed. The simulated volume loss generated using computational model ranges from 0.1 mm^3 to 17.4 mm^3 , and the determined wear volume was very close (maximum error equal to 0.2 mm^3) to the theoretical with concordance correlation coefficients (CCC) of 0.9997 (Figure 7(a)). As illustrated in Figure 6(b), the gold standard gravimetric measurement was chosen as a reference for validation of the 3-D curve surface fitting method in physical volume removal tests. The wear volume generated by the ball-ended cutter was gravimetrically measured using the AT 201 balance (Mettler Toledo Inc., Columbus, Ohio, USA) and ranged from 0.9 mm^3 to 19.3 mm^3 , and the validation results indicated that the methodology is accurate for assessment of wear volume (maximum errors equal to 0.2 mm^3 and 1.1 mm^3 , resp.), with CCC of 0.9998 and 0.9960 with and without initial surface coordinates, respectively (Figure 7(b)). The corresponding wear volume assessed by the presented methodology ranged from 1.0 mm^3 to 19.5 mm^3 and from 0.8 mm^3 to 18.2 mm^3 , respectively.

Initial geometric measurement of specimens or design drawings would be ideal as a reference for volumetric wear assessment; however, these are not always available [15, 16]. This study presented a CMM-based methodology to determine volumetric material loss based on 3-D curve surface fitting, and the validation results indicated that the methodology is adequate for both laboratory and clinically retrieved tibial knee inserts where no prewear data, CAD models, or original design drawings are available. Further

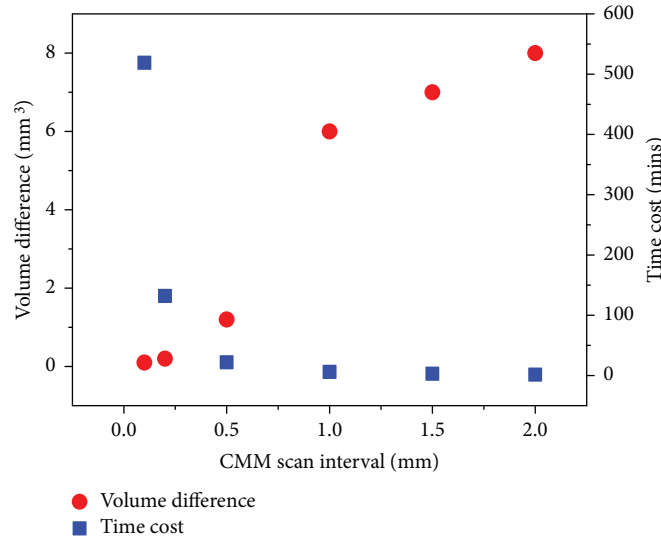


FIGURE 5: The influence of CMM scan interval on volume difference.

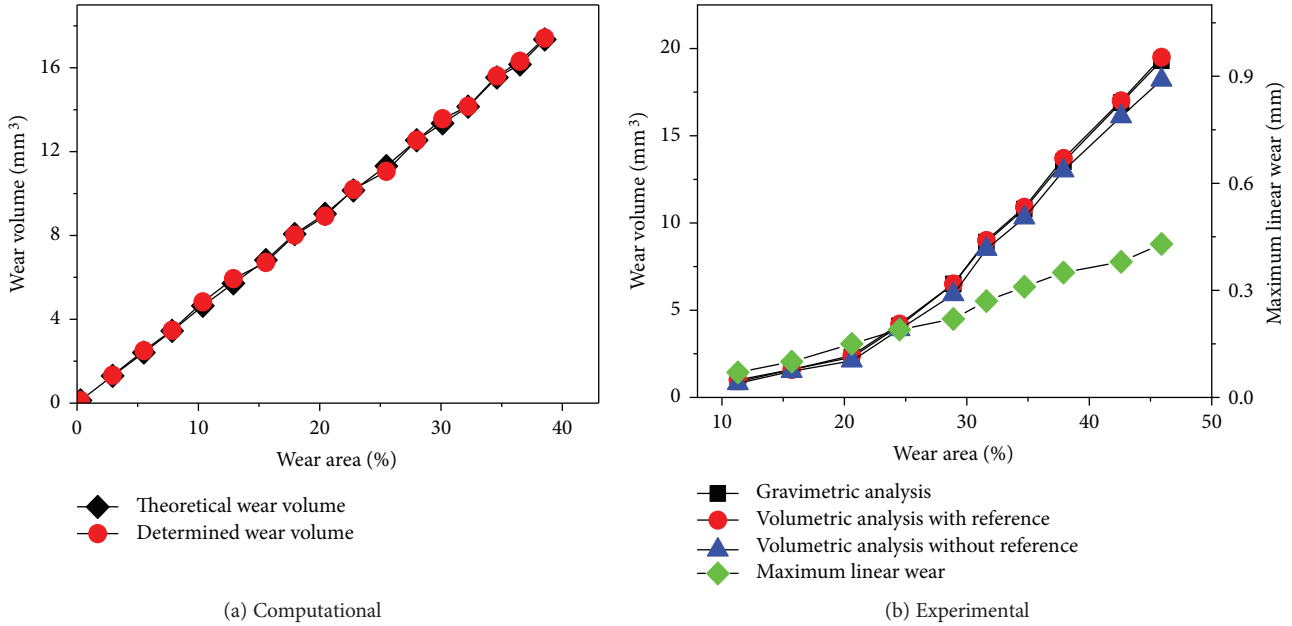


FIGURE 6: Computational and experimental simulated volume removal test results.

studies indicated that at least 50 percent undeformed region of each condyle was required for accurate volumetric assessment, as proved in physical volume removal tests (Figure 4). With the increase of wear area, the undeformed region will not be enough to reconstruct the initial surface, which will have a great influence on the volumetric assessment. There were some limitations in this study, such as the uncertainty in the actual machining tolerance and plastic deformations generated during physical volume removal tests, which are likely due to the vibration. Furthermore, the clamping and probing forces during the CMM measurement can induce deformations to the polyethylene tibial knee components, which is not visible when comparing the volumetric determination with and without reference; however, this should be

taken into account as an uncertainty contribution and needs further studies. However, the general high levels of agreement indicate that this method is appropriate to measure clinically relevant levels of wear.

4. Conclusions

This paper presented a coordinate-based volumetric wear assessment methodology for polyethylene tibial knee inserts in total knee replacements. In the cases of no prewear data such as CAD models and design drawings provided, the original condyle surface was generated via a 5th-order polynomial curve surface fitting algorithm based on the unworn coordinates obtained using CMM. The influence of scan

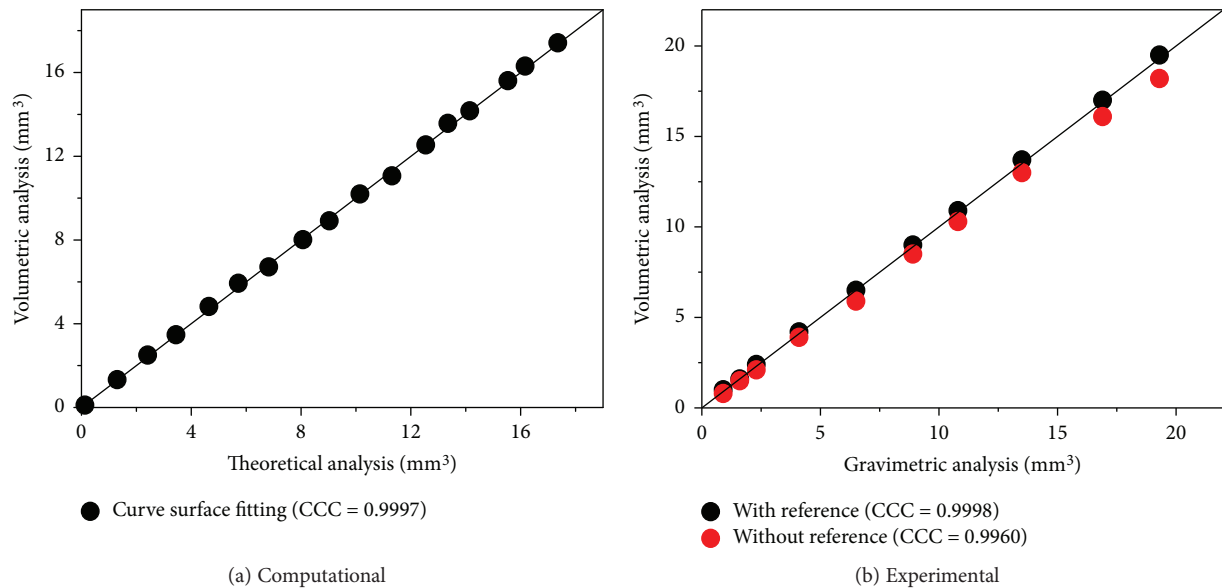


FIGURE 7: Concordance correlation coefficients results of volumetric assessment methodology based on computational and experimental simulated volume removal tests.

interval range from 0.1 mm to 2.0 mm was investigated using an unworn tibial knee component, and the scan interval of 0.2 mm was used in the CMM measurement to balance accuracy and time costs. Both computational and experimental simulated volume removal tests were performed to validate the accuracy of the methodology. For computational simulated volume removal tests, the determined volume loss was very close (maximum error equal to 0.2 mm^3) to the theoretical with concordance correlation coefficients (CCC) of 0.9997. For experimental simulated volume removal tests, the validation results show slightly deviation but still indicated that the methodology is accurate for wear volume assessment (maximum errors equal to 0.2 mm^3 and 1.1 mm^3 , resp.), with CCC of 0.9998 and 0.9960 with and without initial surface geometry, respectively. The presented CMM-based methodology can be used for volumetric assessment and can also be applied to the biotribological study of other polyethylene components, since wear and damage can be assessed visually and volumetrically.

Conflicts of Interest

The authors declare that there is no conflict of interest regarding the publication of this paper.

Acknowledgments

This research is part of Zhongmin Jin's PhD thesis in University of Leeds and was supported by the EPSRC, the Centre of Excellence in Medical Engineering funded by the Wellcome and by the NIHR LMBRU Leeds Musculoskeletal Biomedical Research Unit, the Applied Basic Research Programs of Science and Technology Commission Foundation of Jiangsu Province (BK20150256), and Scientific Research Foundation of Changzhou Institute of Technology (YN1512, YN1626).

References

- [1] G. A. Engh, "Failure of the polyethylene bearing surface of a total knee replacement within four years. A case report," *The Journal of Bone & Joint Surgery*, vol. 70, no. 7, pp. 1093–1096, 1988.
- [2] B. C. Carr and T. Goswami, "Knee implants – review of models and biomechanics," *Materials & Design*, vol. 30, no. 2, pp. 398–413, 2009.
- [3] S. M. Kurtz, *The UHMWPE Handbook*, Academic, Amsterdam, 2004.
- [4] J. Fisher, H. M. McEwen, J. L. Tipper et al., "Wear, debris, and biologic activity of cross-linked polyethylene in the knee: benefits and potential concerns," *Clinical Orthopaedics and Related Research*, vol. 428, pp. 114–119, 2004.
- [5] C. L. Brockett, L. M. Jennings, and J. Fisher, "The wear of fixed and mobile bearing unicompartmental knee replacements," *Proceedings of the Institution of Mechanical Engineers Part H-Journal of Engineering in Medicine*, vol. 225, no. 5, pp. 511–519, 2011.
- [6] P. Bills, L. Blunt, and X. Jiang, "Development of a technique for accurately determining clinical wear in explanted total hip replacements," *Wear*, vol. 263, no. 7–12, pp. 1133–1137, 2007.
- [7] M. G. Teeter, D. D. Naudie, K. D. Charron, and D. W. Holdsworth, "Three-dimensional surface deviation maps for analysis of retrieved polyethylene acetabular liners using micro-computed tomography," *The Journal of Arthroplasty*, vol. 25, no. 2, pp. 330–332, 2010.
- [8] S. Affatato, B. Bordini, C. Fagnano, P. Taddei, A. Tinti, and A. Toni, "Effects of the sterilisation method on the wear of UHMWPE acetabular cups tested in a hip joint simulator," *Biomaterials*, vol. 23, no. 6, pp. 1439–1446, 2002.
- [9] D. D. D'Lima, J. C. Hermida, P. C. Chen, and C. W. Colwell, "Polyethylene cross-linking by two different methods reduces acetabular liner wear in a hip joint wear simulator," *Journal of Orthopaedic Research*, vol. 21, no. 5, pp. 761–766, 2003.

- [10] M. Spinelli, S. Carmignato, S. Affatato, and M. Viceconti, "CMM-based procedure for polyethylene non-congruous uni-compartmental knee prosthesis wear assessment," *Wear*, vol. 267, no. 5-8, pp. 753–756, 2009.
- [11] L. A. Blunt, P. J. Bills, X. Q. Jiang, and G. Chakrabarty, "Improvement in the assessment of wear of total knee replacements using coordinate-measuring machine techniques," *Proceedings of the Institution of Mechanical Engineers, Part H: Journal of Engineering in Medicine*, vol. 222, no. 3, pp. 309–318, 2008.
- [12] S. Affatato, F. Zanini, and S. Carmignato, "Quantification of wear and deformation in different configurations of polyethylene acetabular cups using micro X-ray computed tomography," *Materials*, vol. 10, no. 12, p. 259, 2017.
- [13] O. K. Muratoglu, R. S. Perinchieff, C. R. Bragdon, D. O. O'Connor, R. Konrad, and W. H. Harris, "Metrology to quantify wear and creep of polyethylene tibial knee inserts," *Clinical Orthopaedics and Related Research*, vol. 410, pp. 155–164, 2003.
- [14] W. Jiang, J. Fisher, Z. Jin, K. W. Ruth, and C. L. Brockett, *Wear Measurement of Polyethylene Components in Total Knee Replacement*, [Ph.D. thesis], University of Leeds, 2014.
- [15] R. Y. Liow and D. W. Murray, "Which primary total knee replacement? A review of currently available TKR in the United Kingdom," *Annals The Royal College of Surgeons of England*, vol. 79, pp. 335–340, 1997.
- [16] R. Chakravarty, R. D. Elmallah, J. J. Cherian, S. M. Kurtz, and M. A. Mont, "Polyethylene wear in knee arthroplasty," *The Journal of Knee Surgery*, vol. 28, no. 5, pp. 370–375, 2015.

Research Article

Active Tube-Shaped Actuator with Embedded Square Rod-Shaped Ionic Polymer-Metal Composites for Robotic-Assisted Manipulation

Yanjie Wang¹, Jiayu Liu,² Denglin Zhu,¹ and Hualing Chen³

¹School of Mechanical and Electrical Engineering, Hohai University, Changzhou Campus, Changzhou 213022, China

²Department of Mechanical Engineering, Johns Hopkins University, Baltimore, MD 21218, USA

³School of Mechanical Engineering, Xi'an Jiaotong University, Xi'an 710049, China

Correspondence should be addressed to Yanjie Wang; yjwang@hhu.edu.cn

Received 3 November 2017; Revised 9 January 2018; Accepted 15 February 2018; Published 25 March 2018

Academic Editor: QingSong He

Copyright © 2018 Yanjie Wang et al. This is an open access article distributed under the Creative Commons Attribution License, which permits unrestricted use, distribution, and reproduction in any medium, provided the original work is properly cited.

This paper reports a new technique involving the design, fabrication, and characterization of an ionic polymer-metal composite (IPMC-) embedded active tube, which can achieve multidegree-of-freedom (MODF) bending motions desirable in many applications, such as a manipulator and an active catheter. However, traditional strip-type IPMC actuators are limited in only being able to generate 1-dimensional bending motion. So, in this paper, we try to develop an approach which involves molding or integrating rod-shaped IPMC actuators into a soft silicone rubber structure to create an active tube. We modified the Nafion solution casting method and developed a complete sequence of a fabrication process for rod-shaped IPMCs with square cross sections and four insulated electrodes on the surface. The silicone gel was cured at a suitable temperature to form a flexible tube using molds fabricated by 3D printing technology. By applying differential voltages to the four electrodes of each IPMC rod-shaped actuator, MDOF bending motions of the active tube can be generated. Experimental results show that such IPMC-embedded tube designs can be used for developing robotic-assisted manipulation.

1. Introduction

In recent years, electroactive polymers (EAPs) have been studied in many engineering fields, such as artificial muscles, biomimetic robots, dynamic sensors, and energy harvesters. Ionic polymer-metal composite (IPMC) is considered to be one of the most promising types of EAPs because of its unique advantages including flexibility, large deformation under low driving voltage, and biocompatibility. Application to an electric field causes cations to move toward the cathode with water molecules inside IPMC, thus introducing swelling in the cathode side and shrinking in the anode side, which leads to a bending motion toward the anode [1–3]. Recently, IPMC has been considered for many applications, such as underwater biomimetic robotics [4–9] and energy harvesting devices [10–13].

A traditional strip-type IPMC consists of an ion exchange membrane, typically Nafion (DuPont) membranes

with thickness of less than 300 μm , and two thin noble metallic electrodes chemically and physically deposited on the surfaces of the membrane. When an electric field is applied, the actuation mode of a strip IPMC generates 1-dimensional bending toward the anode. An extensive study has been conducted in improving the performance of IPMCs [14], including the development of novel ionic polymer membranes through a polymer blending method and nanocomposite membranes [15–23], the replacement of traditional metallic electrodes by nonmetal electrodes such as carbon nanotube-based electrodes [24, 25], and the optimization of the electrode interface [26], increasing the thickness of Nafion membranes through a solution casting method and a hot pressing technique [27, 28]. Although the performance of IPMCs has been improved, the 1-dimensional bending motion of traditional strip-type IPMCs limits its applications. Many researchers have tried to make IPMC biaxial bending actuators capable of

multidegree-of-freedom bending motions. Shahinpoor and Kim proposed the concept of an IPMC biaxial bending actuator in a square rod form [29]. Lee et al. presented platinum-electrode biaxial bending IPMCs based on hot pressing of Nafion films [30]. Cylindrical and tubular platinum-electrode IPMCs based on a hot press process and an extrusion process have also been developed [31–34].

With the development of IPMCs with nontraditional shapes, more promising applications have been proposed and achieved in the biomedical field. Lee et al. presented a helical IPMC actuator for radius control of biomedical active stents [35]. Nguyen et al. developed a flap valve IPMC micro-pump with a flexible supported diaphragm [36]. Li et al. proposed the application of IPMC-based artificial muscle to the myoelectric hand prosthesis [37]. Yoon et al. reported the development of a low-cost active tip bending system actuated by a strip IPMC actuator at the tip for a scanning fiber endoscope [38]. Moreover, an active catheter or active guide wire systems for biomedical applications based on IPMC actuators have received much attention recently. Strip-type IPMC actuators were attached on the front to serve as the servo actuator to bend the catheter for biomedical applications such as active catheters in bifurcated blood vessels [39–41]. However, the resulting motion is only 1-dimensional bending motion perpendicular to the electrodes of the strip-type IPMC actuator. Rod-shaped or tubular IPMC actuators with outer diameter less than 2 mm have also been successfully developed for biomedical applications in intravascular procedures [14, 31–33, 42]. Rod-shaped and tubular IPMCs with four separated electrodes on the surfaces can bend to multiple directions.

Nowadays, robotic-assisted manipulation has become increasingly popular because of numerous benefits compared with conventional surgical procedures, typically such as minimally invasive surgery (MIS). The most common robotic system currently used in the MIS procedures involves using master-slave systems, such as Da Vinci systems, and the multidegree-of-freedom surgical instrument actuated by cable-driven antagonist actuations [43, 44]. Recently, some new alternative mechanisms have been introduced, including electromagnetic drives and hydraulic/pneumatic actuators [45–47]. Unfortunately, these types of MIS robotics have some limitations of their own, such as bulky size, high stiffness, and structural complexity. We herein propose a novel structure which involves molding or integrating IPMC rod-type actuators into a soft silicone rubber material to create an active tube that can be used to realize multidegree-of-freedom bending motions. Compared with existing technologies in robotic-assisted manipulation, the proposed smart active tube offers some advantages in that it can reduce damage to a minimum due to the softness of the structure. The bending motion of the tube could be controlled to reach the desired location, while surgical instruments could be used during surgery through the hole of the active tube.

Figure 1 shows the conceptual design of the proposed active tube-shaped actuator with embedded square rod-shaped IPMC. The main contribution of this work is the design, fabrication, and performance characterization of the

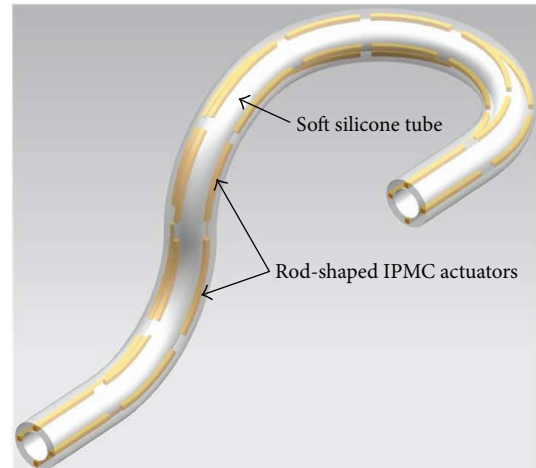


FIGURE 1: A conceptual appearance of the proposed rod-shaped IPMC-embedded tube actuator.

newly created prototype of the IPMC-embedded multidegree-of-freedom bending tube structure. The rod-shaped IPMCs were fabricated by Nafion solution casting and deposition of palladium-gold electrodes. The soft silicone elastomer tube structure was cured in molds fabricated by 3D printing technology. The fabricated rod-shaped IPMCs with dimension of $25\text{ mm} \times 1\text{ mm} \times 1\text{ mm}$ (length \times width \times thickness) were then integrated to the tube structure. We conducted experiments to investigate the multidegree-of-freedom actuation performance, strain energy density, and efficiency of the IPMC-embedded tube actuator. This paper is organized as follows. First, the fabrication process of the rod-shaped IPMCs is developed. Next, the design and fabrication of the rod-shaped IPMC-embedded active tube actuator are presented. After that, experimental results are reported, and strain energy density and efficiency are evaluated. Concluding remarks are presented in the final section.

2. Fabrication Process

2.1. Rod-Shaped IPMC Actuator. In this research, palladium-electrode rod-shaped IPMC actuators with square cross section were fabricated in house based on the solution casting method, and gold was electroplated on top of the palladium electrode to enhance the performance of rod-shaped IPMCs. First, we used Nafion PFSA polymer dispersions (DE 520CS, DuPont) to make a 1 mm thick Nafion film from the solution casting method [26, 27]. Ethylene glycol was added into the Nafion solution to avoid forming cracks during the solution casting process. Then, we cut the plate into Nafion rods with square cross section $1\text{ mm} \times 1\text{ mm}$. For the detailed description, refer to [48].

After fabricating the Nafion polymer beams with square cross section, an impregnation-reduction process and an electroless palladium plating process were applied to create the metal electrodes on the surface of the fabricated Nafion beams. The preparation process was as follows [49]. First, the Nafion beams were sandblasted to roughen the surface

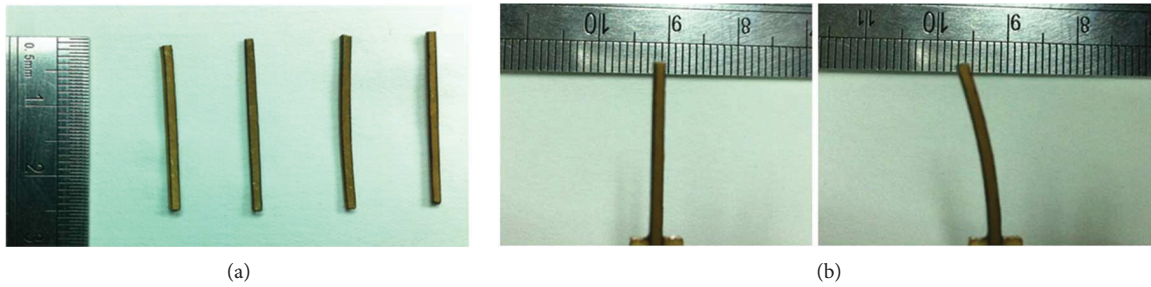


FIGURE 2: Fabricated rod-shaped IPMC actuators: (a) real optical image; (b) actuation exhibition.

and treated with 3% H_2O_2 and 1 mol/l HCl to remove impurities from the beams. Afterwards, the impregnation-reduction process was applied to enable the Nafion beam to absorb enough palladium complex ions $\text{Pd}(\text{NH}_3)_4^{2+}$ which will be reduced to palladium particles that penetrate deep into the Nafion beam. The Nafion beams were immersed in $\text{Pd}(\text{NH}_3)_4^{2+}$ solution (0.1 mol/l) for several hours to allow the Nafion beams to absorb the palladium complex ions sufficiently. The reduction process took place in NaBH_4 solution (0.85 g/l) as the reduction agent to form electrodes on all six surfaces of the Nafion beam. The impregnation-reduction process was repeated for more than 6 times to increase the penetration of palladium particles into the Nafion beams because Nafion beams are thicker than the typical Nafion membranes. Then, the electroless palladium plating process was performed to further create metal electrodes to reduce the resistance of the surface electrodes. The mixed solution of hydrazine hydrate and $\text{Pd}(\text{NH}_3)_4^{2+}$ was used to deposit more palladium metal on the surface to form a thicker palladium electrode layer. The electroless palladium plating process was repeated 3 times to achieve multiple layers of palladium on all surfaces of the Nafion beams.

The electroplating process was then performed by using gold complexes in order to further improve the electrode conductivity without increasing the stiffness significantly. Over time, the performance degradation of the IPMC actuators can occur with an increase in surface (electrode) resistance due to cracks or voids from high levels of actuation or dehydration. Electroplating of gold on the palladium electrodes can fill the cracks and voids and thus can reduce the surface resistivity and maintain the actuation performance [7]. For newly fabricated rod-shaped IPMCs with palladium electrodes, the electrode resistance on the four surfaces is 12.7Ω and 1.1Ω (measured by the two farthest points) before and after the gold electroplating process, separately. In the final step, the four longitudinal edges are insulated by a scalpel and the two ends of the fabricated rod-shaped IPMCs were removed to form 4 separate electrodes on the surface of the Nafion beams. The type of mobile ions inside the IPMCs is sodium ions, with water as solvent.

Figure 2(a) shows the real optical image of rod-shaped IPMC actuators of $1 \text{ mm} \times 1 \text{ mm} \times 25 \text{ mm}$. It can be seen from Figure 2 that the Au electrode is deposited uniformly on the copolymer surface with the above fabrication process. To confirm the thickness of copolymer and electrodes,

Figure 3 shows the SEM images of the cross section. From Figure 3, it is clearly shown that a Pd electrode layer with a thickness of approximately $100 \mu\text{m}$ was formed. Notably, Pd grains penetrate deep into the Nafion copolymer, and there is no clear interface observed between the Pd grains and Nafion copolymer, which indicates that the electrodes adhere very well with the copolymer. The thick metal electrode layer with excellent adhesion should decrease the surface resistance, increase the current of an IPMC, and enhance the actuation deformation and blocking force. Figure 2(b) shows the actuation exhibition of a rod-shaped IPMC actuator.

2.2. Soft Silicone Sleeve. Figure 4 illustrates the concept of embedding rod-shaped IPMC actuators into a soft tube to create a smart active tube capable of multidegree-of-freedom bending motions. In this research, four rod-shaped IPMC actuators are incorporated into the tube structure to control multidegree-of-freedom bending motions of the overall active tube. Further, more rod-shaped IPMC actuators could be implemented to improve the performance of the active tube actuator. The dimension of the tube structure was outer diameter (10.5 mm) \times inner diameter (8.5 mm) \times length (20 mm), designed to house four rod-shaped IPMC actuators with square cross section ($1 \text{ mm} \times 1 \text{ mm} \times 25 \text{ mm}$). The length of the rod-shaped IPMC actuators is fabricated to be larger than the length of the tube structure to facilitate the connection between the IPMCs and the experimental setup. In order to decrease the stiffness of the silicone tube and improve the actuation performance, the tube is designed to have a final thickness of 0.7 mm over the rod-shaped IPMCs and a thickness of 1 mm between the bumps to house the IPMC actuators.

After fabricating rod-shaped IPMC actuators, a mold for the tube structure was fabricated by 3D printing technology using a stereolithography apparatus (SCPS350B, XJRP). The mold was designed to fabricate the silicone rubber tube (outer diameter (10.5 mm), inner diameter (8.5 mm), and length (20 mm)) with four cavities ($1 \text{ mm} \times 1 \text{ mm} \times 20 \text{ mm}$) that can house four rod-shaped IPMCs, as shown in Figure 5. Four bumps with the dimension of $2.4 \text{ mm} \times 2.4 \text{ mm}$ at every 90° of the silicone rubber tube were designed to house the rod-shaped IPMCs.

Silicone casting rubber TC5005 A/B-C (BJB Enterprises Inc., USA) was used to fill the mold to make a flexible tube for the rod-shaped IPMCs. The modulus of the silicone

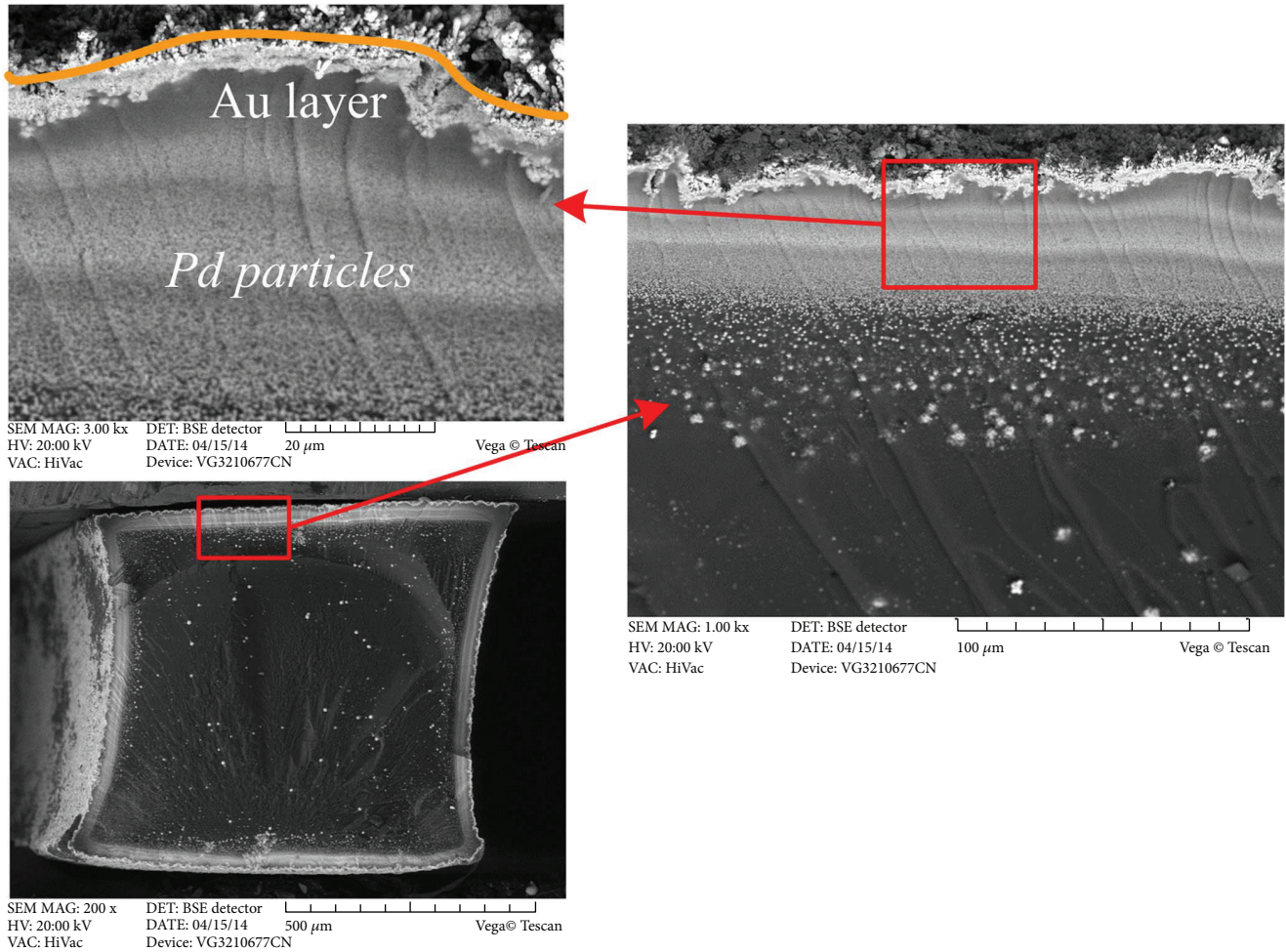


FIGURE 3: Cross-sectional morphology of rod-shaped IPMCs with palladium-gold electrodes.

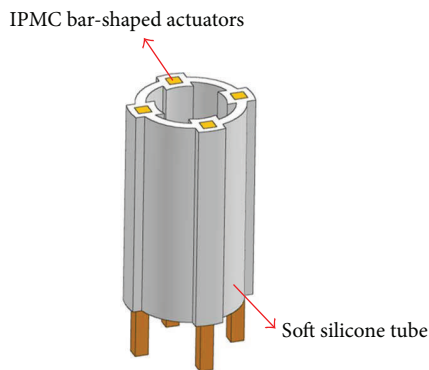


FIGURE 4: Rod-shaped IPMC-embedded multidegree-of-freedom bending tube actuator.

elastomer can be controlled through different mixing ratios between the base silicone and the catalyst. In this research, the mixing ratio was chosen to be one part of catalyst per 10 parts of silicone, as indicated by the manufacturer. The mold fabricated by 3D printing technology was first sprayed with a mold release agent. Then, the mixed silicone gel was poured into the mold and allowed to cure at room temperature for 24 h. Next, the mold was removed leaving the silicone

rubber tube with 4 cavities to insert rod-shaped IPMCs. Four rod-shaped IPMC actuators were then integrated into the silicone rubber tube to complete the IPMC-embedded active control tube (Figure 6).

2.3. Motion Analysis of Rod IPMC and IPMC-Embedded Active Tube. The applied voltages to the four electrode surfaces of a rod-shaped IPMC could be independently controlled. Thus, a rod-shaped IPMC actuator is capable of bending to eight directions including the vertical/horizontal directions and the diagonal directions (Figure 7(a)). To actuate a rod-shaped IPMC in the vertical/horizontal directions, one positive signal was applied to the corresponding electrode. Positive signals were simultaneously applied to adjacent electrodes to actuate rod-shaped IPMC actuators in the diagonal directions. Thus, by controlling the voltages applied to the four electrodes of each rod-shaped IPMC actuator, the bending motions of four inserted rod-shaped IPMC actuators can be independently controlled, causing the multidegree-of-freedom bending motions of the overall active tube structure (Figure 7(b)).

2.4. Experimental Setup. In order to independently apply electric signals to the four electrodes of each rod-shaped

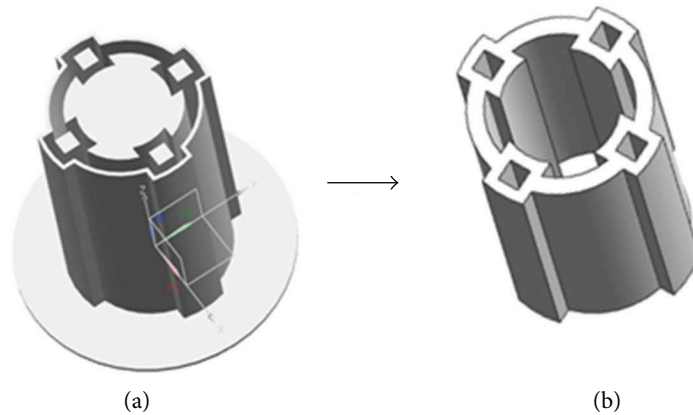


FIGURE 5: (a) The mold fabricated by 3D printing technology for the silicone rubber tube. (b) Soft silicone tube to house 4 rod-shaped IPMC actuators.

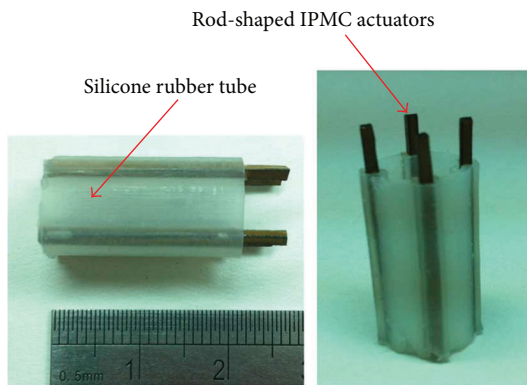


FIGURE 6: Fabricated rod-shaped IPMC-embedded active tube actuator.

IPMC actuator, a custom clamp is created to maintain good electrical contact between the metallized surfaces of the IPMCs and the electrodes of the clamp. As shown in Figure 8, four silicone tubes were inserted into the base fabricated by 3D printing technology. Sixteen pieces of trimmed copper sheets were attached to the silicone tubes as the electrical pads to apply electric signals to the four electrodes of each rod-shaped IPMC actuator. Sixteen wires are individually soldered to the copper sheets for transmitting electrical signals to the device. The active tube actuator embedded with four rod-shaped IPMCs was then inserted into the clamp. A PC equipped with LabVIEW software and a power supply applies the necessary controlled activation signals to the overall sixteen electrodes of four rod-shaped IPMCs through copper sheets. The bending deflection and blocking force of the fabricated IPMC-embedded tube actuator were measured at the tip using a laser displacement sensor (Model Keyence LK-G80) and a force sensor (Model Keyence GSO-10).

3. Results and Discussions

3.1. Tip Deformation and Current Characterization of the Active Tube Actuator. The bending deformation of the active tube actuator in the vertical/horizontal direction and

diagonal direction was measured at the tip of the tube using a laser displacement sensor. The current of rod-shaped IPMCs was simultaneously measured and recorded. The four rod-shaped IPMCs were actuated at 0.2 Hz with both sine and square wave input signals of 0.5 V–2.0 V with the interval of 0.5 V, respectively.

First, the active tube bending deformation in the vertical/horizontal direction was measured. In order to actuate the IPMC-embedded tube actuator in the vertical/horizontal directions, the same input signal with the same phase was applied to the corresponding electrodes of all four rod-shaped IPMCs (see Figure 7(b)). The tip bending responses of the active tube actuator when sine and square wave input signals of 0.5 V, 1.0 V, 1.5 V, and 2.0 V at 0.2 Hz were applied are shown in Figure 9. As the driving voltage increases, the bending deformation of the active tube actuator increases. The experimental data reveals that the tip bending deformation under square input signal is larger compared to that under sine wave input signal. This is expected as the largest tip bending deformation in the vertical/horizontal direction is 0.53 mm under 2.0 V square wave input at 0.2 Hz. The responses exhibit a good repeatability under periodic electrical inputs. Figures 9(c) and 9(d) show the current responses of the active tube actuator.

From the relation between tip bending deformation in the vertical/horizontal directions and applied voltages (Figure 10), we can also observe that the bending deformation of the active tube actuator does not increase linearly with the driving voltage. This is because the actuation of IPMCs is induced by the migration of cations with water molecules from anode to cathode inside the material. When the applied voltage increases, much more cations can move along with water molecules inside the IPMCs, thus generating a larger bending deformation of the entire tube structure. In fact, a larger increment of bending deformation can be achieved each time we increase the driving voltage by an interval of 0.5 V from 0.5 V to 2.0 V. Much larger bending deformations can be generated by applying higher voltages. However, electrolysis due to high driving voltages should be taken into account to ensure stable actuation performance.

Next, the bending deformation of the active tube actuator in the diagonal direction is generated by simultaneously

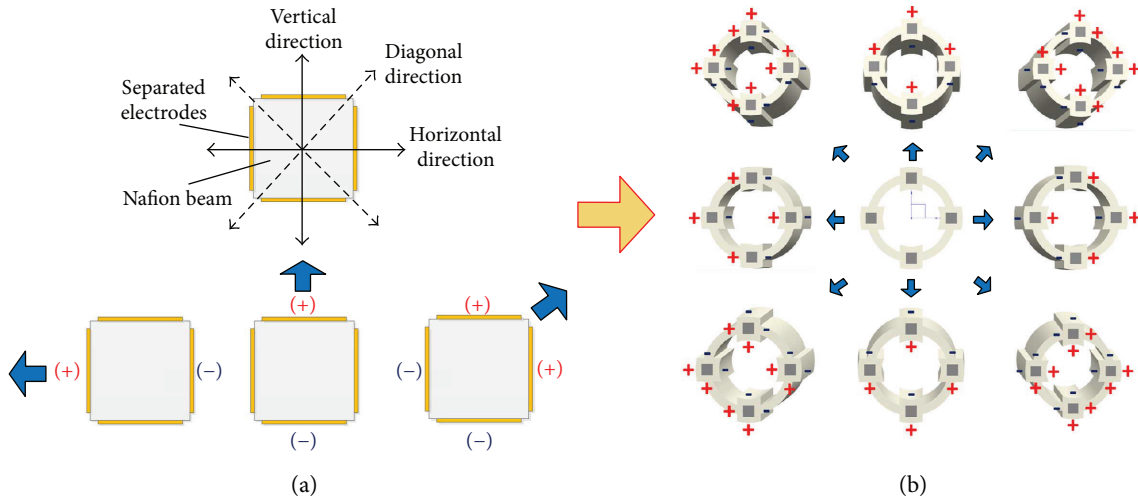


FIGURE 7: Actuation modes of (a) rod-shaped IPMC and (b) IPMC-embedded tube in the vertical/horizontal directions and diagonal directions.

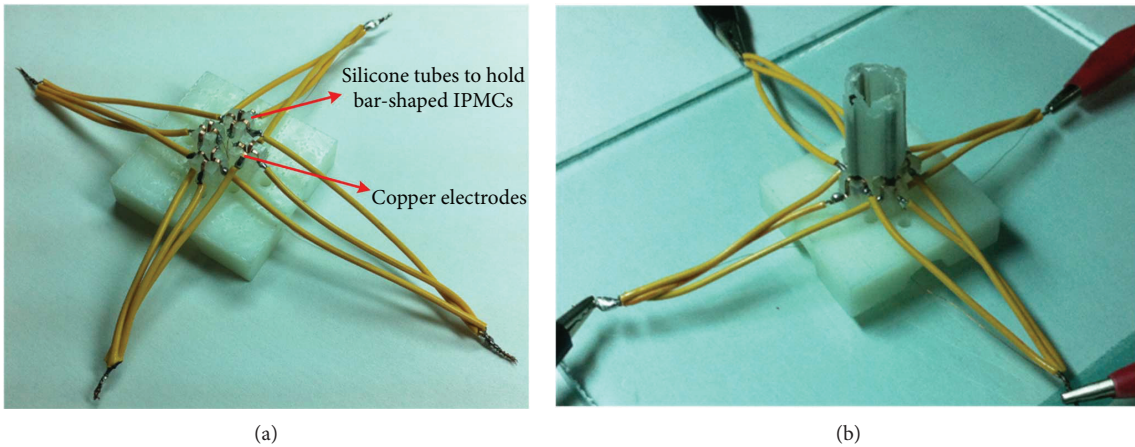


FIGURE 8: (a) Experimental setup for the IPMC-embedded tube actuator. (b) The assembly ready for measurement. Due to space constraints, fine copper wire is used for the fourth conductive wires inside the active tube.

applying the same input to the corresponding adjacent electrodes of each rod-shaped IPMC actuator (Figure 7(b)). The same levels of the above sine and square wave signals were applied to actuate the four rod-shaped IPMCs. Figure 11 illustrates the tip bending deformation in the diagonal directions of the active tube actuator under different input signals. The same trend was observed that utilizing a square input signal generates a larger bending response compared to the sine input signal. The tip bending deformation of the tube actuator in the diagonal direction was smaller than that in the vertical/horizontal direction under the same input signal. The largest tip bending deformation in the diagonal direction is approximately 0.4 mm under 2.0 V square wave input at 0.2 Hz.

It should be noted that, although the tip bending deformation of the tube actuator in the diagonal direction was smaller than that in the vertical/horizontal direction under the square input signal, the current responses of IPMCs show the opposite trend. By comparing Figure 9(c)

with Figure 11(c), we find that the actuation current in the diagonal direction was larger than that in the vertical/horizontal direction under the square input signal. This is due to the fact that in the diagonal direction, the electric field strength between the adjacent anode and cathode is higher than that between two opposite outer electrodes of rod-shaped IPMCs in the vertical/horizontal direction. This in turn causes higher charge density near the electrodes and therefore higher actuation current. However, the bending stiffness of rod-shaped IPMCs in the diagonal direction is larger than that in the vertical/horizontal direction. Thus, although the actuation current in the diagonal direction is larger, the bending deformation of the tube structure in the diagonal direction is smaller than that in the vertical/horizontal direction. In addition, for Figure 11(d), the current data under square input signal of 2.0 V has over-range. The peak current is due to the charging process of IPMC. Since the acquisition circuit of the maximum current we designed is 0.5 A, the data above 0.5 A cannot be obtained.

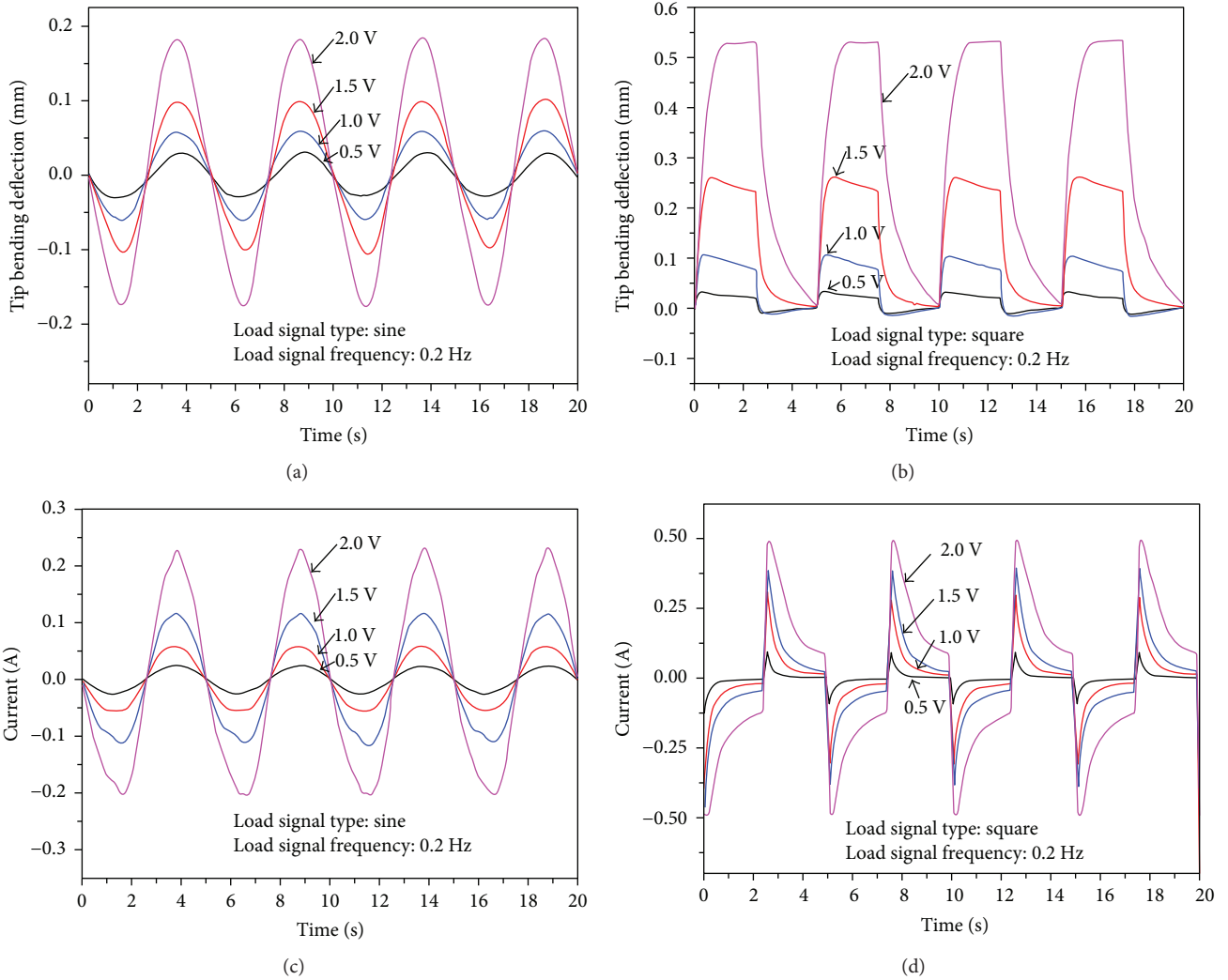


FIGURE 9: Experimental results in the vertical/horizontal directions: (a) tip deformation under sine input signals, (b) tip deformation under square input signals, (c) current responses under sine input signals, and (d) current responses under square input signals.

But from the present data, the current responses at different voltages have clearly shown an approximately linear trend.

3.2. Tip Blocking Force Characterization of the Tube Actuator.

A lightweight cap fabricated by 3D printing technology was put on top of the active tube actuator so that the blocking force of the entire tube actuator could be measured and the actuation performance of the tube actuator would not be affected (Figure 12). The bending force of the active tube in the vertical/horizontal direction and the diagonal direction was measured at the tip using a load cell. The same actuation scheme as aforementioned was used to actuate the tube actuator in the vertical/horizontal directions and the diagonal directions.

For the tip bending force of the tube actuator in the vertical/horizontal directions, 0.2 Hz 0.5 V–2.0 V sine and square wave input signals were applied to the four rod-shaped IPMCs (Figure 13). The tip bending force of the active tube actuator increases with the driving voltages, and the tip bending force under square input signals is larger than

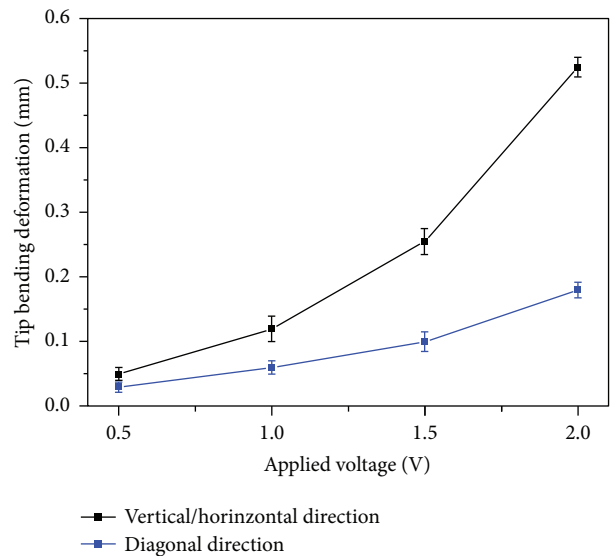


FIGURE 10: Tip bending deformation in the vertical/horizontal directions under 0.2 Hz actuation.

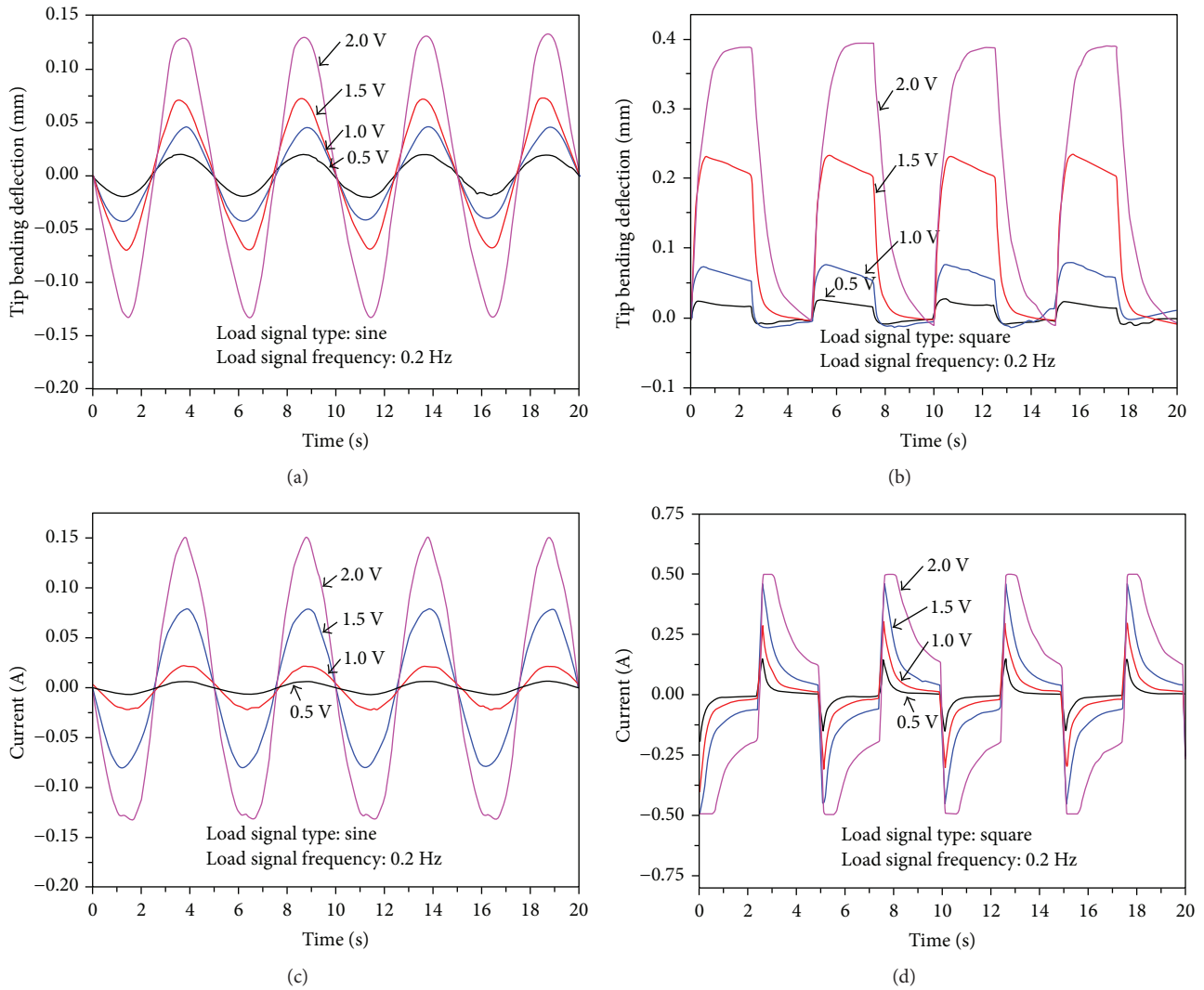


FIGURE 11: Experimental results in the diagonal directions: (a) tip deformation under sine input signals, (b) tip deformation under square input signals, (c) current responses under sine input signals, and (d) current responses under square input signals.

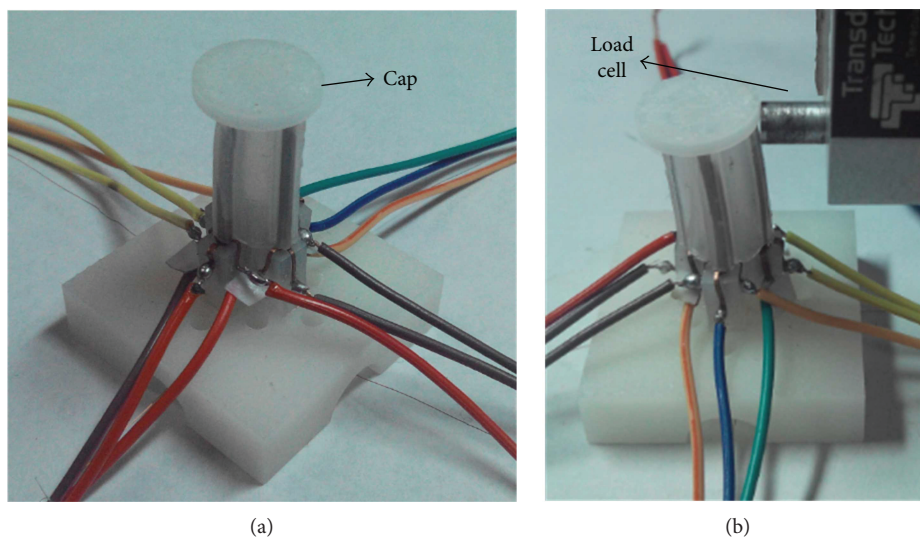


FIGURE 12: Experimental setup for measuring tip bending force of the IPMC-embedded tube actuator.

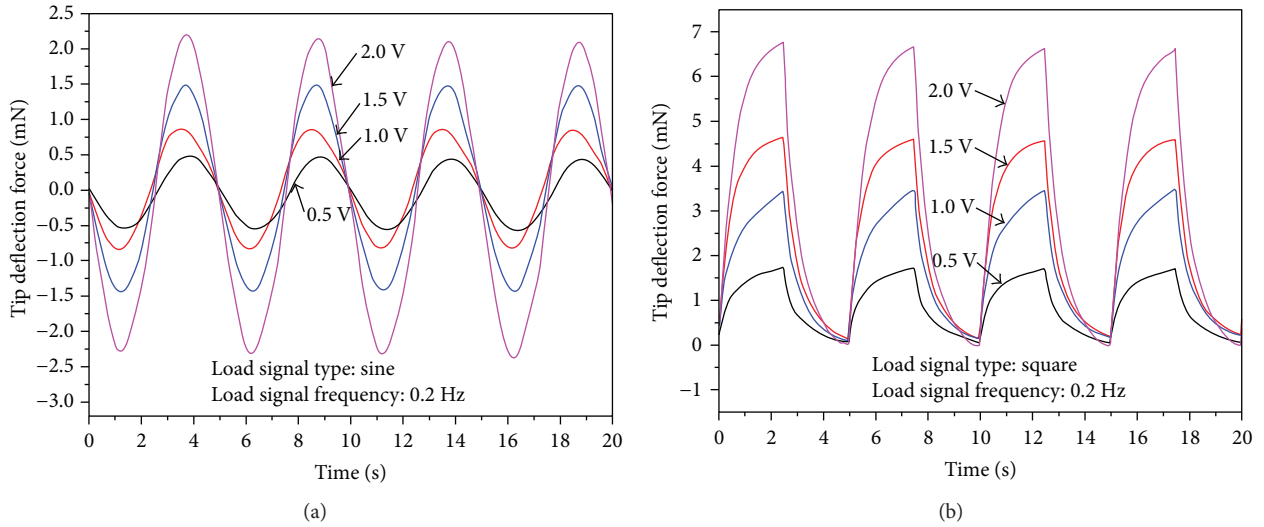


FIGURE 13: Measured tip bending force in the vertical/horizontal directions under (a) sine input signals and (b) square input signals.

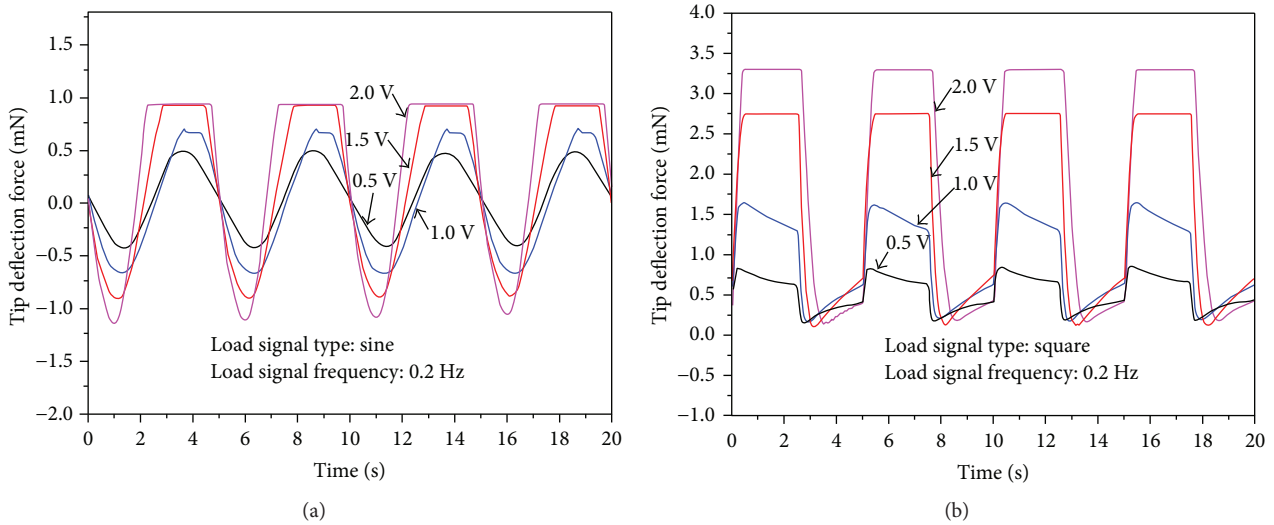


FIGURE 14: Measured tip bending force in the diagonal direction under (a) sine input signals and (b) square input signals.

that under sine input signal. The largest tip bending force in the vertical/horizontal directions is 6.9 mN under 0.2 Hz 2.0 V square wave input signal.

Figure 14 shows the tip bending forces in the diagonal direction for the tube actuator under 0.2 Hz 0.5 V–2.0 V sine and square input signals. From Figure 14, tip force data of cases 1.5 V and 2.0 V both have overrange at the diagonal direction. This is related to our initial setup. It is well known that the force response of IPMC is hard to measure. In order to measure the force response of the active tube, we design a plastic cap to cover the top of the tube. When the test begins, that cap gives the force sensor a prestress (Figure 12(a)). With the application of alternating voltage, the tube with the cap touches or leaves the force sensor inevitably. When the cap leaves the force sensor, the force response cannot be obtained as shown in Figure 14. If the prestress is too large, force response data will be inaccurate. We used a smaller prestress in the experiments so that overrange is inevitable.

Even so, it is conceivable that all data of four cases show a sinusoidal form. The offset and irregular phenomenon is due to the effect of electrodes in the diagonal direction and the silicone tube. The tip bending force of the tube actuator in the diagonal direction was smaller than that in the vertical/horizontal direction under the same input signal. Additionally, for the sine driving signals with amplitudes higher than 1.0 V, the maximum tip bending force in the diagonal direction was not reached (Figure 14(a)). This is because the cap on top of the tube actuator was initially pushed in touch with the load cell before measurement (Figure 12). When the tube bends toward the load cell, the tip bending force of the active tube could be accurately measured (negative force values). When the tube bends away from the load cell, the tip bending force could not be measured after the tip leaves the load cell (positive force values). Therefore, we can observe that for driving signals with amplitudes higher than 1.0 V, the negative force values have

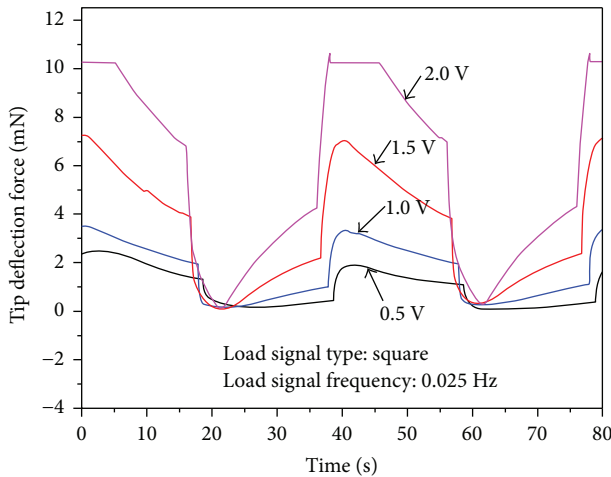


FIGURE 15: Measured tip bending force in the vertical/horizontal directions under 0.025 Hz square input signals.

reached the maximum, but the positive force values have not reached the maximum. The same phenomenon could be observed for tip bending force in the diagonal direction under square wave signals in Figure 14(b).

Another observation is that the tip bending forces in the vertical/horizontal direction under 0.2 Hz 0.5 V–2.0 V square wave input signals have not reached the maximum values that could be achieved with such driving voltages (Figure 13(b)). The tip bending forces were still increasing and have not reached their maximum values when the driving voltage started to decrease and the tube started to bend toward the opposite direction. Thus, the tip bending forces of the tube actuator in the vertical/horizontal direction were measured under 0.025 Hz 0.5 V–2.0 V square wave input signals (Figure 15). The resulting tip bending forces in the vertical/horizontal direction reach the maximum values, and the largest tip bending force reaches up to 10.4 mN under 0.025 Hz 2.0 V square wave signal. The same problem arises that the force values could not reach the maximum for the 0.025 Hz 2.0 V square input due to the initial pressure between the cap and the load cell. The present result also shows that the tip bending force of the IPMC-embedded tube actuator was not able to maintain the maximum value and gradually declined. These experimental data suggest that the relaxation back phenomenon that appears in flat-type IPMC actuators can occur in the step responses of the rod-shaped IPMC actuators.

4. Conclusions

This paper explored the approach to embed rod-shaped IPMC actuators into a soft tube structure to create an active tube capable of multidegree-of-freedom bending motions. The Nafion solution casting method was modified, and a complete sequence of the fabrication process was developed for rod-shaped IPMCs with square cross sections. Four rod-shaped IPMCs were incorporated into the soft tube fabricated based on 3D printing technology to create the active tube actuator. For the IPMC-embedded tube with

dimensions of OD (10.5 mm) \times ID (8.5 mm) \times L (20 mm), the measured maximum tip bending deformation in the vertical/horizontal direction and the diagonal direction was approximately 0.53 mm and 0.4 mm under 0.2 Hz 2.0 V square wave actuation, and the corresponding tip bending force could reach up to 10.4 mN and 3.38 mN. These results suggest that such active tube structures have a potential to be used for minimally invasive surgery applications.

Conflicts of Interest

The authors declared no potential conflicts of interest with respect to the research, authorship, and/or publication of this article.

Acknowledgments

This work was supported by the National Natural Science Foundation of China (51505369, 91748124, and 51290294), Basic Research Program of Changzhou City (CJ20179050), the Foundation of Jiangsu Key Laboratory of Special Robot Technology (2017B21114), and the Fundamental Research Funds for the Central Universities, China (2016B02814). The authors gratefully acknowledge the supports.

References

- [1] G. Del Bufalo, L. Placidi, and M. Porfiri, "A mixture theory framework for modeling the mechanical actuation of ionic polymer metal composites," *Smart Materials and Structures*, vol. 17, no. 4, article 045010, 2008.
- [2] M. Porfiri, "Charge dynamics in ionic polymer metal composites," *Journal of Applied Physics*, vol. 104, no. 10, article 104915, 2008.
- [3] R. Tiwari and E. Garcia, "The state of understanding of ionic polymer metal composite architecture: a review," *Smart Materials and Structures*, vol. 20, no. 8, article 083001, 2011.
- [4] Z. Chen, S. Shatara, and X. Tan, "Modeling of biomimetic robotic fish propelled by an ionic polymer–metal composite caudal fin," *IEEE/ASME Transactions on Mechatronics*, vol. 15, no. 3, pp. 448–459, 2010.
- [5] Q. Shen, T. Wang, J. Liang, and L. Wen, "Hydrodynamic performance of a biomimetic robotic swimmer actuated by ionic polymer–metal composite," *Smart Materials and Structures*, vol. 22, no. 7, article 075035, 2013.
- [6] L. Wen and G. Lauder, "Understanding undulatory locomotion in fishes using an inertia-compensated flapping foil robotic device," *Bioinspiration & Biomimetics*, vol. 8, no. 4, article 046013, 2013.
- [7] V. Palmre, J. J. Hubbard, M. Fleming et al., "An IPMC-enabled bio-inspired bending/twisting fin for underwater applications," *Smart Materials and Structures*, vol. 22, no. 1, article 014003, 2012.
- [8] M. Yamakita, A. Sera, N. Kamamichi, K. Asaka, and Z.-W. Luo, "Integrated design of IPMC actuator/sensor," in *Proceedings 2006 IEEE International Conference on Robotics and Automation, 2006. ICRA 2006*, pp. 1834–1839, Orlando, FL, USA, May 2006.
- [9] W. Yim, J. Lee, and K. J. Kim, "An artificial muscle actuator for biomimetic underwater propulsors," *Bioinspiration & Biomimetics*, vol. 2, no. 2, pp. S31–S41, 2007.

- [10] Q. Shen, T. Wang, and K. J. Kim, "A biomimetic underwater vehicle actuated by waves with ionic polymer-metal composite soft sensors," *Bioinspiration & Biomimetics*, vol. 10, no. 5, article 055007, 2015.
- [11] M. Aureli, C. Prince, M. Porfiri, and S. D. Peterson, "Energy harvesting from base excitation of ionic polymer metal composites in fluid environments," *Smart Materials and Structures*, vol. 19, no. 1, article 015003, 2009.
- [12] J. Brufau-Penella, M. Puig-Vidal, P. Giannone, S. Graziani, and S. Strazzeri, "Characterization of the harvesting capabilities of an ionic polymer metal composite device," *Smart Materials and Structures*, vol. 17, no. 1, article 015009, 2007.
- [13] R. Tiwari, K. J. Kim, and S. M. Kim, "Ionic polymer-metal composite as energy harvesters," *Smart Structures and Systems*, vol. 4, no. 5, pp. 549–563, 2008.
- [14] C. Jo, D. Pugal, I. K. Oh, K. J. Kim, and K. Asaka, "Recent advances in ionic polymer-metal composite actuators and their modeling and applications," *Progress in Polymer Science*, vol. 38, no. 7, pp. 1037–1066, 2013.
- [15] Q. He, M. Yu, X. Yang, K. J. Kim, and Z. Dai, "An ionic electroactive actuator made with graphene film electrode, chitosan and ionic liquid," *Smart Materials and Structures*, vol. 24, no. 6, article 065026, 2015.
- [16] D. J. Guo, H. T. Ding, H. Wei, Q. He, M. Yu, and Z. D. Dai, "Hybrids perfluorosulfonic acid ionomer and silicon oxide membrane for application in ion-exchange polymer-metal composite actuators," *Science in China Series E: Technological Sciences*, vol. 52, no. 10, pp. 3061–3070, 2009.
- [17] M. Yu, Q. S. He, Y. Ding, D. J. Guo, J. B. Li, and Z. D. Dai, "Force optimization of ionic polymer metal composite actuators by an orthogonal array method," *Chinese Science Bulletin*, vol. 56, no. 19, pp. 2061–2070, 2011.
- [18] Q. He, X. Yang, Z. Wang et al., "Advanced electro-active dry adhesive actuated by an artificial muscle constructed from an ionic polymer metal composite reinforced with nitrogen-doped carbon nanocages," *Journal of Bionic Engineering*, vol. 14, no. 3, pp. 567–578, 2017.
- [19] S. H. Kim, K. W. Oh, and J. H. Choi, "Preparation and self-assembly of polyaniline nanorods and their application as electroactive actuators," *Journal of Applied Polymer Science*, vol. 116, no. 5, pp. 2601–2609, 2010.
- [20] S. J. Kim, M. S. Kim, S. R. Shin et al., "Enhancement of the electromechanical behavior of IPMCs based on chitosan/polyaniline ion exchange membranes fabricated by freeze-drying," *Smart Materials and Structures*, vol. 14, no. 5, pp. 889–894, 2005.
- [21] B. J. Landi, R. P. Raffaella, M. J. Heben, J. L. Alleman, W. VanDerveer, and T. Gennett, "Development and characterization of single wall carbon nanotube-Nafion composite actuators," *Materials Science and Engineering: B*, vol. 116, no. 3, pp. 359–362, 2005.
- [22] D. Y. Lee, I. S. Park, M. H. Lee, K. J. Kim, and S. Heo, "Ionic polymer-metal composite bending actuator loaded with multi-walled carbon nanotubes," *Sensors and Actuators A: Physical*, vol. 133, no. 1, pp. 117–127, 2007.
- [23] I. K. Oh and J. Y. Jung, "Biomimetic nano-composite actuators based on carbon nanotubes and ionic polymers," *Journal of Intelligent Material Systems and Structures*, vol. 19, no. 3, pp. 305–311, 2007.
- [24] S. Liu, Y. Liu, H. Cebeci et al., "High electromechanical response of ionic polymer actuators with controlled-morphology aligned carbon nanotube/Nafion nanocomposite electrodes," *Advanced Functional Materials*, vol. 20, no. 19, pp. 3266–3271, 2010.
- [25] W. Yang, H. Choi, S. Choi, M. Jeon, and S. Y. Lee, "Carbon nanotube-graphene composite for ionic polymer actuators," *Smart Materials and Structures*, vol. 21, no. 5, article 055012, 2012.
- [26] Y. Wang, J. Liu, Y. Zhu, D. Zhu, and H. Chen, "Formation and characterization of dendritic interfacial electrodes inside an ionomer," *ACS Applied Materials & Interfaces*, vol. 9, no. 36, pp. 30258–30262, 2017.
- [27] K. J. Kim and M. Shahinpoor, "A novel method of manufacturing three-dimensional ionic polymer-metal composites (IPMCs) biomimetic sensors, actuators and artificial muscles," *Polymer*, vol. 43, no. 3, pp. 797–802, 2002.
- [28] S. J. Lee, M. J. Han, S. J. Kim, J. Y. Jho, H. Y. Lee, and Y. H. Kim, "A new fabrication method for IPMC actuators and application to artificial fingers," *Smart Materials and Structures*, vol. 15, no. 5, pp. 1217–1224, 2006.
- [29] M. Shahinpoor and K. J. Kim, "Ionic polymer-metal composites: IV. Industrial and medical applications," *Smart Materials and Structures*, vol. 14, no. 1, pp. 197–214, 2004.
- [30] G. Y. Lee, J. O. Choi, M. Kim, and S. H. Ahn, "Fabrication and reliable implementation of an ionic polymer-metal composite (IPMC) biaxial bending actuator," *Smart Materials and Structures*, vol. 20, no. 10, article 105026, 2011.
- [31] S. J. Kim, D. Pugal, Y. Jung, J. Wong, K. J. Kim, and W. Yim, "A rod-shaped ionic polymer-metal composite for use as an active catheter-platform," in *ASME 2010 Conference on Smart Materials, Adaptive Structures and Intelligent Systems, Volume 2*, pp. 145–151, Philadelphia, PA, USA, October 2010.
- [32] S. J. Kim, D. Pugal, J. Wong, K. J. Kim, and W. Yim, "A bio-inspired multi degree of freedom actuator based on a novel cylindrical ionic polymer-metal composite material," *Robotics and Autonomous Systems*, vol. 62, no. 1, pp. 53–60, 2014.
- [33] V. Palmre, D. Pugal, K. J. Kim, and W. Yim, "An electroactive IPMC-based cylindrical robotic platform," in *2013 10th International Conference on Ubiquitous Robots and Ambient Intelligence (URAI)*, pp. 713–714, Jeju, South Korea, November 2013.
- [34] T. Stalbaum, S. E. Nelson, V. Palmre, and K. J. Kim, "Multi degree of freedom IPMC sensor," in *Electroactive Polymer Actuators and Devices (EAPAD) 2014*, San Diego, CA, USA, March 2014.
- [35] M.-J. Lee, S.-H. Jung, S. Lee, M.-S. Mun, and I. Moon, "Control of IPMC-based artificial muscle for myoelectric hand prosthesis," in *The First IEEE/RAS-EMBS International Conference on Biomedical Robotics and Biomechanics, 2006. BioRob 2006*, pp. 1172–1177, Pisa, Italy, February 2006.
- [36] T. T. Nguyen, N. S. Goo, V. K. Nguyen, Y. Yoo, and S. Park, "Design, fabrication, and experimental characterization of a flap valve IPMC micropump with a flexibly supported diaphragm," *Sensors and Actuators A: Physical*, vol. 141, no. 2, pp. 640–648, 2008.
- [37] S. L. Li, W. Y. Kim, T. H. Cheng, and I. K. Oh, "A helical ionic polymer-metal composite actuator for radius control of biomedical active stents," *Smart Materials and Structures*, vol. 20, no. 3, article 035008, 2011.
- [38] W. J. Yoon, P. G. Reinhall, and E. J. Seibel, "Analysis of electroactive polymer bending: a component in a low cost ultrathin

- scanning endoscope,” *Sensors and Actuators A: Physical*, vol. 133, no. 2, pp. 506–517, 2007.
- [39] B. K. Fang, M. S. Ju, and C. C. K. Lin, “A new approach to develop ionic polymer–metal composites (IPMC) actuator: fabrication and control for active catheter systems,” *Sensors and Actuators A: Physical*, vol. 137, no. 2, pp. 321–329, 2007.
- [40] B. K. Fang, C. C. K. Lin, and M. S. Ju, “Development of sensing/actuating ionic polymer–metal composite (IPMC) for active guide-wire system,” *Sensors and Actuators A: Physical*, vol. 158, no. 1, pp. 1–9, 2010.
- [41] S. Guo, T. Fukuda, K. Kosuge, F. Arai, K. Oguro, and M. Negoro, “Micro catheter system with active guide wire-structure, experimental results and characteristic evaluation of active guide wire catheter using ICPF actuator,” in *1994 5th International Symposium on Micro Machine and Human Science Proceedings*, p. 191, Nagoya, Japan, October 1994.
- [42] K. Oguro, N. Fujiwara, K. Asaka, K. Onishi, and S. Sewa, “Polymer electrolyte actuator with gold electrodes,” in *Smart Structures and Materials 1999: Electroactive Polymer Actuators and Devices*, pp. 64–71, Newport Beach, CA, USA, May 1999.
- [43] Y. Bahramzadeh and M. Shahinpoor, “Ionic polymer-metal composites (IPMCs) as dexterous manipulators and tactile sensors for minimally invasive robotic surgery,” in *Electroactive Polymer Actuators and Devices (EAPAD) 2012*, San Diego, CA, USA, April 2012.
- [44] A. R. Lanfranco, A. E. Castellanos, J. P. Desai, and W. C. Meyers, “Robotic surgery: a current perspective,” *Annals of Surgery*, vol. 239, no. 1, pp. 14–21, 2004.
- [45] F. Capri and E. Smela, *Introduction in Biomedical Applications of Electroactive Polymer Actuators*, Wiley, Chichester, UK, 2009.
- [46] K. J. Kim and S. Tadokoro, *Electroactive Polymers for Robotic Applications: Artificial Muscles and Sensors*, Springer, London, 2007.
- [47] M. Shahinpoor, K. J. Kim, and M. Mojarad, *Artificial Muscles: Applications of Advanced Polymeric Nanocomposites*, CRC Press, New York, London, 2007.
- [48] Y. Wang, H. Chen, Y. Wang et al., “Influence of additives on the properties of casting Nafion membranes and SO-based ionic polymer–metal composite actuators,” *Polymer Engineering & Science*, vol. 54, no. 4, pp. 818–830, 2014.
- [49] J. Liu, Y. Wang, D. Zhao, C. Zhang, H. Chen, and D. Li, “Design and fabrication of an IPMC-embedded tube for minimally invasive surgery applications,” in *Electroactive Polymer Actuators and Devices (EAPAD) 2014*, San Diego, CA, USA, March 2014.

Research Article

Biomimetic Beetle-Inspired Flapping Air Vehicle Actuated by Ionic Polymer-Metal Composite Actuator

Yang Zhao,¹ Di Xu,¹ Jiazheng Sheng,¹ Qinglong Meng,¹ Dezhi Wu,¹ Lingyun Wang,¹ Jingjing Xiao,¹ Wenlong Lv,^{1,2} Qinnan Chen ¹ and Daoheng Sun¹

¹Department of Mechanical and Electrical Engineering, Xiamen University, Xiamen, Fujian, China

²Pen-Tung Sah Institute of Micro-Nano Science and Technology, Xiamen University, Xiamen, Fujian, China

Correspondence should be addressed to Qinnan Chen; chenqinnan@xmu.edu.cn

Received 3 November 2017; Accepted 17 January 2018; Published 27 February 2018

Academic Editor: QingSong He

Copyright © 2018 Yang Zhao et al. This is an open access article distributed under the Creative Commons Attribution License, which permits unrestricted use, distribution, and reproduction in any medium, provided the original work is properly cited.

During the last decades, the ionic polymer-metal composite (IPMC) received much attention because of its potential capabilities, such as large displacement and flexible bending actuation. In this paper, a biomimetic flapping air vehicle was proposed by combining the superiority of ionic polymer metal composite with the bionic beetle flapping principle. The blocking force was compared between casted IPMC and IPMC. The flapping state of the wing was investigated and the maximum displacement and flapping angle were measured. The flapping displacement under different voltage and frequency was tested. The flapping displacement of the wing and the support reaction force were measured under different frequency by experiments. The experimental results indicate that the high voltage and low frequency would get large flapping displacement.

1. Introduction

Ionic polymer-metal composite (IPMC) is a new type of electroactive polymer material, which can produce large-size deformation under the excitation of electric field [1]. Since the mechanical properties and actuating characteristics of IPMC are very similar to biological muscle, it is also called “artificial muscle” [2]. Notable advantages of IPMC include low driving voltage, relatively large strain, and soft and lightweight mechanisms. It has good prospect and development potential in the fields of bionic robot, sensor, and energy harvesting [3]. In the past, bionic flapping air vehicles were mostly constructed of rigid materials, which were complex, inefficient, and heavy in weight [4, 5]. Due to the unique performance of the IPMC, it is being tried to be applied to flapping mechanism [6]. It is not only easy to control the mechanism by IPMC but also more similar to the biological flexibility [7]. Biomimetic flapping wing mechanisms are used for a deeper understanding of flapping flight [8].

In the last decades, many researchers concentrated on fabrication, modeling, and bionic application of IPMC. He developed an ionic polymer-metal-carbon nanotube

composite (IPMCC) actuator composed of a multiwalled carbon nanotube (MWCNT)/Nafion membrane sandwiched between two hybrid electrodes, composed of palladium, platinum, and MWCNTs. The V-I characteristics indicate that the change in shape becomes significant at amplitudes higher than 1.2 V [9]. Chen et al. proposed a novel synthesis technique to fabricate hybrid IPMC membrane actuator capable of generating 3-dimensional (3D) kinematic motions. By controlling each individual IPMC beams, complex 3D motions could be generated [10]. Zhao et al. developed a gradient structure of Nafion in thickness to improve the performance of IPMC. The results of the experiments indicate that the gradient structure would improve the performance both in deformation displacement and blocking force [11]. Caponetto et al. proposed an enhanced fractional-order transfer function (FOTF) model for IPMC membrane working as actuator [12]. He analyzed the effects of the thickness on the performance of IPMC with an electromechanical model. As the thickness increases, the elastic modulus of Nafion membrane and the blocking force of IPMC increase, but the current and the displacement decrease [13]. Shen et al. proposed a hybrid biomimetic

underwater vehicle that uses IPMCs as sensors. Propelled by the energy of waves, the underwater vehicle does not need an additional energy source [14]. Shi et al. developed a prototype movable robotic Venus flytrap and evaluated its walking and rotating speeds by using different applied signal voltages [15]. Otis presented the electromechanical characterization of Nafion-Pt microlegs for the development of an insect-like hexapod BioMicroRobot (BMR). BMR microlegs are built using quasi-cylindrical Nafion-Pt ionic polymer-metal composite (IPMC), which has 2.5 degrees of freedom [16]. The thrust performance of a biomimetic robotic swimmer that uses IPMC as a flexible actuator in viscous and inertial flow was studied by Shen et al. A hydrodynamic model based on the elongated body theory was developed [17]. Helical IPMC actuators are newly developed to control the radius of biomedical active stents by Li et al. The helix-shaped IPMC actuator was fabricated through the thermal treatment of an IPMC strip helically coiled on a glass rod. The helical IPMC actuator can be used to realize not only bending motion but also torsional and longitudinal motion [18]. Akle et al. presented the design and development of an underwater jellyfish-like robot using IPMC as propulsion actuators. A water-based IPMC demonstrates a fast strain rate of 1%/s but small peak strain of 0.3% and high current of 200 mA/cm [19]. Lee presented a trade-off design and fabrication of IPMC as an actuator for a flapping device. The internal solvent loss of IPMCs had been conducted for various combinations of cation and solvent in order to find out the best combination of cation and solvent for minimal solvent loss and higher actuation force [20]. Colozza discusses the development of a new aircraft based on a bird's flying principle. Rather than a metal framework covered by riveted plates and hydraulically actuated parts, ionic polymer-metal composite was proposed to be applied to the plane's body and wings [21]. Kim et al. developed a flapping actuator module operated at the resonant frequency by using an IPMC actuator. The performances of the IPMC actuators, including the deformation, blocking force, and natural frequency, were obtained according to the input voltage and IPMC dimensions. The empirical performance model and the equivalent stiffness model of the IPMC actuator are established [22]. Mukherjee and Ganguli used an energy-based variational approach for structural dynamic modeling of the IPMC flapping wing. An optimization study was performed to obtain improved flapping actuation of the IPMC wing. The optimization algorithm leads to a flapping wing with dimensions similar to the dragonfly *Aeshna multicolor*'s wing [23]. With the development of IPMC, it has a wide prospect in bionic robot and other applications. But applying IPMC in flapping air vehicle has lack of study. Due to the unique performance of the IPMC, it can be suitably used in the bionic flapping actuation.

By combing the principle of bionics of beetle flapping, a biomimetic beetle-inspired flapping air vehicle was proposed in this work. The flapping mechanism was fabricated by casted IPMC. The flapping state of beetle-inspired air vehicle was used to analyze the flapping displacement and angle of the wing. The regularity of flapping displacement was investigated under different conditions. Experiments of



FIGURE 1: Wings of beetle.

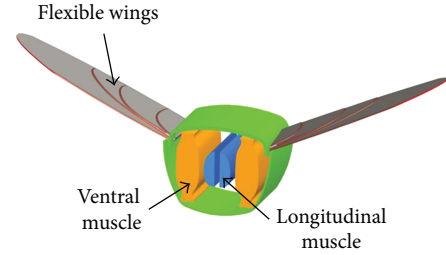


FIGURE 2: Schematic of beetle flapping bionics.

support reaction force of flapping mechanism were performed and the concept of biomimetic flapping air vehicle actuated by IPMC is shown feasible.

2. Beetle-Inspired Flapping Mechanism Design

Beetle flight depends on the control of the chest elastic movement and the force acting on the wings, as shown in Figure 1. The flapping way of the wings is similar to a tuning fork resonance effect. A beetle does not directly flap its wings, but it uses alternating movement of two groups of chest muscle to produce deformation, as shown in Figure 2. Through this way, the wings and chest resonate to produce high-frequency large flapping cycle.

The flapping wings of the insects have two kinds of motions: the longitudinal stroke and the rotation of the wings. In this study, we just consider the stroke of wings [24, 25]. When the wing flaps, the angular velocity of stroking ω_s is not exactly a simple harmonic motion but a complicated nonlinear motion. In the process of acceleration and deceleration, $\omega_s(t)$ can be treated as simple harmonic motion.

$$\omega_s(t) \begin{cases} \omega_m \sin\left(\frac{t\pi}{\Delta t_s}\right), & t \in [0, 0.5\Delta t_s], \\ \omega_m, & t \in (0.5\Delta t_s, 0.5T - 0.5\Delta t_s], \\ \omega_m \sin\left[(0.5T - 0.5t)\frac{\pi}{\Delta t_s}\right], & t \in (0.5T - 0.5\Delta t_s, 0.5T + 0.5\Delta t_s], \\ -\omega_m, & t \in (0.5T + 0.5\Delta t_s, T - 0.5\Delta t_s], \\ \omega_m \sin\left[(t - T)\frac{\pi}{\Delta t_s}\right], & t \in (T - 0.5\Delta t_s, T], \end{cases}$$

$$\omega_m = \frac{\theta_m}{(2\Delta t_s)/(\pi + 0.5T - \Delta t_s)}, \quad (1)$$

where θ_m is the angle amplitude of flapping wing.

In the design process of the beetle-inspired flapping mechanism, a 50 mm long, 10 mm wide, and 420 μm thick IPMC was selected for the actuation because the primary concerns are actuation force and response speed. As shown in Figure 3, the skeleton of flapping mechanism was made of PET film, the wings were made of PVC film, and the size of the wing is 42 mm in length and 15 mm in width. The wing was fixed on the outer surface of PET skeleton by free hinge joint. The IPMC actuator was gripped by a clamp at one side and attached the wings at another side to transfer the actuation force from the IPMC actuator to the wing. Therefore, the bending motion of the IPMC actuator would produce the flapping motion of the beetle-inspired mechanism.

An electromechanical modeling was established for IPMC based on thermodynamics theory [26, 27]. The deformation of IPMC under the combined effect of force field and electric field is as follows:

$$\frac{1}{\rho} = \frac{M}{YI_z} = \frac{M_m + M_e}{YI_z}. \quad (2)$$

The moment M_m by force is described as

$$M_m = \frac{YI_z}{\rho} - M_e = \frac{YI_z}{\rho} - BE, \quad (3)$$

where ρ is the curvature radius after bending deformation, M_m is the moment by force, and M_e is the moment by electrical field. Y is the elastic modulus of IPMC and I_z is the moment of inertia of cross section to z -axis. E is the electric field and B is the bending coefficient of IPMC and is proportional to the square of the length and linearly proportional to the width and thickness of IPMC. Besides, it is also related to the conductivity of the sample and the diffusion rate of the ions used.

3. Experiments

3.1. Fabrication of Casted IPMC. The performance of the IPMC varies with its thickness, such as deformation and blocking force. Thick IPMC was chosen for the actuation of the beetle-inspired mechanism. To achieve the desired thick Nafion film, the casting method with Nafion dispersion from DuPont™ was used to fabricate the IPMC in this study. Nafion dispersion and dimethylformamide (DMF) were poured together to cast the Nafion film. The proportion of Nafion and DMF is 4 : 1. The use of DMF is to prevent surface cracks in solidified Nafion during solvent evaporation. The mixed solution was stirred with a magnetic stirrer to make the solution homogeneous. The solution is then placed in a constant-temperature drying oven. The solvent was fully evaporated at 70°C in the oven. It takes almost 18 hours to form the film. The Nafion film was conserved in deionized water. The electrodes of Pt attached to both sides of the Nafion film were fabricated by electroless plating. First, number 1500 sandpaper was used to roughen the surface of the film along one direction. It was used to increase the interfacial area to make the electrode material deposits. Then the film was rinsed chemically with H_2SO_4 (0.5%) and H_2O_2 (15%) solution, rinsed with boiled deionized water, and

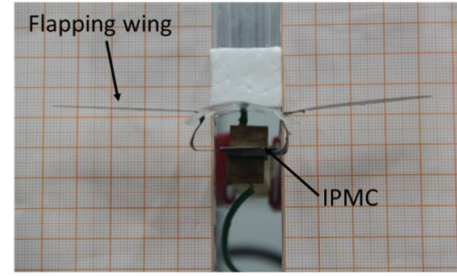


FIGURE 3: Beetle-inspired flapping mechanism.

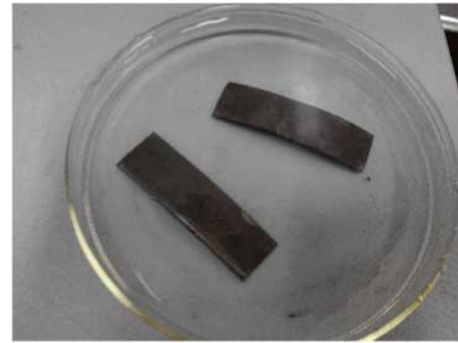


FIGURE 4: Casted IPMC sample.

dipped into H_2SO_4 (0.5%). Second, the film was dipped into the solution of $[\text{Pt}(\text{NH}_3)_4]\text{Cl}_2$ (3 mg/mm^2) for about 12 hours to accomplish ion exchange. Third, the platinum complex cations were reduced to the metallic state by using the reducing agents NaBH_4 (5%); the reaction temperature was from 40 to 60°C. The electrode of Pt was deposited on the surface of the film. Fourth, the film was prepared for the second reduction reaction by rinsing in ultrasonic cleaners after the first reduction reaction. Fifth, the solution of hydrazine hydrate (20%) and the solution of hydroxylammonium chloride (5%) were used to perform the second reduction as the reducing agents. After this reduction, the IPMC sample was fabricated, as shown in Figure 4. Finally, the IPMC sample was rinsed with deionized water and stored in a solution of LiCl for experiment [11].

3.2. Experimental Setup. Since the main performance characteristic of flapping air vehicle is the flapping displacement of the wing, the flapping displacement measurement system was established. The experimental setup of the flapping displacement measurement system is shown in Figure 5. The beetle-inspired flapping air vehicle was placed in front of the coordinate paper (1 mm * 1 mm per grid); the actuated flapping process was captured by digital camera; and the flapping displacement data of the wing was acquired by a laser displacement sensor (LK-080).

The experimental setup of the blocking force measurement system was also established, as shown in Figure 6. The blocking force was measured by a load cell (XH10-5 g) and data acquisition was done by using National Instruments™ PXI system with PXIe-6361 (DAQ).

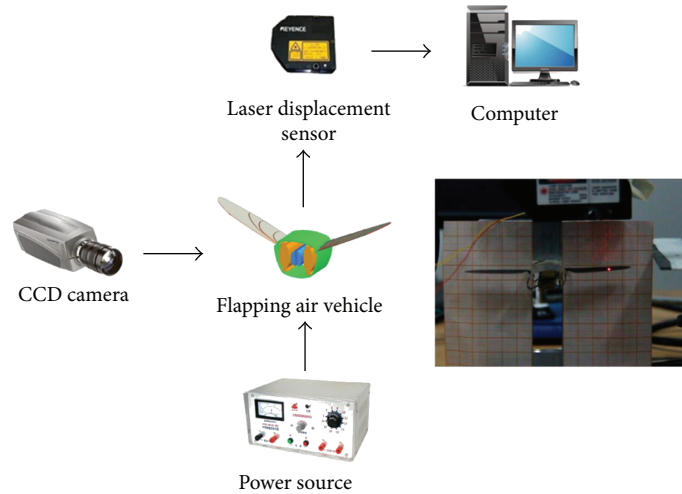


FIGURE 5: Displacement measurement system.

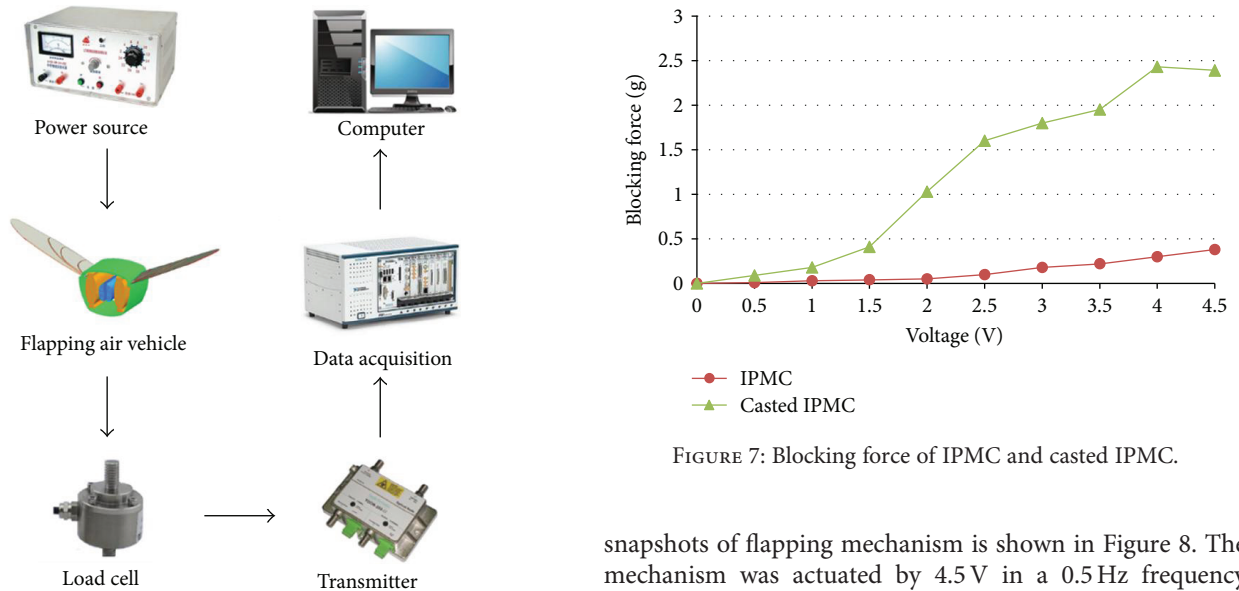


FIGURE 7: Blocking force of IPMC and casted IPMC.

FIGURE 6: Force measurement system.

4. Results and Discussion

The IPMC actuator of beetle-inspired air vehicle was fabricated by a casted Nafion membrane. The thickness of IPMC by the casted Nafion was $420\ \mu\text{m}$. Driven by 0–4.5 V DC, the blocking force of IPMC fabricated by the casted Nafion was compared with IPMC fabricated by a commercial Nafion-117 in Figure 7. It can be found that the blocking force of IPMC by casted Nafion is larger than IPMC fabricated by Nafion-117; the IPMC by casted Nafion can create 2.4 grams of force for 4 V DC. It is suitable for the actuation of a flapping wing than IPMC fabricated by Nafion-117.

The wings of the beetle-inspired air vehicle flap in upstroke and downstroke when AC voltage is applied. The front view of the flapping motion of the beetle-inspired air vehicle was recorded by CCD camera. The consecutive

snapshots of flapping mechanism is shown in Figure 8. The mechanism was actuated by 4.5 V in a 0.5 Hz frequency sinusoidal wave input voltage. Take one snapshot per 0.5 second. As shown in Figure 8(a), the wings of the mechanism were at the lowest position at 0 second. Then the wings flap in an upstroke position. The highest position of upstroke is at 1 second. After the downstroke of the flapping wings, the wings return to the original position at 2 seconds to finish one upstroke and downstroke cycle. From Figure 8, the maximum tip displacements of the wing is exceeding 10 mm; the maximum flapping angle is 12.5 degrees.

Figure 9 shows the results of the wing displacements of beetle-inspired air vehicle under different voltage and frequency. The displacements of the wing keep increasing with the increase in the actuation voltage. Meanwhile, the displacements of the wing keep decreasing with the increase in the actuation frequency. The reason is that the driving voltage increases and the blocking force of IPMC increases under the same frequency, so the displacements of the wing generated by the IPMC increase. Under the same driving voltage, the driving frequency decreases and the driving time

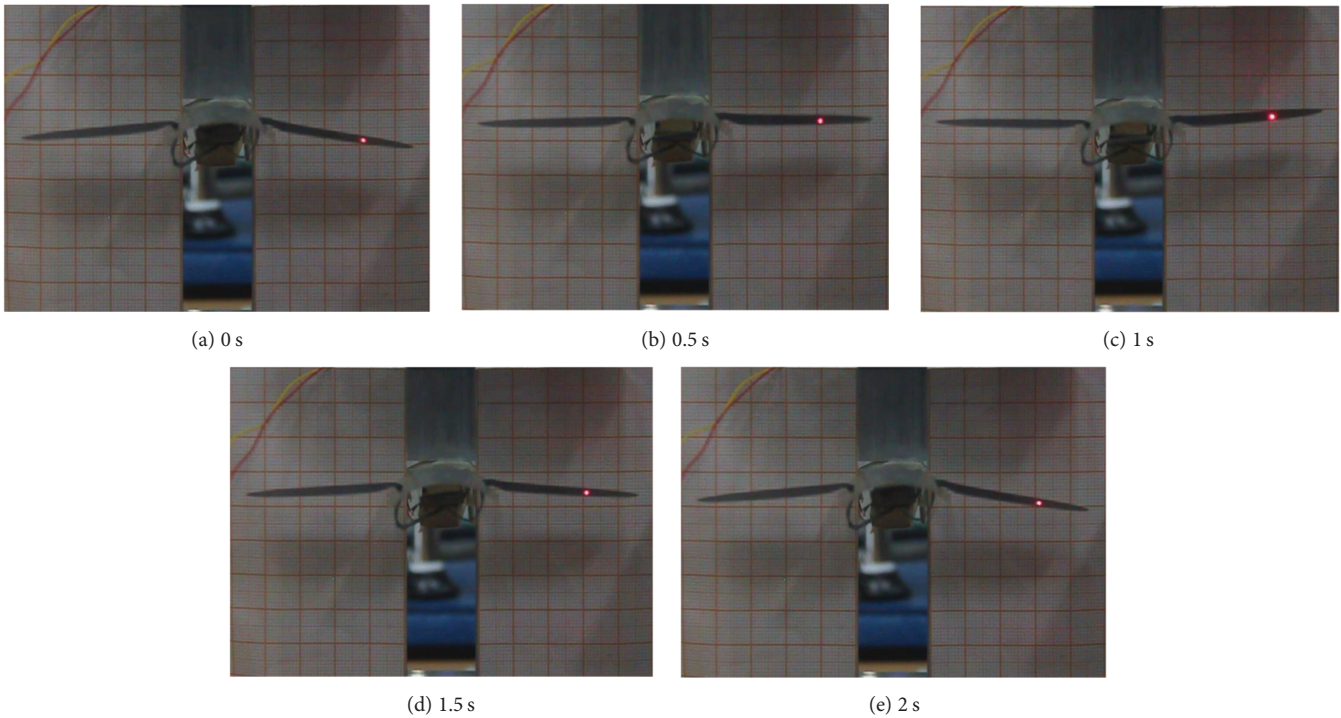


FIGURE 8: Flapping motion of the beetle-inspired air vehicle.

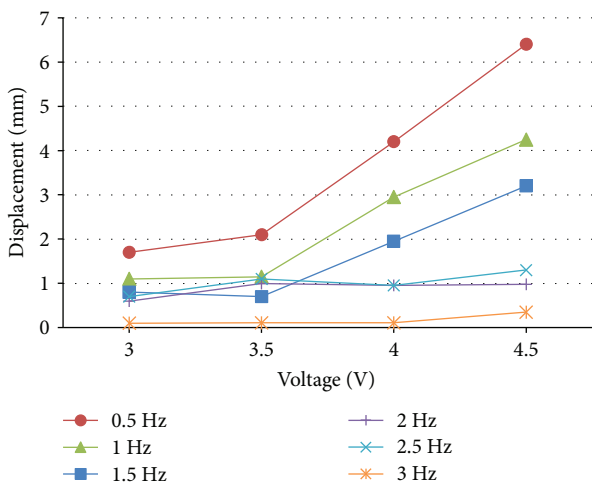


FIGURE 9: Displacements of the wing under different voltage and frequency.

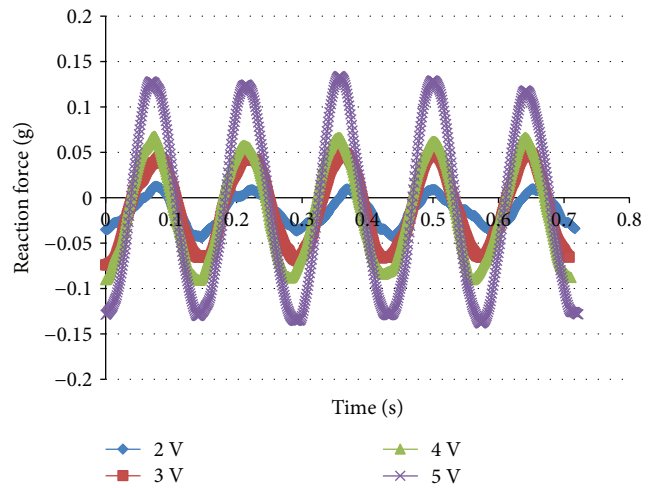


FIGURE 10: Reaction force of flapping mechanism under 7 Hz, 2–5 V AC.

is lengthened; thus, the displacements increase. It can be seen that the maximum displacement of the wing is obtained under the 4.5 V in 0.5 Hz; the value is 6.4 mm. Similarly, the flapping angle was reduced for higher input frequency.

When the actuation frequency of IPMC is close to the resonant frequency, low-amplitude high-frequency flapping of the wing could be realized. As a result of frequency-sweeping test, the resonant frequency of the IPMC is 7.5 Hz. The measurement of reaction force of the support was carried out at the resonant frequency. Figures 10–12 show the reaction force under a 7 Hz, 7.5 Hz, and 8 Hz

sinusoidal input voltage with amplitude varying from 2 to 5 V at 1 V intervals, respectively. With the increase of actuation voltage, the reaction force increases and it also exhibits the regularity of sinusoidal input. As shown in Figure 11, the reaction force under 7.5 Hz is larger than that of 7 Hz and 8 Hz. It indicates that more actuation force and high-frequency flapping could be obtained at the resonant frequency. But it can be seen from the results of the measurement that the actuation force is low when AC voltage is applied, and it is difficult to actuate the flapping wing under high frequency and low voltage.

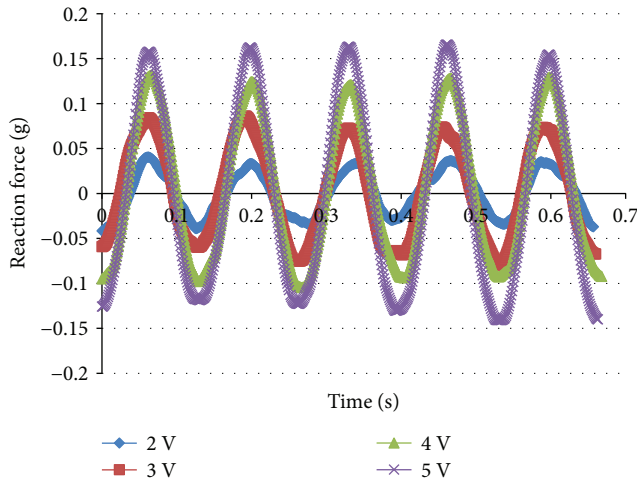


FIGURE 11: Reaction force of flapping mechanism under 7.5 Hz, 2–5 V AC.

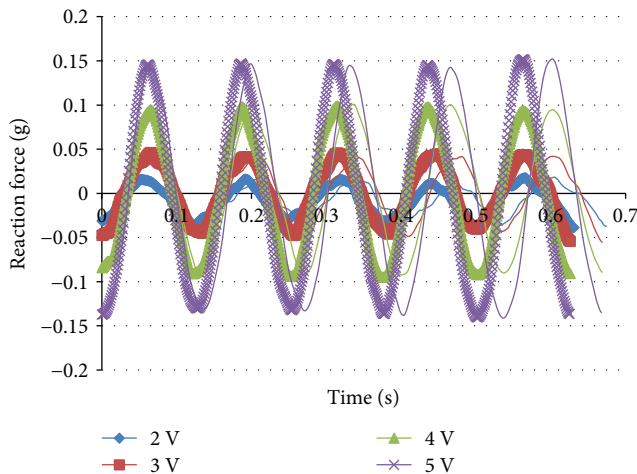


FIGURE 12: Reaction force of flapping mechanism under 8 Hz, 2–5 V AC.

5. Conclusions

In this study, the biomimetic flapping principle of beetle is presented. A beetle-inspired flapping air vehicle is proposed and fabricated by using IPMC actuator of casted Nafion. The thickness of the casted Nafion is $420\ \mu\text{m}$. The blocking force measurement was carried out to verify the performance of flapping actuation. The flapping state of air vehicle was investigated. The maximum tip displacement and flapping angle were measured. The experiments of displacement test of the flapping wing under different voltage and frequency were investigated. Increasing the voltage and decreasing the frequency would get larger displacements. But it still needs further research for practical use. Future work would be concentrated on the improvement of lift force of the vehicle and the biomimetic pattern of mimicking the flapping wing. The improvement of the performance of IPMC actuator by material modification also needs to be studied.

Conflicts of Interest

The authors declare that they have no conflicts of interest.

Acknowledgments

This work is financially supported by the National Natural Science Foundation of China (no. 51505401, no. 91648114, and no. 61605163), Health-Education Joint Research Projects of Fujian Province (no. WKJ2016-2-21), and Fundamental Research Funds for the Central Universities of Xiamen University (no. 20720150082).

References

- [1] C. Jo, D. Pugal, I. K. Oh, K. J. Kim, and K. Asaka, "Recent advances in ionic polymer–metal composite actuators and their modeling and applications," *Progress in Polymer Science*, vol. 38, no. 7, pp. 1037–1066, 2013.
- [2] M. Shahinpoory, Y. Bar-Cohenz, J. O. Simpsonx, and J. Smith, "Ionic polymer–metal composites (IPMCs) as biomimetic sensors, actuators and artificial muscles: a review," *ACS Symposium*, vol. 726, no. 6, pp. 251–267, 1998.
- [3] Z. Q. Zhang, J. Zhao, H. L. Chen, and D. S. Chen, "A survey of bioinspired jumping robot: takeoff, air posture adjustment, and landing buffer," *Applied Bionics and Biomechanics*, vol. 2017, Article ID 4780160, 22 pages, 2017.
- [4] J. W. Gerdes, S. K. Gupta, and S. A. Wilkerson, "A review of bird-inspired flapping wing miniature air vehicle designs," *Journal of Mechanisms and Robotics*, vol. 4, article 021003, 2012.
- [5] J. S. Palmisano, J. D. Geder, R. Ramamurti, W. C. Sandberg, and B. Ratna, "Robotic pectoral fin thrust vectoring using weighted gait combinations," *Applied Bionics and Biomechanics*, vol. 9, no. 3, pp. 333–345, 2012.
- [6] S. S. Jayabalan, R. Ganguli, and G. Madras, "Nanomaterial-based ionic polymer metal composite insect scale flapping wing actuators," *Mechanics of Advanced Materials and Structures*, vol. 23, no. 11, pp. 1300–1311, 2016.
- [7] Y. Bahramzadeh and M. Shahinpoor, "A review of ionic polymeric soft actuators and sensors," *Soft Robotics*, vol. 1, no. 1, pp. 38–52, 2014.
- [8] J. S. Swarrup, G. Ranjan, and M. Giridhar, "Structural modeling of actuation of IPMC in dry environment: effect of water content and activity," *Smart Structures and Systems*, vol. 19, no. 5, pp. 553–565, 2017.
- [9] Q. He, L. Song, M. Yu, and Z. D. Dai, "Fabrication, characteristics and electrical model of an ionic polymer metal–carbon nanotube composite," *Smart Materials and Structures*, vol. 24, no. 7, article 075001, 2015.
- [10] Z. Chen, T. I. Um, and H. Bart-Smith, "A novel fabrication of ionic polymer–metal composite membrane actuator capable of 3-dimensional kinematic motions," *Sensors and Actuators A: Physical*, vol. 168, no. 1, pp. 131–139, 2011.
- [11] Y. Zhao, B. Xu, G. Zheng et al., "Improving the performance of IPMCs with a gradient in thickness," *Smart Materials and Structures*, vol. 22, no. 11, article 115035, 2013.
- [12] R. Caponetto, S. Graziani, F. Sapuppo, and V. Tomasello, "An enhanced fractional order model of ionic polymer–metal composites actuator," *Advances in Mathematical Physics*, vol. 2013, Article ID 717659, 6 pages, 2013.

- [13] Q. He, M. Yu, L. Song, H. Ding, X. Zhang, and Z. Dai, "Experimental study and model analysis of the performance of IPMC membranes with various thickness," *Journal of Bionic Engineering*, vol. 8, no. 1, pp. 77–85, 2011.
- [14] Q. Shen, T. Wang, and K. J. Kim, "A biomimetic underwater vehicle actuated by waves with ionic polymer–metal composite soft sensors," *Bioinspiration & Biomimetics*, vol. 10, no. 5, article 055007, 2015.
- [15] L. Shi, Y. He, S. Guo, H. Kudo, M. Li, and K. Asaka, "IPMC actuator-based a movable robotic venus flytrap," in *2013 ICME International Conference on Complex Medical Engineering*, pp. 375–378, Beijing, China, May 2013.
- [16] M. J. D. Otis, "Electromechanical characterization and locomotion control of IPMC BioMicroRobot," *Advances in Materials Science and Engineering*, vol. 2013, Article ID 683041, 17 pages, 2013.
- [17] Q. Shen, T. Wang, J. Liang, and L. Wen, "Hydrodynamic performance of a biomimetic robotic swimmer actuated by ionic polymer–metal composite," *Smart Materials and Structures*, vol. 22, no. 7, article 075035, 2013.
- [18] S. L. Li, W. Y. Kim, T. H. Cheng, and I. K. Oh, "A helical ionic polymer-metal composite actuator for radius control of biomedical active stents," *Smart Materials and Structures*, vol. 20, no. 3, article 035008, 2011.
- [19] B. Akle, J. Najem, D. Leo, and J. Blottman, "Design and development of bio-inspired underwater jellyfish like robot using ionic polymer metal composite (IPMC) actuators," in *Proceedings Volume 7976, Electroactive Polymer Actuators and Devices (EAPAD) 2011*, San Diego, CA, USA, March 2011.
- [20] S. G. Lee, H. C. Park, S. D. Pandita, and Y. Yoo, "Performance improvement of IPMC (ionic polymer metal composites) for a flapping actuator," *International Journal of Control, Automation and Systems*, vol. 4, no. 6, pp. 748–755, 2006.
- [21] A. Colozza, "Fly like a bird," *IEEE Spectrum*, vol. 44, no. 5, pp. 38–43, 2007.
- [22] H. I. Kim, D. K. Kim, and J. H. Han, "Study of flapping actuator modules using IPMC," in *Proceedings Volume 6524, Electroactive Polymer Actuators and Devices (EAPAD) 2007*, San Diego, CA, USA, April 2007.
- [23] S. Mukherjee and R. Ganguli, "A dragonfly inspired flapping wing actuated by electro active polymers," in *50th AIAA/ASME/ASCE/AHS/ASC Structures, Structural Dynamics, and Materials Conference*, Palm Springs, CA, USA, May 2009.
- [24] S. Mukherjee and R. Ganguli, "Nonlinear dynamic analysis of dragonfly-inspired piezoelectric unimorph actuated flapping and twisting wing," *International Journal of Smart and Nano Materials*, vol. 3, no. 2, pp. 103–122, 2012.
- [25] Q. V. Nguyen, W. L. Chan, and M. Debiasi, "An insect-inspired flapping wing micro air vehicle with double wing clap-fling effects and capability of sustained hovering," in *Proceedings Volume 9429, Bioinspiration, Biomimetics, and Bioreplication 2015*, San Diego, CA, USA, March 2015.
- [26] C. Jo, E. Naguib Hani, and H. Kwon Roy, "Modeling and optimization of the electromechanical behavior of an ionic polymer–metal composite," *Smart Materials and Structures*, vol. 17, no. 6, article 065022, 2008.
- [27] H. G. Liu, K. Xiong, K. Bian, and K. J. Zhu, "Experimental study and electromechanical model analysis of the nonlinear deformation behavior of IPMC actuators," *Acta Mechanica Sinica*, vol. 33, no. 2, pp. 382–393, 2017.

Research Article

Passive Cushiony Biomechanics of Head Protection in Falling Geckos

Hao Wang ¹, Wenbo Wang,¹ Yi Song,² Lei Cai ¹ and Zhendong Dai¹

¹College of Astronautics, Nanjing University of Aeronautics and Astronautics, Nanjing 210016, China

²College of Aerospace Engineering, Nanjing University of Aeronautics and Astronautics, Nanjing 210016, China

Correspondence should be addressed to Hao Wang; haowang@nuaa.edu.cn

Received 16 October 2017; Revised 23 December 2017; Accepted 15 January 2018; Published 19 February 2018

Academic Editor: Qi Shen

Copyright © 2018 Hao Wang et al. This is an open access article distributed under the Creative Commons Attribution License, which permits unrestricted use, distribution, and reproduction in any medium, provided the original work is properly cited.

Gekko gekkos are capable to crawl on the steep even on upside-down surfaces. Such movement, especially at great altitude, puts them at high risks of incidentally dropping down and inevitable body or head impactions, though they may trigger air-righting reaction (ARR) to attenuate the landing shocks. However, the air-righting ability (ARA) in *Gekko gekkos* is not fully developed. The implementation of ARR in some geckos is quite slow; and for those without tails, the ARR is even unobservable. Since ARA is compromised in *Gekko gekkos*, there must be some other mechanisms responsible for protecting them from head injuries during falls. In this study, we looked into a *Gekko gekko*'s brain to study its internal environment and structure, using the magnetic resonance imaging (MRI) technique. The results showed that the brain parenchyma was fully surrounded by the cerebrospinal fluid (CSF) in the skull. A succulent characteristic was presented, which meant the intracalvarium was significantly occupied by the CSF, up to 45% in volume. Then a simplified three-dimensional finite element model was built, and a dynamic simulation was conducted to evaluate the mechanical property of this succulent characteristic during the head impactions. These implied the succulent characteristic may play certain roles on the self-protection in case of head impact, which is adaptable to the *Gekko gekko*'s locomotion and behavior.

1. Introduction

Many animals in nature are able to crawl, climb, or run on different inclined surfaces, such as walls, ceilings, branches, and leaves, at a certain height above the earth. Falling down, as a common experience, is somehow unavoidable. To avoid the body being injured when falling and impacting with the ground, animals have developed various abilities, such as air-righting abilities (ARA). Cats try to make their feet to attach on the ground at first to reduce the impact forces acting on the body by turning up the body upside-down through the vertebra and tail [1–4]. *Gekko gekkos* turn up by rotating their tail [5]. Preventing the brain injury from the falling and impacting to the ground, a sort of self-protection is one of the important survival skills gained from natural selection and evolution in animals. Aerial maneuverability or air-righting performance is the most important mechanism of self-protection in insects [6, 7], cats [1–4], rats [8, 9], rabbits [10], frogs [11], and geckos [5]. However, the air-righting is

not always performed perfectly in geckos. It was showed that the geckos without tails could not perform air-righting reaction (ARR) at all, and even for the geckos with tails, almost one-tenth could not perform ARR well [5]. Actually, the ARA might be weaker in *Gekko gekkos*, because the relevant air-righting reflex did not mature, developmentally speaking, into a complete central program. The published data [9] provided evidence that the ARA probably starts developmentally as a reflex and within days/weeks mature into a central pattern generator (CPG) by showing that the completion of the ARR maturation process had no dependency on loads attached to different parts of the body. In our behavior experiments, not all geckos could turn around successfully in abdomen-up falling down. Especially when the falling height is not so high, the time for free fall is not sufficient for this performance. Even though, it rarely causes any injury in the brain. The head impaction is cushioned somehow. It seems that *Gekko gekkos* may possess certain characteristics to prevent themselves especially their head from injury caused by

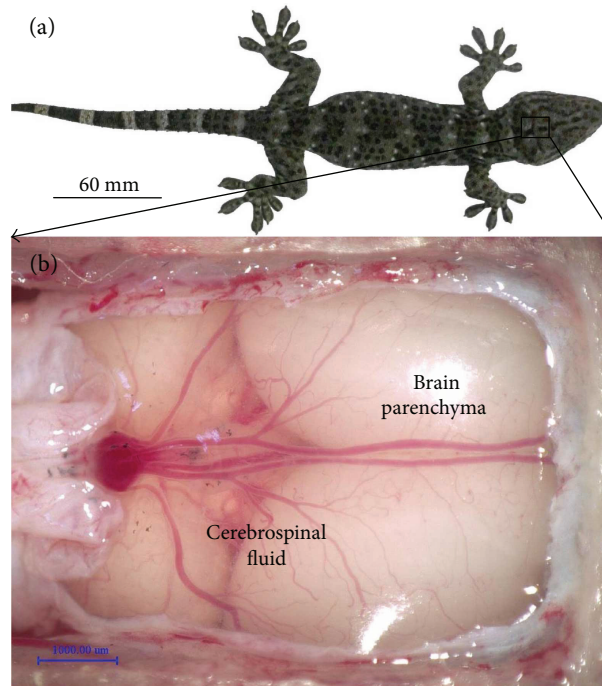


FIGURE 1: (a) A *Gekko gekko* lizard and (b) the observation on the intracalvarium of gecko brain using a digital microscope (VHX-600, Keyence, Japan) after craniotomy (the skull was opened and the dura was removed while the arachnoid was intact).

impacting the ground while falling down. To disclose the potential mechanism underlying the self-protection in head impactation, it is necessary to look into the intracalvarium structure and material of the animal's head.

Not like a woodpecker's head, which has been studied thoroughly for decades [12–15], a *Gekko gekko*'s head has been rarely investigated, since its significance of antishock characteristic is much lower than the former. The woodpecker's head can stand high-frequency shocks that are introduced from its drumming beak during the daily forage, while the gecko's head is only in the risk of one sudden head shock caused by an incident dropping. The underlying mechanism of head protection should be different. Here, we took a close look at the intracranial structures by the magnetic resonance imaging (MRI) technique. Then a simplified mathematical model was built to qualitatively evaluate the corresponding mechanical property.

2. Materials and Methods

2.1. Experimental Animals. The *Gekko gekko* lizards were brought from Nanning, Guangxi Province, China, and habituated to the study colony for two months before the experiments. The mean temperature and relative humidity were 25°C and 65%, respectively, which were close to the values for the natural ambience of *Gekko gekkos*. Adult *Gekko gekkos* weighted 40–70 g were selected for the MRI study.

The entire study was carried out in accordance with the Guide of Laboratory Animal Management Ordinance of China and approved by the Jiangsu Association for Laboratory Animal Science (Jiangsu, China).

2.2. The Intracalvarium Morphology Investigation. The intracalvarium morphology was investigated by two ways, the qualitative observation after the surgical anatomy and the quantitative measurement using MRI.

After the surgical anatomy, we found that the gecko's brain parenchyma (Figure 1) is surrounded by the cerebrospinal fluid (CSF).

For MRI investigation, the animal was anaesthetized by the intraperitoneal injection of 0.4% sodium pentobarbital in a 0.75% NaCl solution. A dose of 0.75 ml/100 g body weight was administered. After the pain reflex had disappeared, the gecko was fixed to a custom-designed fixture (manuscript in preparation, see Figure 2) and then placed into the MRI instrument (BioSpec 7T/20 cm, Bruker, Germany). The whole brain was scanned in three orthogonal (sagittal, coronal, and horizontal) planes (Figure 3), and the corresponding spatial interval of the scan was all 0.30 mm.

Based on the MRI image sequence, the distribution and the volume of the CSF in the skull were evaluated with the help of the open source software ImageJ (<http://rsbweb.nih.gov/ij/>). It is not difficult to distinguish the brain parenchyma and the CSF by gray level of the MRI image. Then, the surface integral and the volume integral were conducted for the brain parenchyma and the CSF, respectively.

3. Results and Discussion

3.1. Distribution of the CSF in the Gecko Skull. The percentage distribution of the CSF in the gecko skull is shown in Figure 4. Since the dimensions of the brain along the sagittal, coronal, and vertical directions are different, the number of slices is variable. It provided relatively more detail along the

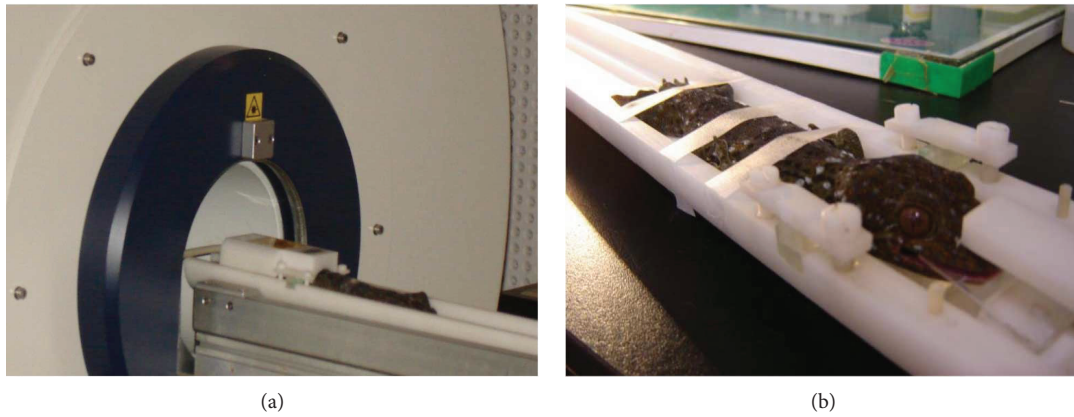


FIGURE 2: An anaesthetized gecko is placed into the MRI instrument, whose head and body are fixed to a custom-designed fixture (a). The close view of the fixed gecko in the fixture without cover (b).

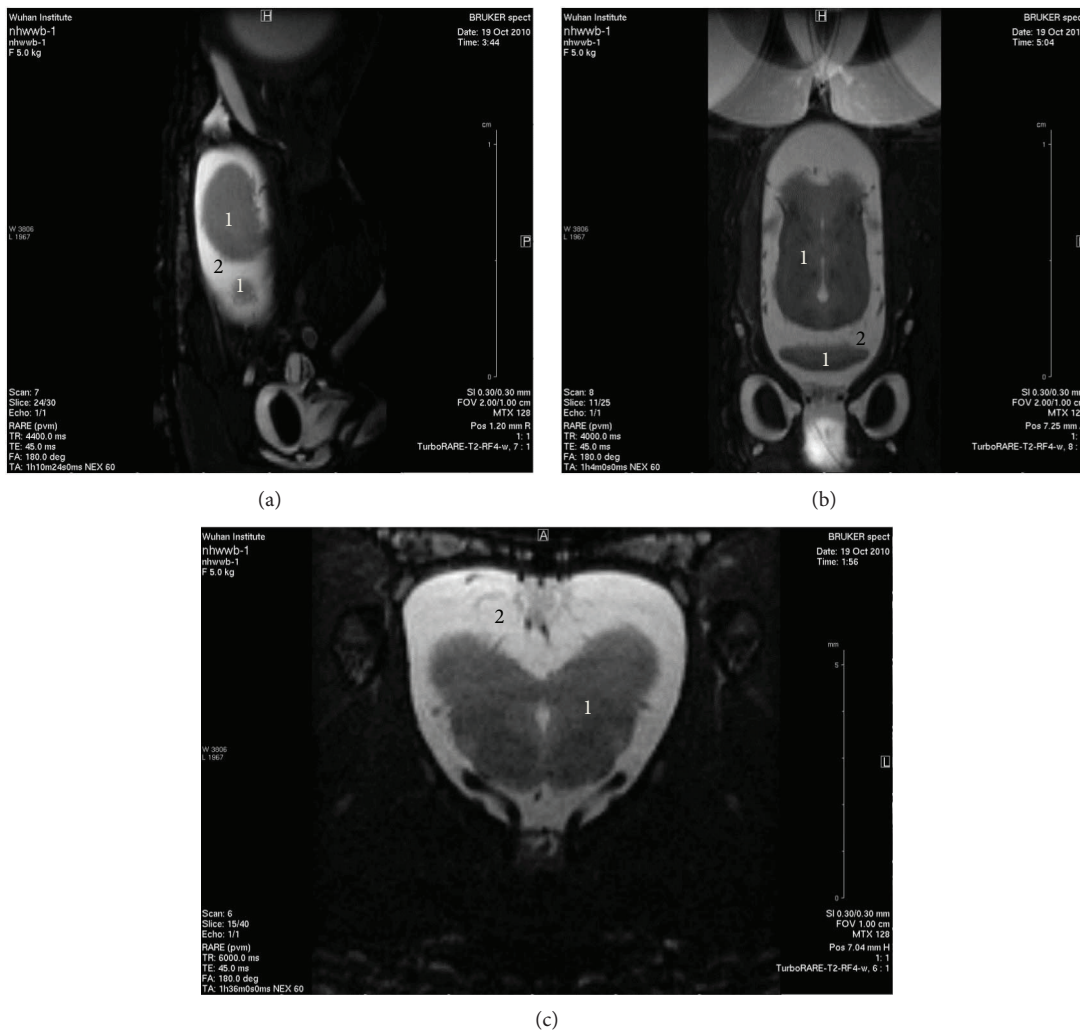


FIGURE 3: The MRI scanning of a gecko head in the sagittal plane (a), horizontal plane (b), and coronal plane (c). The dark area (marked by “1”) indicates the brain parenchyma while the bright area (marked by “2”) the CSF.

sagittal direction (coronal plane, Figure 4(c)), so the corresponding image sequence was employed to calculate the volume of the brain parenchyma and the CSF. The distribution

is clearly symmetrical along the coronal direction (sagittal plane, Figure 4(a)) due to the morphologically bilateral symmetry of the brain. The MRI images and the diagrams show

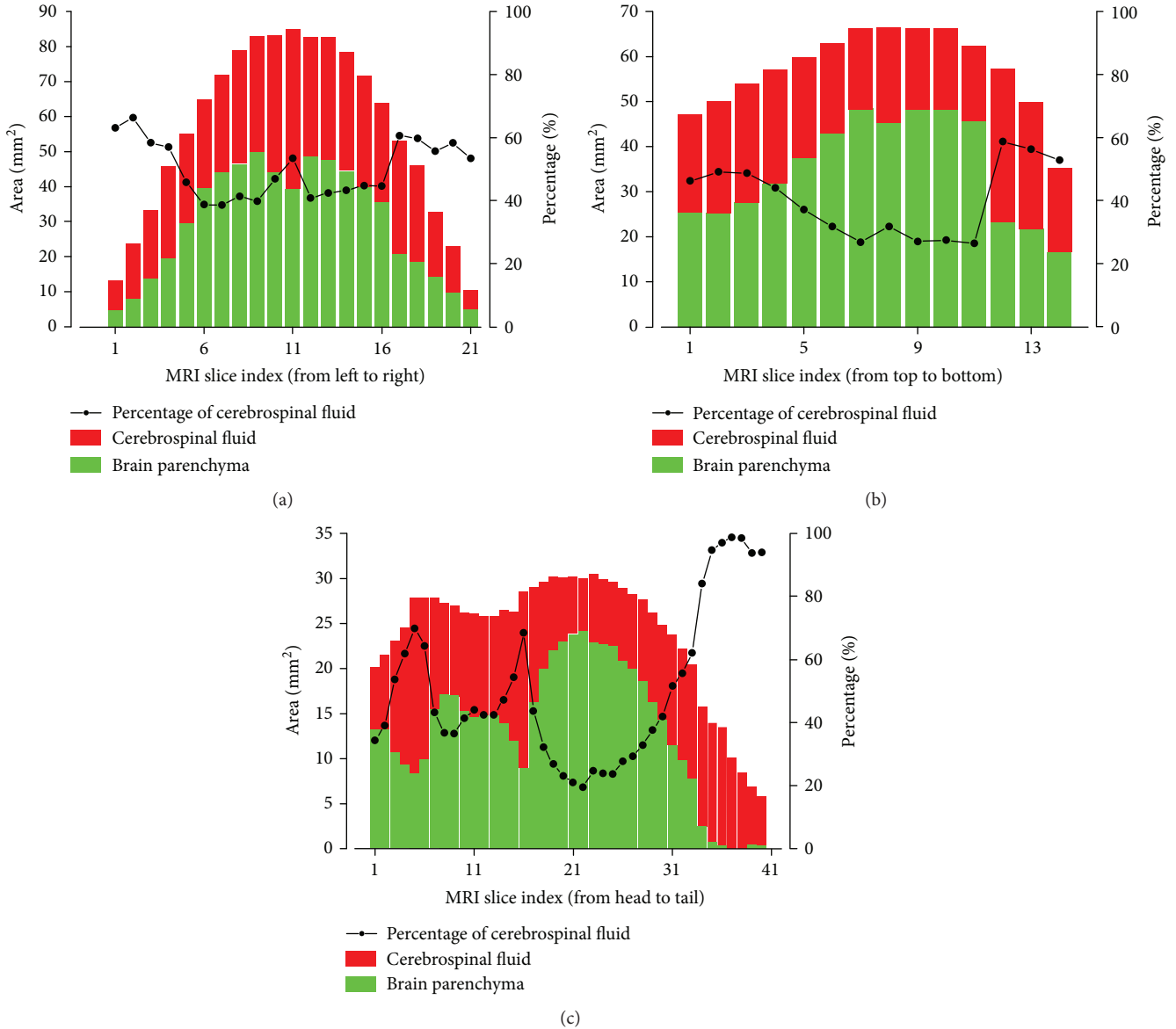


FIGURE 4: The percentage distribution of the CSF in the gecko skull along the coronal direction ((a), sagittal plane), vertical direction ((b), horizontal plane), and sagittal direction ((c), coronal plane). The outer envelope of the CSF indicates the full sectional area of the inner skull.

that the brain parenchyma is fully surrounded by the CSF. The minimum percentage of the CSF is still above 20%.

Based on the data shown in Figure 4(c), the volume of the brain parenchyma and the CSF was integrated as 159.0 mm³ and 127.4 mm³, respectively. Thus, the CSF accounts for about 45% of the entire brain volume.

3.2. The Finite Element Model of a Simplified Gecko Brain. The gecko brain was simplified into concentric spheres filled with liquid interval (Figure 5(a)). The parenchyma density of the gecko brain was around 1060 kg/m³, which was estimated by the ratio of mass to volume. Considering the irregular geometrical shape, the parenchyma volume was decided using the fluid volume measuring method. The density of the brain parenchyma [16, 17] is quite close to 1036 kg/m³. The density

of CSF was also measured around 989 kg/m³. And the viscosity coefficient (μ) of the CSF [18] is around 0.85 mPa·s.

The plan model was introduced to present the mechanics of the head impact cushioning. The contact target surface (ground) is defined as a rigid body in the model. The elasticity modulus and passion ratio of skull and brain parenchyma are set to be 15 GPa and 0.3 GPa, respectively. The Young's modulus for the CSF was set at 2.436 GPa, similar processing as the biomechanical study on the hemolymph in insects [19].

The finite element model was built and simulated using the ABAQUS/Explicit (ABAQUS 6.6, ABAQUS, Inc., USA), which is always chosen to solve nonlinear dynamical problems such as impact and explosion. Considering the symmetrical structure, the finite element model was built as

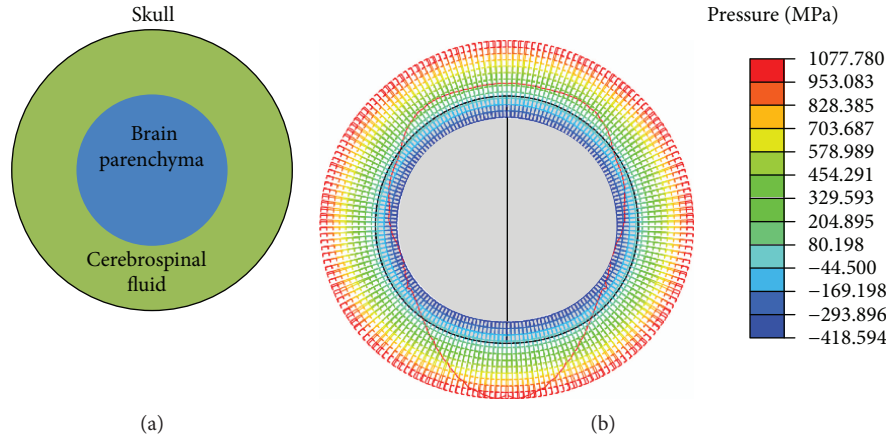


FIGURE 5: (a) The simple finite element model of a gecko brain. (b) The pressure distribution around the brain, indicated by a red curve. The black circle denotes the brain surface, and the color-coded mesh represents the values of pressure.

TABLE 1: The comparison of pressure on the brain parenchyma for different proportion of the CSF at different falling heights.

Height (m)	CSF 45%		CSF 22%	
	Positive pressure (MPa)	Negative pressure (MPa)	Positive pressure (MPa)	Negative pressure (MPa)
1.0	1077.78	428.92	1285.06	396.25
0.5	925.93	337.26	1064.86	302.90

a half-plane strain model. The initial contact between the ground and the skull, between the CSF and the skull, and the brain and the CSF were established using the contact-pair tool in ABAQUS/Explicit. All the structures were meshed into a quadrilateral, and the CPE4R elements were employed throughout. The model was built based on the fundamental principles of continuum mechanics, and the simplification on the fluid of CSF also had precedents [19], which guaranteed the model as secure as possible.

The simulation showed the pressure distribution around the brain was varying during the interaction between the head and the ground. When the two objects got stuck, strain built up. Along the vertical direction, the compressive stress was increasing that caused positive pressure on the brain, while along the lateral direction, the tensile stress was increasing that caused negative pressure on the brain (Figure 5(b)).

The CSF accounts for around 45% of a gecko brain. Different proportion of the fluid may affect the pressure limits caused by falling and head impact. Additionally, the height of falling could be another factor. Here, we simulated two proportions of the CSF, 45% and 22%, given two different falling heights, 1 m and 0.5 m, respectively. The comparison is shown in Table 1.

3.3. The Succulent Characteristic of a Gecko's Head. The MRI investigation has disclosed the succulent characteristic of a gecko's head. The intracalvarium of the head is full of the CSF, up to 45% in volume. Animal skulls contain a space

between the brain and the skull's vascular tissue, called a subarachnoid cavity. The cavity houses the CSF. It is said that CSF can only provide cushioning from minor bumps and jostling. In the instances of strong vibrations or blows, CSF will allow excessive movement of the brain, potentially resulting in bruising and concussions. One factor of the antishock mechanism in the woodpecker is that it has relatively little CSF [12, 20], thereby reducing the transmission of the mechanical excitations into the brain through the CSF [21, 22]. This is contradictory to what we found in a gecko's head. However, from a physical point of view, the mode of head shock in a woodpecker is different from that in the gecko. The former is a bilateral vibration in a certain frequency, by which the brain parenchyma may be restrained near the equilibrium position relative to the skull. The latter is an instant unidirectional impactation, by which the brain parenchyma may overshoot far from its equilibrium position. This might be the reason why the amounts of CSF in the woodpecker and in gecko are so different.

According to the comparison in Table 1, the high proportion of the CSF helps to reduce the maximal positive pressure, around 16% and 13%, at the falling height 1 m and 0.5 m, respectively. But it also causes an increase in the maximal negative pressure, around 8% and 11%, at the falling height 1 m and 0.5 m, respectively. Both positive and negative pressures in the intracalvarium are the reasons for brain injury [23]. Decreased positive pressure and increased negative pressure are the two opposites of the self-protection in the head impactation but which affects the brain more is still unknown. Speculatively, especially for the high falling height (1.0 m), for the high proportion of the CSF, the benefit of decreasing positive pressure (16%) surpasses the perils of increasing negative pressure (8%). This may be one of the advantages of natural selection and evolution for animals who can move at high altitude.

The finite element model and simulation developed in here is quite simple, which need further investigation using more fidelity models, such as considering the complex cortical bone property [24, 25]. However, the simple model has

implied the succulent characteristics of head impact in *Gekko geckos* qualitatively from several aspects. First, the fluid spreads the impulse across a wide area, allowing the material to absorb more of the impact. Second, the hydrodynamic drag gradually slows down the motion of the brain parenchyma caused by inertia after head impact. Thirdly, the good liquidity of the CSF attenuates the positive pressure in the intracalvarium. All those imply that the succulent characteristics of a gecko's head may play an important role in the self-protection in the head impaction, which is worth further studying and supplements to the behavioral and bionic application studies in *Gekko geckos* [26].

ARA is one of the important abilities for animals who move on high. It has been shown that ARA probably starts developmentally as a reflex and within days/weeks matures into CPG [9]. From an evolutionary point of view, this is a relatively later evolutionary state. The succulent characteristic of a gecko's head may provide a case in which the ARA starts in an earlier evolutionary state. More importantly, this may imply how nature has compensated for this by providing an alternative approach to protect the head. As evolution progressed, from reptiles to birds and mammals, the ARA developed and the need for 45% CSF was reduced, thus releasing space for the brain.

4. Conclusion

This study investigated the internal environment and structure of a *Gekko gecko*'s brain qualitatively and quantitatively, in order to understand their mechanism underlying the self-protection in head impaction. This study was also necessary in order to discover possible alternative mechanisms, besides the air-righting abilities, responsible for protecting animals moving on high from head injuries in falling. The succulent characteristic of a *Gekko gecko*'s brain was disclosed. By means of surgical anatomy, it was shown that the *Gekko gecko*'s brain parenchyma was fully surrounded by the CSF, while by means of the MRI techniques, it was shown that the intracalvarium was significantly occupied by the CSF, up to 45% in volume. The three-dimensional finite element model and its simulation on the impactions due to falling from different heights showed that the succulent characteristic contributed to the positive pressure decreasing during the head impaction but also to the negative pressure increasing. The former is beneficial to the self-protection in head impactions while the latter is not. Though the decreased positive pressure showed clear advantages over the increased negative pressure when falling from great height, at the point of view of the change rate in pressures, it needs further detail and elegant comparative studies to draw comprehensive conclusions. To our certain knowledge, to date, there has been no systematic interspecific or intraspecific comparative studies on how the CSF affects the mechanical property of the head and the consequence in self-protection. As one step further of this research, a fidelity finite element modeling study and physical model validation involving the morphology of the brain, the CSF and the skull, and their mechanical properties are demanded.

Conflicts of Interest

The authors declare that there are no conflicts of interest regarding the publication of this paper.

Acknowledgments

The authors thank Dr. Xuxia Wang at Wuhan Institute of Physics and Mathematics, CAS, for her help in MRI scanning. This research was supported by NSFC (61375096) and 863 Program (2015AA042304).

References

- [1] T. R. Kane and M. P. Scher, "A dynamical explanation of the falling cat phenomenon," *International Journal of Solids and Structures*, vol. 5, no. 7, pp. 663–670, 1969.
- [2] E. J. Marey, "The movements that certain animals execute to fall on their feet when they are tossed from an elevated place (translated from French)," *Science*, vol. 119, pp. 714–717, 1984.
- [3] D. A. McDonald, "How does a cat fall on its feet?," *New Scientist*, vol. 7, pp. 1647–1649, 1960.
- [4] R. Montgomery, "Gauge theory of the falling cat. Fields Institute," *Communications*, vol. 1, pp. 193–218, 1993.
- [5] A. Jusufi, D. I. Goldman, S. Revzen, and R. J. Full, "Active tails enhance arboreal acrobatics in geckos," *Proceedings of the National Academy of Sciences of the United States of America*, vol. 105, no. 11, pp. 4215–4219, 2008.
- [6] S. P. Yanoviak, Y. Munk, M. A. Kaspari, and R. Dudley, "Aerial manoeuvrability in wingless gliding ants (*Cephalotes atratus*)," *Proceedings of the Royal Society B*, vol. 277, no. 1691, pp. 2199–2204, 2010.
- [7] S. P. Yanoviak, Y. Munk, and R. Dudley, "Evolution and ecology of directed aerial descent in arboreal ants," *Integrative and Comparative Biology*, vol. 51, no. 6, pp. 944–956, 2011.
- [8] Y. Laouris, J. Kalli-Laouri, and P. Schwartze, "The postnatal development of the air-righting reaction in albino rats. Quantitative analysis of normal development and the effect of preventing neck-torso and torso-pelvis rotations," *Behavioural Brain Research*, vol. 37, no. 1, pp. 37–44, 1990.
- [9] Y. Laouris, J. Kalli-Laouri, and P. Schwartze, "The influence of altered head, thorax and pelvis mass on the postnatal development of the air-righting reaction in albino rats," *Behavioural Brain Research*, vol. 38, no. 2, pp. 185–190, 1990.
- [10] J. Schönfelder, "The development of air-righting reflex in postnatal growing rabbits," *Behavioural Brain Research*, vol. 11, no. 3, pp. 213–221, 1984.
- [11] H. Wang, L. Wang, J. D. Shao, T. T. Liu, and Z. D. Dai, "Long hindlimbs contribute to air-righting performance in falling tree frogs," *Journal of Mechanics in Medicine and Biology*, vol. 13, no. 06, article 1340023, 2013.
- [12] P. R. May, J. M. Fuster, P. Newman, and A. Hirschman, "Woodpeckers and head injury," *The Lancet*, vol. 307, no. 7957, pp. 454–455, 1976.
- [13] P. R. May, J. M. Fuster, J. Haber, and A. Hirschman, "Woodpecker drilling behavior. An endorsement of the rotational theory of impact brain injury," *Archives of Neurology*, vol. 36, no. 6, pp. 370–373, 1979.
- [14] R. D. Stark, D. J. Dodenhoff, and E. V. Johnson, "A quantitative analysis of woodpecker drumming," *Condor*, vol. 100, no. 2, pp. 350–356, 1998.

- [15] Z. D. Zhu, C. W. Wu, and W. Zhang, "Frequency analysis and anti-shock mechanism of woodpecker's head structure," *Journal of Bionic Engineering*, vol. 11, no. 2, pp. 282–287, 2014.
- [16] R. L. Hickling and M. L. Wenner, "Mathematical model of a head subjected to an axisymmetric impact," *Journal of Biomechanics*, vol. 6, no. 2, pp. 115–132, 1973.
- [17] S. L. Dawson, S. H. Charles, F. V. Lucas, and B. A. Sebek, "The countercoup phenomenon: reappraisal of a classic problem," *Human Pathology*, vol. 11, no. 2, pp. 155–166, 1980.
- [18] I. G. Bloomfield, I. H. Johnston, and L. E. Bilston, "Effects of proteins, blood cells and glucose on the viscosity of cerebrospinal fluid," *Pediatric Neurosurgery*, vol. 28, no. 5, pp. 246–251, 1998.
- [19] Z. D. Dai and S. Gorb, "Contact mechanics of pad of grasshopper (Insecta: ORTHOPTERA) by finite element methods," *Chinese Science Bulletin*, vol. 54, no. 4, pp. 549–555, 2009.
- [20] L. Wang, J. T. Cheung, F. Pu, M. Zhang, and Y. Fan, "Why do woodpeckers resist head impact injury: a biomechanical investigation," *PLoS One*, vol. 6, no. 10, article e26490, 2011.
- [21] I. R. Schwab, "Cure for a headache," *British Journal of Ophthalmology*, vol. 86, no. 8, pp. 843–846, 2002.
- [22] S. H. Yoon and S. Park, "A mechanical analysis of woodpecker drumming and its application to shock-absorbing systems," *Bioinspiration & Biomimetics*, vol. 6, no. 1, article 016003, 2011.
- [23] J. F. Kraus and D. L. McArthur, "Epidemiologic aspects of brain injury," *Neurologic Clinics*, vol. 14, no. 2, pp. 435–450, 1996.
- [24] J. H. Mcelhaney, J. L. Fogle, J. W. Melvin, R. R. Haynes, V. L. Roberts, and N. M. Alem, "Mechanical properties of cranial bone," *Journal of Biomechanics*, vol. 3, no. 5, pp. 495–511, 1970.
- [25] U. Stefan, B. Michael, and S. Werner, "Effects of three different preservation methods on the mechanical properties of human and bovine cortical bone," *Bone*, vol. 47, pp. 1048–1053, 2010.
- [26] S. Y. Liu, P. Zhang, H. Lü, C. W. Zhang, and Q. Xia, "Fabrication of high aspect ratio microfiber arrays that mimic gecko foot hairs," *Chinese Science Bulletin*, vol. 57, pp. 404–408, 2012.